

**Azimuthal P-wave AVA Inversion for Fracture  
Orientation and Density**

---

A Thesis  
Presented to  
the Faculty of the Department of Earth and Atmospheric Sciences  
University of Houston

---

In Partial Fulfillment  
of the Requirements for the Degree  
Master of Science

---

By  
Keyao Xia

May 2014

# **Azimuthal P-wave AVA Inversion for Fracture Orientation and Density**

---

Keyao Xia

APPROVED:

---

Dr. Aibing Li, Chairman  
Department of Earth and Atmospheric Sciences

---

Dr. Fred Hilterman, Co-Chairman  
Department of Earth and Atmospheric Sciences

---

Dr. Evgeny Chesnokov, Committee member  
Department of Earth and Atmospheric Sciences

---

Dr. Zhiyong Zhao, Committee member  
Geokinetics Inc.

---

Dean, College of Natural Sciences and  
Mathematics

# ACKNOWLEDGEMENTS

First of all, I would like to express my gratitude to my supervisor Dr. Fred Hilterman for his continuous support, consistent advice, and patient guidance throughout all aspects of this research. And most appreciated, he provided me unyielding encouragement and support in various ways. I am indebted to him more than he knows.

I also want to thank my committee members, Dr. Evgeny Chesnokov, Dr. Aibing Li, and Dr. Zhiyong Zhao, for their participation in and sincere suggestions for my thesis.

I feel privileged to have learned a great deal from my peers, Luanxiao Zhao, Rui Zhou, Zhao Li, Huizhong Yan, Ayodeji Babalola, and Yuandi Gan, about effective medium theory, anisotropy, and inversion. And I also want to thank Sami Atassi, who had helped me through the editorial process.

Last but not least, I thank my parents for their unending patience, encouragement, love, support, and faith in my abilities.

# **Azimuthal P-wave AVA Inversion for Fracture Orientation and Density**

---

An Abstract of a Thesis

Presented to

the Faculty of the Department of Earth and Atmospheric Sciences

University of Houston

---

In Partial Fulfillment

of the Requirements for the Degree

Master of Science

---

By

Keyao Xia

May 2014

# ABSTRACT

This thesis studies the numerical seismic modeling of a simulated fractured medium to analyze variations of seismic reflection amplitudes with incident and azimuthal angles (AVAZ). The intent is to extract the information about the fracture orientation and intensity of a fractured medium. The effective compliance tensor for a fractured medium can be written as the sum of the compliance tensor of the unfractured background rock and the compliance tensor for the set of aligned fractures. Based on the assumption of rotationally invariant fracture sets, two fracture compliances—the normal and tangential compliance—are required to specify the fracture compliance tensor. The stiffness tensor can be attained by inverting the compliance tensor. The P-wave reflection coefficients for arbitrary anisotropic media are obtained by two methods (Chattopadhyay, 2004; Schoenberg and Protazio, 1992). Rüger’s linear approximation can accurately estimate the exact reflection coefficients and hence it is widely used in the linear inversion. Analysis is applied in the decision to choose between the incident angle and the average angle for Rüger’s linear approximation.

Linear AVAZ inversions, based on singular value decomposition (SVD), and non-linear AVAZ inversion, based on generalized linear inversion (GLI), for fracture orientation and HTI anisotropy parameters, were applied on P-wave reflection coefficients with variable incident angle and azimuth. However,  $90^\circ$  ambiguity in the estimation of the fracture orientation always exists. Sensitivity analysis of the inversion results, including S/N ratio, maximum incident angle used, and error propagation, confirms the accuracy of the amplitude analysis.

# TABLE OF CONTENTS

ACKNOWLEDGEMENTS.....	iii
ABSTRACT.....	v
TABLE OF CONTENTS.....	vi
LIST OF FIGURES .....	viii
LIST OF TABLES .....	xii
Chapter 1.....	1
Introduction.....	1
1.1 Organization of the thesis.....	3
1.2 Contribution of the thesis .....	4
Chapter 2.....	5
Review of Seismic Anisotropy.....	5
2.1 Introduction .....	5
2.2 Hooke’s law for isotropic media.....	5
2.3 Hooke’s law for anisotropic media.....	6
2.4 Voigt notation .....	7
2.5 Symmetry system .....	9
2.6 Thomsen’s notation and its equivalence for HTI media.....	11
2.7 Phase velocity and group velocity.....	18
2.8 Conclusion.....	25
Chapter 3.....	26
Reflection and Transmission Coefficients for Anisotropic Media.....	26
3.1 Introduction .....	26
3.2 Reflection and transmission coefficients (Chattopadhyay).....	27
3.3 Reflection and transmission coefficients (Schoenberg and Protazio) .....	31
3.4 Reflection coefficient approximations for HTI media (Rüger).....	38
3.5 Incident angle versus average angle .....	46
3.6 Conclusion.....	50
Chapter 4.....	51
Effective Medium Theory.....	51
4.1 Introduction .....	51
4.2 Crack density .....	52

4.3	Parallel fractures: linear slip theory.....	53
4.4	Aligned penny-shaped crack .....	61
4.5	Bond transformation.....	75
4.6	Accuracy.....	78
4.7	Conclusion.....	82
Chapter 5.....		83
AVAZ Inversion .....		83
5.1	Introduction .....	83
5.2	SVD inversion .....	83
5.3	Generalized linear inversion.....	87
5.4	Inversion for fracture orientation.....	91
5.5	Inversion for anisotropy parameters.....	103
5.6	Error analysis.....	107
5.7	Conclusion.....	123
Chapter 6.....		125
Conclusion .....		125
APPENDIX A.....		128
APPENDIX B.....		129
REFERENCE.....		130

# LIST OF FIGURES

Figure 2.1. The symmetry axis for VTI and HTI models (Rüger, 2002).....	14
Figure 2.2. The relationship between phase angle and group angle (Chen, 2000).....	18
Figure 2.3. The phase velocities of P-wave, SV-wave, and SH-wave for illite. The elastic constants for illite are given in Appendix A. ....	24
Figure 2.4. The group velocities of P-wave, SV-wave, and SH-wave for illite. The elastic constants for illite are given in Appendix A. ....	24
Figure 3.1. Scheme of an incident wave hits an interface. $\theta$ denotes the angle between the slowness vector of the incident wave and vertical axis. $\phi$ is the azimuthal angle which is defined with respect to the symmetry axis pointing in the $x_1$ -direction (Rüger, 2002). ....	27
Figure 3.2. Reflected and transmitted waves caused by an incident quasi-P-wave hits the interface between two anisotropic half-spaces.. ....	28
Figure 3.3. Exact reflection coefficients for an isotropic half-space over a VTI half-space with elastic constants given in Appendix B. ....	36
Figure 3.4. Exact reflection coefficients for an isotropic half-space over a HTI half-space with elastic constants given in Appendix B. ....	36
Figure 3.5. Exact reflection coefficients for a VTI half-space over a HTI half-space with elastic constants given in Appendix B. ....	37
Figure 3.6. Reflection coefficients for an isotropic half-space over a HTI half-space. Dashed lines are the exact results and solid lines are the results calculated by linearized approximation for azimuths of $0^\circ$ , $30^\circ$ , $60^\circ$ , and $90^\circ$ . Model parameters are given in Table 3.1 (A). ....	41
Figure 3.7. Reflection coefficients for an isotropic half-space over a HTI half-space. Dashed lines are the exact results and solid lines are the results calculated by linearized approximation for azimuths of $0^\circ$ , $30^\circ$ , $60^\circ$ , and $90^\circ$ . Model parameters are given in Table 3.1 (B). ....	41
Figure 3.8. Reflection coefficients for an isotropic half-space over a HTI half-space. Dashed lines are the exact results and solid lines are the results calculated by linearized approximation for azimuths of $0^\circ$ , $30^\circ$ , $60^\circ$ , and $90^\circ$ . Model parameters are given in Table 3.1 (C). ....	42
Figure 3.9. Reflection coefficients for an isotropic half-space over a HTI half-space. Dashed lines are the exact results and solid lines are the results calculated by linearized approximation for azimuths of $0^\circ$ , $30^\circ$ , $60^\circ$ , and $90^\circ$ . Model parameters are given in Table 3.1 (D). ....	42
Figure 3.10. Deviation between exact P-wave reflection coefficients and approximations for Model A. The exact reflection coefficients and the linearized approximations are shown in Figure 3.6. ....	44
Figure 3.11. Deviation between exact P-wave reflection coefficients and approximations for Model B. The exact reflection coefficients and the linearized approximations are shown in Figure 3.7. ....	44

Figure 3.12. Deviation between exact P-wave reflection coefficients and approximations for Model C. The exact reflection coefficients and the linearized approximations are shown in Figure 3.8.....	45
Figure 3.13. Deviation between exact P-wave reflection coefficients and approximations for Model D. The exact reflection coefficients and the linearized approximations are shown in Figure 3.9.....	45
Figure 3.14. Reflection coefficients with azimuthal angle of $0^\circ$ calculated by incident angle and average angle. Exact reflection coefficients are calculated by azimuthal angle of $0^\circ$ .....	48
Figure 3.15. Reflection coefficients with azimuthal angle of $30^\circ$ calculated by incident angle and average angle. Exact reflection coefficients are calculated by azimuthal angle of $30^\circ$ .....	48
Figure 3.16. Reflection coefficients with azimuthal angle of $60^\circ$ calculated by incident angle and average angle. Exact reflection coefficients are calculated by azimuthal angle of $60^\circ$ .....	49
Figure 3.17. Reflection coefficients with azimuthal angle of $90^\circ$ calculated by incident angle and average angle. Exact reflection coefficients are calculated by azimuthal angle of $90^\circ$ .....	49
Figure 4.1. Diagrammatic view of a vertically fractured medium (Schoenberg and Sayers, 1995).....	54
Figure 4.2. Maps of joint traces in two directions on bedding surface of Rico Formation, Monument upwarp, southeastern Utah (Schoenberg and Sayers, 1995).....	56
Figure 4.3. Phase velocities of P-wave, SV-wave, and SH-wave of a fractured medium, with P-wave velocity in the isotropic host rock equals to 2.5 km/s; S-wave velocity in the isotropic host rock, 1.5 km/s; density, $2.7 \text{ g/cm}^3$ ; and, crack density, 0.03.....	66
Figure 4.4. Group velocities of P-wave, SV-wave, and SH-wave of a fractured medium, with P-wave velocity in the isotropic host rock equals to 2.5 km/s; S-wave velocity in the isotropic host rock, 1.5 km/s; density, $2.7 \text{ g/cm}^3$ ; and, crack density, 0.03.....	67
Figure 4.5. Phase velocity of P-wave in the vertical symmetry plane. Model parameters are the same as Figure 4.3 except for crack density.....	70
Figure 4.6. Phase velocity of P-wave in the isotropic plane. Model parameters are the same as Figure 4.3 except for crack density.....	70
Figure 4.7. Phase velocity of SV-wave in the vertical symmetry plane. Model parameters are the same as Figure 4.3 except for crack density.....	71
Figure 4.8. Phase velocity of SV-wave in the isotropic plane. Model parameters are the same as Figure 4.3 except for crack density.....	71
Figure 4.9. Phase velocity of SH-wave in the vertical symmetry plane. Model parameters are the same as Figure 4.3 except for crack density.....	72
Figure 4.10. Phase velocity of SH-wave in the isotropic plane. Model parameters are the same as Figure 4.3 except for crack density.....	72
Figure 4.11. Reflection coefficients for the interface between an isotropic medium and a fractured medium.....	74

Figure 4.12. P-wave velocity of a fractured rock before rotation and after rotation. The model parameters are the same as those given for Figure 4.3. ....	77
Figure 4.13. Anisotropic parameters (a) $\varepsilon^{(v)}$ , (b) $\delta^{(v)}$ , and (c) $\gamma^{(v)}$ for a single set of vertical penny-shaped dry cracks (Grechka and Kachanov, 2006). ....	79
Figure 4.14. Irregular vertical cracks. All fractures are planar; Their normals are directed along the $x_1$ - axis . The faces of cracks 2, 3, and 4 have sharp edges. Geometries 4, 5, and 6, that contain interior rock islands, represent partially closed fractures (Grechka and Kachanov, 2006). ....	80
Figure 4.15. Misfits $\Delta_c^{nm}$ for six fracture shapes in Figure 4.14 (Grechka and Kachanov, 2006). ....	80
Figure 5.1. Workflow for generalized linear inversion (Cooke and Schneider, 1983). ....	89
Figure 5.2. Inversion result for the fracture orientation. The lower HTI medium is rotated by $20^\circ$ . S/N = 20. ....	95
Figure 5.3. Error of inversion result for the fracture orientation. The lower HTI medium is rotated by $20^\circ$ . S/N = 20. ....	95
Figure 5.4. Inversion result for the fracture orientation. The lower HTI medium is rotated by $110^\circ$ . S/N = 20. ....	96
Figure 5.5. Error of inversion result for the fracture orientation. The lower HTI medium is rotated by $110^\circ$ . S/N = 20. ....	96
Figure 5.6. Inversion result for the fracture orientation. The lower HTI medium is rotated by $20^\circ$ . S/N = 10. ....	97
Figure 5.7. Error of inversion result for the fracture orientation. The lower HTI medium is rotated by $20^\circ$ . S/N = 10. ....	97
Figure 5.8. Inversion result for the fracture orientation. The lower HTI medium is rotated by $110^\circ$ . S/N = 10. ....	98
Figure 5.9. Error of inversion result for the fracture orientation. The lower HTI medium is rotated by $110^\circ$ . S/N = 10. ....	98
Figure 5.10. Inversion result for the fracture orientation. The lower HTI medium is rotated by $20^\circ$ . S/N = 5. ....	99
Figure 5.11. Error of inversion result for the fracture orientation. The lower HTI medium is rotated by $20^\circ$ . S/N = 5. ....	99
Figure 5.12. Inversion result for the fracture orientation. The lower HTI medium is rotated by $110^\circ$ . S/N = 5. ....	100
Figure 5.13. Error of inversion result for the fracture orientation. The lower HTI medium is rotated by $110^\circ$ . S/N = 5. ....	100
Figure 5.14. Inversion result for the fracture orientation based on the exact reflection coefficient inversion. The lower HTI medium is rotated by $20^\circ$ . ....	101
Figure 5.15. Inversion result for the fracture orientation based on the exact reflection coefficient inversion. The lower HTI medium is rotated by $110^\circ$ . ....	101
Figure 5.16. Inversion error for $\delta^{(v)}$ . ....	105
Figure 5.17. Inversion error for $\varepsilon^{(v)}$ . ....	105
Figure 5.18. Inversion error for $\gamma$ . ....	106

Figure 5.19. Inversion error results with S/N = 20. $a, b, c, d, e,$ and $f$ denote $\frac{\Delta\alpha}{\bar{\alpha}}, \frac{\Delta\beta}{\bar{\beta}}, \frac{\Delta\rho}{\bar{\rho}}, \delta^{(v)}, \varepsilon^{(v)},$ and $\gamma$ .....	108
Figure 5.20. Inversion error results with S/N = 10. $a, b, c, d, e,$ and $f$ denote $\frac{\Delta\alpha}{\bar{\alpha}}, \frac{\Delta\beta}{\bar{\beta}}, \frac{\Delta\rho}{\bar{\rho}}, \delta^{(v)}, \varepsilon^{(v)},$ and $\gamma$ .....	108
Figure 5.21. Inversion error results with S/N = 5. $a, b, c, d, e,$ and $f$ denote $\frac{\Delta\alpha}{\bar{\alpha}}, \frac{\Delta\beta}{\bar{\beta}}, \frac{\Delta\rho}{\bar{\rho}}, \delta^{(v)}, \varepsilon^{(v)},$ and $\gamma$ .....	109
Figure 5.22. Inversion error results with S/N = 2. $a, b, c, d, e,$ and $f$ denote $\frac{\Delta\alpha}{\bar{\alpha}}, \frac{\Delta\beta}{\bar{\beta}}, \frac{\Delta\rho}{\bar{\rho}}, \delta^{(v)}, \varepsilon^{(v)},$ and $\gamma$ .....	109
Figure 5.23. Inversion errors from data with incident angles from $0^\circ$ to $10^\circ$ . $a = \delta^{(v)}, b = \varepsilon^{(v)},$ and $c = \gamma$ .....	112
Figure 5.24. Inversion errors from data with incident angles from $0^\circ$ to $15^\circ$ . $a = \delta^{(v)}, b = \varepsilon^{(v)},$ and $c = \gamma$ .....	112
Figure 5.25. Inversion errors from data with incident angles from $0^\circ$ to $20^\circ$ . $a = \delta^{(v)}, b = \varepsilon^{(v)},$ and $c = \gamma$ .....	113
Figure 5.26. Inversion errors from data with incident angles from $0^\circ$ to $25^\circ$ . $a = \delta^{(v)}, b = \varepsilon^{(v)},$ and $c = \gamma$ .....	113
Figure 5.27. Inversion errors from data with incident angles from $0^\circ$ to $30^\circ$ . $a = \delta^{(v)}, b = \varepsilon^{(v)},$ and $c = \gamma$ .....	114
Figure 5.28. Inversion errors from data with incident angles from $0^\circ$ to $35^\circ$ . $a = \delta^{(v)}, b = \varepsilon^{(v)},$ and $c = \gamma$ .....	114
Figure 5.29. Inversion errors from data with incident angles from $0^\circ$ to $40^\circ$ . $a = \delta^{(v)}, b = \varepsilon^{(v)},$ and $c = \gamma$ .....	115
Figure 5.30. Inversion errors from data with incident angles from $0^\circ$ to $45^\circ$ . $a = \delta^{(v)}, b = \varepsilon^{(v)},$ and $c = \gamma$ .....	115
Figure 5.31. Inversion errors from data with incident angles from $0^\circ$ to $50^\circ$ . $a = \delta^{(v)}, b = \varepsilon^{(v)},$ and $c = \gamma$ .....	116
Figure 5.32. Difference between the reflection coefficients for rotation angles of $0^\circ$ and $5^\circ$ .....	119
Figure 5.33. Inversion error for anisotropic parameters for an error of $5^\circ$ in the estimated fracture orientation. $a = \delta^{(v)}, b = \varepsilon^{(v)},$ and $c = \gamma$ .....	120
Figure 5.34. Difference between the reflection coefficients for rotation angles of $0^\circ$ and $10^\circ$ .....	121
Figure 5.35. Inversion error for anisotropic parameters for an error of $10^\circ$ in the estimated fracture orientation. $a = \delta^{(v)}, b = \varepsilon^{(v)},$ and $c = \gamma$ .....	122

## LIST OF TABLES

TABLE 2.1. Thomsen's equivalence for HTI medium and its relation to the generic Thomsen parameters. ....	17
TABLE 3.1. Model parameters used to study the accuracy of the approximation equation. ....	40
TABLE 4.1. Coordinate cosine values between pre- and post- rotation. ....	75

# CHAPTER 1

## INTRODUCTION

With the rapid development of the oil and gas industry in the world, geophysicists play an important role in the exploration of all types of hydrocarbon reservoirs. These include fractured reservoirs, which have pervasively existed in carbonates, tight clastic sediments, and basements reservoirs. However, fractures have different effects on hydrocarbon production. One positive impact is fractures can provide more pore space for reservoirs to store gas and oil. Moreover, permeability is vastly increased by fractures so that hydrocarbons can be easily migrated. Unfortunately, fractures sometimes also play a detrimental role. Fractures may be the cause of leakage of traps in some reservoirs. As well, cemented and mineralized fractures may act as barriers of fluid flow (Nelson, 1985; Aguilera, 2003). Therefore, it is meaningful and challenging for not only geophysicists but also geologists and reservoir engineers to study the orientation and distribution of fractures when evaluating a reservoir.

Seismic anisotropy can be defined as “the dependence of seismic velocity upon angle” (Thomsen, 2002). The velocity anisotropy may be caused by several reasons, such as rock fabric, grain-scale microcracks, rock layering, and aligned fractures at all scales, provided that seismic wavelengths are much larger than the size and spacing of the fracture (Worthington, 2008).

Both direct and indirect methods can be used to characterize fractures. Well log curves and core samples are the most direct and simplest methods to analyze fractures.

However, these direct methods can only apply to a small area near well locations. Indirect exploration methods like seismic analysis are required to find the orientation and density of fractures. The azimuthal variation in reflection amplitude of seismic P-wave is used to study fractured reservoirs. The method to use reflection amplitudes for fracture characterization has advantages over seismic velocity, because reflection amplitudes have higher vertical resolution and are more sensitive to the properties of reservoirs.

In this work, linear slip theory (Schoenberg, 1980; Schoenberg, 1983) is used to specify the relationship between stress and strain by fracture compliance. Schoenberg suggests treating fractures as infinitely thin and highly compliant (soft) layers or planes of weakness (Bakulin *et al.*, 2000). Linear slip boundary conditions are applied to the interface across which traction is continuous, but the displacement is discontinuous. The exact reflection coefficients are obtained by two different methods for arbitrary anisotropic media. In addition, Rüger's linear approximation for transversely isotropic medium with a horizontal symmetry axis is introduced and applied for linear inversion. Both linear and non-linear inversions are used to invert for fracture orientation. Linear inversion, which is better for low S/N data, is used to invert for anisotropy parameters.

P-wave seismic exploration has been widely used for fracture analysis for the past several years. Tsvankin and Lynn (1999) list the following reasons for using P-wave data: (1) lower cost of P-wave acquisition compared to surveys for S-waves, (2) usually higher data quality of P-wave compared to S-waves, and (3) development of azimuthal techniques on P-wave data for obtaining principal directions and magnitude of anisotropy.

## 1.1 Organization of the thesis

In Chapter 2, I begin with a review of anisotropic media. Hooke's law is introduced to relate stress and strain for isotropic and anisotropic media. Voigt notation is used to simplify the  $3 \times 3 \times 3 \times 3$  stiffness tensor into  $6 \times 6$  stiffness matrix. Thomsen (1986) introduces a widely used notation for transversely isotropic media with a vertical symmetry axis (VTI). Rüger (2002) provides another set of anisotropy parameters, which is similar to Thomsen's notation, to describe a transversely isotropic medium with a horizontal symmetry axis (HTI). The first and the second Green-Christofel equations, which are used to obtain the phase velocity and group velocity, are described in detail in this chapter.

In Chapter 3, two methods are presented to calculate the exact reflection coefficients for arbitrary anisotropic media. Rüger's linear approximation provides a convenient way to obtain the P-wave reflection coefficients approximation for HTI media. The difference between this approximation and the exact reflection coefficients is acceptable at small angles. The choice of average angle (average of the incident and transmission angles across the boundary) and incident angle for Rüger's linear approximation is analyzed in this chapter.

The effective medium theory is described in Chapter 4 for a set of vertical, aligned fractures. The linear slip theory (Schoenberg, 1980; Schoenberg, 1983) is used to link the seismic signatures to the properties of fracture systems. Under certain conditions, Schoenberg and Douma (1988) express the fracture compliance in terms of crack density and the ratio of S-wave and P-wave velocity of the host isotropic rock. And a set of

vertical, aligned, rotationally invariant fractures leads to a particular HTI medium, which can be specified by only four independent parameters.

The linear and non-linear inversions are introduced in Chapter 5. The singular value decomposition inversion (SVD), which is a linear inversion, is based on Rüger's linear approximation. And the generalized linear inversion (GLI), which is a non-linear inversion, is based on Chattopadhyay's method. Both of these two inversion methods are used to invert for the fracture orientation. The anisotropic parameters are obtained by the SVD method. Different error analyses are also discussed in this chapter.

## **1.2 Contribution of the thesis**

Seismic amplitude variation for anisotropic media is very complicated. The seismic amplitude shows variation with azimuthal change for an interface between isotropic medium and HTI medium, which is the main concern of my work. Numerical modeling and inversion in this thesis show an outline to invert for the fracture orientation and density from seismic amplitude. The main contributions of this thesis are as follows:

- The method to obtain phase and group velocities for arbitrary anisotropic media is introduced in detail.
- Two methods for exact reflection coefficients for arbitrary anisotropic media are explained in detail.
- Linear and non-linear inversions are applied to invert for the fracture orientation. The reason for  $90^\circ$  ambiguity in the inversion result is discussed.
- Error analysis is applied for S/N ratio, maximum incident angle, and error propagation.

## CHAPTER 2

# REVIEW OF SEISMIC ANISOTROPY

### 2.1 Introduction

Seismic anisotropy is defined to be the dependence of seismic velocity upon angle (Thomsen, 2002). However, there is no sharp criterion to demarcate isotropy and anisotropy. In general, we assume the medium is isotropic when it is hard to detect velocity variation with respect to direction, or when the effects of anisotropy are too small to affect any further processing or data interpretation (Helbig, 1994). By contrast, heterogeneity is defined to be the dependence of physical properties upon position. Small-scale ordered heterogeneity, such as the fabric of a rock, can result in large-scale seismic anisotropy. The terms large and small are compared to the seismic wavelength. When the seismic wavelength is large compared to the scale of ordered heterogeneities, we can assume the medium is anisotropic and it obeys the laws of anisotropic wave propagation.

### 2.2 Hooke's law for isotropic media

Strain and stress in isotropic media have a linear relationship which is defined experimentally by Hooke's law. Two constants (e.g. Lamé parameters  $\lambda$  and  $\mu$ ) describe this relationship between the stress  $\sigma$  and strain  $\epsilon$ ,

$$\sigma_{ij} = \lambda \delta_{ij} \epsilon_{kk} + 2\mu \epsilon_{ij}, \quad (2.1)$$

or

$$\varepsilon_{ij} = \frac{1}{E} [(1 + \nu)\sigma_{ij} - \nu\delta_{ij}\sigma_{\alpha\alpha}], \quad (2.2)$$

where

$\varepsilon_{ij}$  = elements of the strain tensor,

$\sigma_{ij}$  = elements of the stress tensor,

$\varepsilon_{\alpha\alpha}$  = volumetric strain (sum over repeated index),

$\sigma_{\alpha\alpha}$  = mean stress times 3 (sum over repeated index),

$\delta_{ij}$  = 0 if  $i \neq j$  and  $\delta_{ij}$  = 1 if  $i = j$ ,

E = Young's modulus, and

$\nu$  = Poisson's ratio.

Two constants are enough to specify the relationship between stress and strain for the linear elastic and isotropic medium. With bulk and shear modulus, the other elastic constants can be defined; however, there are only two independent constants.

### 2.3 Hooke's law for anisotropic media

For arbitrary anisotropic media, there is also an equation that links the stress and strain. Hooke's law for elastic anisotropic media states that the stress  $\sigma$  is linearly proportional to the strain  $\varepsilon$  through the fourth-rank stiffness or compliance tensor, as expressed by

$$\sigma_{ij} = C_{ijkl}\varepsilon_{kl}, \quad (2.3)$$

or

$$\varepsilon_{ij} = S_{ijkl} \sigma_{kl}, \quad (2.4)$$

where  $C_{ijkl}$  is the stiffness tensor and  $S_{ijkl}$  is the compliance tensor.

Both  $C_{ijkl}$  and  $S_{ijkl}$  are fourth-rank tensor that contains 81 components. The nine elements of the strain tensor and the nine elements of the stress tensor are related to each other by the 81 elastic constants of the stiffness tensor (Fedorov, 1968; Winterstein, 1990). However, not all 81 components are independent. Because of the symmetries existing in the stress tensor and strain tensor, we obtain a relationship between stiffness tensor by interchanging the indices  $i$  and  $j$ ,  $k$  and  $l$  in  $C_{ijkl}$  as

$$C_{ijkl} = C_{jikl} = C_{ijlk} = C_{jilk} \quad (2.5)$$

In addition, the existence of unique strain energy potential provides another relationship  $C_{ijkl} = C_{klij}$  which further reduces the number of independent constants to 21. And 21 independent constants are sufficient to specify the lowest symmetry which is triclinic medium. The number of independent constants for the different symmetry systems reduces from 21 for triclinic medium to 9 for orthorhombic medium and 2 for isotropic media (Winterstein, 1990).

## 2.4 Voigt notation

It is more convenient and practical to use the abbreviated Voigt notion to represent stress, strain, stiffness, and compliance tensors with a two-subscript notation rather than the fourth-rank tensor. Thus, the stress and strain are written as six element column vectors instead of nine element square matrices following the convention: 11  $\rightarrow$  1, 22  $\rightarrow$  2,

33→3, 23 & 32→4, 13 & 31→5, and 12 & 21→6.

$$T = \begin{pmatrix} \sigma_1 = \sigma_{11} \\ \sigma_2 = \sigma_{22} \\ \sigma_3 = \sigma_{33} \\ \sigma_4 = \sigma_{23} \\ \sigma_5 = \sigma_{13} \\ \sigma_6 = \sigma_{12} \end{pmatrix} \quad E = \begin{pmatrix} \varepsilon_1 = \varepsilon_{11} \\ \varepsilon_2 = \varepsilon_{22} \\ \varepsilon_3 = \varepsilon_{33} \\ \varepsilon_4 = 2\varepsilon_{23} \\ \varepsilon_5 = 2\varepsilon_{13} \\ \varepsilon_6 = 2\varepsilon_{12} \end{pmatrix} \quad (2.6)$$

The factor of 2 is only introduced in the definition of strain. The stiffness matrix is then represented as

$$\begin{pmatrix} c_{11} & c_{12} & c_{13} & c_{14} & c_{15} & c_{16} \\ c_{12} & c_{22} & c_{23} & c_{24} & c_{25} & c_{26} \\ c_{13} & c_{23} & c_{33} & c_{34} & c_{35} & c_{36} \\ c_{14} & c_{24} & c_{34} & c_{44} & c_{45} & c_{46} \\ c_{15} & c_{25} & c_{35} & c_{45} & c_{55} & c_{56} \\ c_{16} & c_{26} & c_{36} & c_{46} & c_{56} & c_{66} \end{pmatrix}, \quad (2.7)$$

and similarly, the compliance matrix is represented as

$$\begin{pmatrix} s_{11} & s_{12} & s_{13} & s_{14} & s_{15} & s_{16} \\ s_{12} & s_{22} & s_{23} & s_{24} & s_{25} & s_{26} \\ s_{13} & s_{23} & s_{33} & s_{34} & s_{35} & s_{36} \\ s_{14} & s_{24} & s_{34} & s_{44} & s_{45} & s_{46} \\ s_{15} & s_{25} & s_{35} & s_{45} & s_{55} & s_{56} \\ s_{16} & s_{26} & s_{36} & s_{46} & s_{56} & s_{66} \end{pmatrix}. \quad (2.8)$$

Both the stiffness and compliance matrices in Voigt notation are symmetric. The 21 independent constants in the upper triangle of the 6x6 matrix are sufficient to specify the lowest possible symmetric linear elastic material. And we can write the general Hooke's law as

$$\begin{pmatrix} \sigma_1 \\ \sigma_2 \\ \sigma_3 \\ \sigma_4 \\ \sigma_5 \\ \sigma_6 \end{pmatrix} = \begin{pmatrix} c_{11} & c_{12} & c_{13} & c_{14} & c_{15} & c_{16} \\ c_{12} & c_{22} & c_{23} & c_{24} & c_{25} & c_{26} \\ c_{13} & c_{23} & c_{33} & c_{34} & c_{35} & c_{36} \\ c_{14} & c_{24} & c_{34} & c_{44} & c_{45} & c_{46} \\ c_{15} & c_{25} & c_{35} & c_{45} & c_{55} & c_{56} \\ c_{16} & c_{26} & c_{36} & c_{46} & c_{56} & c_{66} \end{pmatrix} \begin{pmatrix} \varepsilon_1 \\ \varepsilon_2 \\ \varepsilon_3 \\ \varepsilon_4 \\ \varepsilon_5 \\ \varepsilon_6 \end{pmatrix}. \quad (2.9)$$

Note that the matrix in the Voigt notation is not tensor because the matrix in this notation no longer follows the laws of tensor transformation. There are two ways to do the tensor transformation from Voigt notation. We can convert the Voigt notation back to the four-index notation and then apply the tensor transformation. Or we can use the Bond transformation matrix which is more convenient and efficient to do the transformation. I will introduce this method in Chapter 4. And in this thesis, the capital  $C$  is used for the fourth-rank tensor and the minuscule  $c$  is used for the Voigt notation.

## 2.5 Symmetry system

Different symmetry systems can be defined by different elastic stiffness matrices as follows (Mavko *et al.*, 2009)

### Isotropic: two independent constants

$$c_{ij} = \begin{pmatrix} c_{11} & c_{12} & c_{12} & 0 & 0 & 0 \\ c_{12} & c_{11} & c_{12} & 0 & 0 & 0 \\ c_{12} & c_{12} & c_{11} & 0 & 0 & 0 \\ 0 & 0 & 0 & c_{44} & 0 & 0 \\ 0 & 0 & 0 & 0 & c_{44} & 0 \\ 0 & 0 & 0 & 0 & 0 & c_{44} \end{pmatrix}, \quad c_{12} = c_{11} - 2c_{44}. \quad (2.10)$$

As mentioned before, the elastic constants in the stiffness matrix for isotropic media can be specified by two Lamé parameters as  $c_{12} = \lambda$ ,  $c_{44} = \mu$ , and  $c_{11} = \lambda + 2\mu$ .

**Cubic: three independent constants**

$$c_{ij} = \begin{pmatrix} c_{11} & c_{12} & c_{12} & 0 & 0 & 0 \\ c_{12} & c_{11} & c_{12} & 0 & 0 & 0 \\ c_{12} & c_{12} & c_{11} & 0 & 0 & 0 \\ 0 & 0 & 0 & c_{44} & 0 & 0 \\ 0 & 0 & 0 & 0 & c_{44} & 0 \\ 0 & 0 & 0 & 0 & 0 & c_{44} \end{pmatrix} \quad (2.11)$$

**Hexagonal or Transversely isotropic: five independent constants**

$$c_{ij} = \begin{pmatrix} c_{11} & c_{12} & c_{13} & 0 & 0 & 0 \\ c_{12} & c_{11} & c_{13} & 0 & 0 & 0 \\ c_{13} & c_{13} & c_{33} & 0 & 0 & 0 \\ 0 & 0 & 0 & c_{44} & 0 & 0 \\ 0 & 0 & 0 & 0 & c_{44} & 0 \\ 0 & 0 & 0 & 0 & 0 & c_{66} \end{pmatrix}, \quad c_{66} = (c_{11} - c_{12}) \cdot \quad (2.12)$$

**Orthorhombic: nine independent constants**

$$c_{ij} = \begin{pmatrix} c_{11} & c_{12} & c_{13} & 0 & 0 & 0 \\ c_{12} & c_{11} & c_{13} & 0 & 0 & 0 \\ c_{13} & c_{13} & c_{33} & 0 & 0 & 0 \\ 0 & 0 & 0 & c_{44} & 0 & 0 \\ 0 & 0 & 0 & 0 & c_{44} & 0 \\ 0 & 0 & 0 & 0 & 0 & c_{66} \end{pmatrix} \quad (2.13)$$

In my thesis, I mainly considered the transversely isotropic (TI) medium. The transversely isotropic medium is one with the physical property which is symmetric about an axis that is normal to a plane of isotropy. The TI medium has infinite planes of isotropy and thus, within this plane, the velocities are the same in all directions. The TI medium is very important because it is a good approximation to several geologic models. For instance, the transversely isotropic medium with a vertical symmetry axis (VTI)

approximates the horizontal layered sedimentary rock model. More importantly in today's exploration for unconventional shale, a single set of vertical aligned fractures can be modeled by a transversely isotropic medium with a horizontal symmetry axis (HTI), if we consider the background rock as an isotropic medium.

## 2.6 Thomsen's notation and its equivalence for HTI media

For transversely isotropic media with a vertical symmetry axis (VTI) with weak elastic anisotropy, Thomsen (1986) introduces a widely used notation. Thomsen's notation regrouped the elastic constants into three anisotropic parameters ( $\delta$ ,  $\varepsilon$  and  $\gamma$ ) which simplifies the equations of the phase velocities of the P-, SV-, and SH-waves. Thomsen suggests the following convenient notation for VTI media in terms of the P-wave and S-wave velocities along the symmetry axis,  $\alpha$  and  $\beta$ , plus three additional constants,

$$\begin{aligned}\alpha &\equiv \sqrt{c_{33} / \rho} , \\ \beta &\equiv \sqrt{c_{44} / \rho} , \\ \varepsilon &\equiv \frac{c_{11} - c_{33}}{2c_{33}} , \\ \gamma &\equiv \frac{c_{66} - c_{44}}{2c_{44}} , \\ \delta &\equiv \frac{(c_{13} + c_{44})^2 - (c_{33} - c_{44})^2}{2c_{33}(c_{33} - c_{44})} .\end{aligned}$$

We can also invert the Thomsen parameters for the elastic constants to Voigt notation as

$$\begin{aligned}
c_{33} &= \rho\alpha^2, \\
c_{44} &= \rho\beta^2, \\
c_{11} &= c_{33}(1+2\varepsilon), \\
c_{66} &= c_{44}(1+2\gamma), \\
c_{13} &= \pm\sqrt{2c_{33}(c_{33}-c_{44})\delta + (c_{33}-c_{44})^2} - c_{44}.
\end{aligned}$$

Note for  $c_{13}$  there is a plus and minus sign before the square root which makes the sign of  $(c_{13}+c_{44})$  ambiguous; but, Tsvankin (2001) suggests that it is appropriate to choose the positive sign before the square root. They also places some limits on the values of Thomsen parameters

$$\begin{aligned}
-(1 - \beta^2 / \alpha^2) / 2 \leq \delta \leq 2 / (\alpha^2 / \beta^2 - 1), \\
\varepsilon > \delta, \\
\gamma > 0,
\end{aligned}$$

Where  $\alpha$  and  $\beta$  are P-wave and S-wave velocities in the direction of the symmetry axis (see figure 2.1).

The phase velocities for P-, SV-, and SH-waves are written conveniently as

$$\begin{aligned}
V_p(\theta) &\approx \alpha(1 + \delta \sin^2 \theta \cos^2 \theta + \varepsilon \sin^4 \theta), \\
V_{SV}(\theta) &\approx \beta(1 + \frac{\alpha^2}{\beta^2}(\varepsilon - \delta) \sin^2 \theta \cos^2 \theta), \\
V_{SH}(\theta) &\approx \beta(1 + \gamma \sin^2 \theta),
\end{aligned} \tag{2.14}$$

Where  $V_P$  is the phase velocity of P-wave,  $V_{SH}$  is the phase velocity of S-wave,  $V_{SV}$  is the phase velocity of the S-wave which polarized normal to the SH-wave, and  $\theta$  is the angle between the wave vector and  $x_3$ -axis or symmetry axis.

Berryman (2008) introduces another set of equations for P-wave and SV-wave velocities based on Thomsen's expressions in order to enhance the validity for wider

ranges of angle and stronger anisotropy. The expressions are

$$\begin{aligned} V_p(\theta) &\approx \alpha \left[ 1 + \varepsilon \sin^2 \theta - (\varepsilon - \delta) \frac{2 \sin^2 \theta_m \sin^2 \theta \cos^2 \theta}{1 - \cos 2\theta_m \cos 2\theta} \right], \\ V_{sv}(\theta) &\approx \beta \left[ 1 + \left( \frac{\alpha^2}{\beta^2} \right) (\varepsilon - \delta) \frac{2 \sin^2 \theta_m \sin^2 \theta \cos^2 \theta}{1 - \cos 2\theta_m \cos 2\theta} \right], \end{aligned} \quad (2.15)$$

where

$$\tan^2 \theta_m = \frac{c_{33} - c_{44}}{c_{11} - c_{44}}.$$

Berryman's formulas accurately predict the angle where the SV-wave has a maximum or minimum value, thus the phase velocity of SV-wave calculated by Berryman's formula has a more accurate result than the result obtained by Thomsen's equation. However, the phase velocity of P-wave calculated by Berryman's equation is not always more accurate. Thomsen's equation for P-wave is sometimes more accurate at small angles.

Based on the assumption of weakly anisotropic media, we defined the constant  $\varepsilon$  as the fractional difference between the P-wave velocities orthogonal and parallel to the symmetry axis

$$\varepsilon \approx \frac{V_p(90^\circ) - V_p(0^\circ)}{V_p(0^\circ)}. \quad (2.16)$$

Similarly, we defined the constant  $\gamma$  as the fractional difference between the SH-wave velocities orthogonal and parallel to the symmetry axis. And we also can describe it as the difference between the velocities of S-waves polarized normal and parallel to the symmetry axis, both propagating normal to the symmetry axis

$$\gamma \approx \frac{V_{SH}(90^\circ) - V_{SH}(0^\circ)}{V_{SH}(0^\circ)} = \frac{V_{SH}(90^\circ) - V_{SV}(90^\circ)}{V_{SV}(90^\circ)} . \quad (2.17)$$

Transversely isotropic media with a vertical symmetry axis (VTI) and transversely isotropic media with a horizontal symmetry axis (HTI) are of the same symmetry type, however the stiffness matrices for VTI media and HTI media are different because of the symmetry axes are perpendicular. The symmetry axis of VTI model is pointing in the  $x_3$ -direction and the symmetry axis of HTI model is pointing in the  $x_1$ -direction.

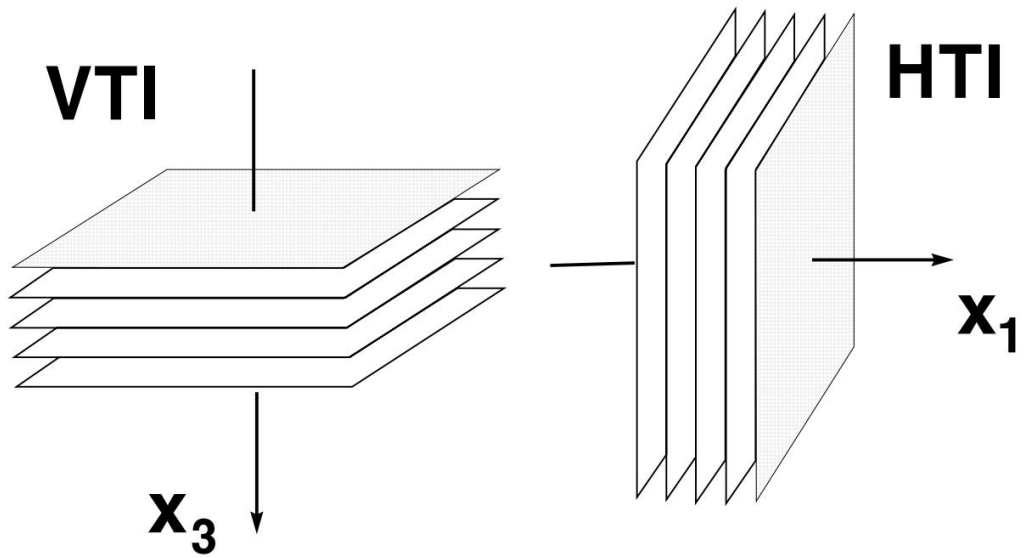


Figure 2.1. The symmetry axis for VTI and HTI models (Rüger, 2002).

However, they both have 5 parameters to specify the anisotropic medium

$$c_{VTI} = \begin{pmatrix} c_{11} & (c_{11} - 2c_{66}) & c_{13} & 0 & 0 & 0 \\ (c_{11} - 2c_{66}) & c_{11} & c_{13} & 0 & 0 & 0 \\ c_{13} & c_{13} & c_{33} & 0 & 0 & 0 \\ 0 & 0 & 0 & c_{55} & 0 & 0 \\ 0 & 0 & 0 & 0 & c_{55} & 0 \\ 0 & 0 & 0 & 0 & 0 & c_{66} \end{pmatrix}, \quad (2.18)$$

$$c_{HTI} = \begin{pmatrix} c_{11} & c_{13} & c_{13} & 0 & 0 & 0 \\ c_{13} & c_{33} & (c_{11} - 2c_{66}) & 0 & 0 & 0 \\ c_{13} & (c_{11} - 2c_{66}) & c_{33} & 0 & 0 & 0 \\ 0 & 0 & 0 & c_{44} & 0 & 0 \\ 0 & 0 & 0 & 0 & c_{55} & 0 \\ 0 & 0 & 0 & 0 & 0 & c_{55} \end{pmatrix}. \quad (2.19)$$

Because of the similarity between VTI and HTI media, we can use the equivalent

Thomsen's parameters to describe the HTI model as follows

$$\begin{aligned} \varepsilon^{(V)} &\equiv \frac{c_{11} - c_{33}}{2c_{33}}, \\ \delta^{(V)} &\equiv \frac{(c_{13} + c_{55})^2 - (c_{33} - c_{55})^2}{2c_{33}(c_{33} - c_{55})}, \\ \gamma^{(V)} &\equiv \frac{c_{66} - c_{44}}{2c_{44}}. \end{aligned} \quad (2.20)$$

Thomsen's HTI parameters can be related to the Thomsen's VTI parameters since the only difference between VTI and HTI is the direction of symmetry axis. So we can write

Thomsen's HTI parameter in terms of VTI parameters as

$$\begin{aligned}
\varepsilon^{(v)} &= -\frac{\varepsilon}{1+2\varepsilon}, \\
\delta^{(v)} &= \frac{\delta - 2\varepsilon(1 + \frac{\varepsilon}{f})}{(1+2\varepsilon)(1 + \frac{2\varepsilon}{f})}, \\
\gamma^{(v)} &= -\frac{\gamma}{1+2\gamma},
\end{aligned} \tag{2.21}$$

where

$$f \equiv 1 - (V_{S0}/V_{P0})^2.$$

$V_{P0}$  and  $V_{S0}$  are the velocities along the horizontal symmetry axis. Then we can make a short conclusion about the parameters for VTI medium and HTI medium in exact form and the approximate form (weak anisotropy) as shown in Table 2.1.

TABLE 2.1. Thomsen's equivalence for HTI media and its relation to the generic Thomsen parameters.

	Voigt notation	Generic Thomsen notation	Weak anisotropy
$\alpha$	$\sqrt{c_{33} / \rho}$	$V_{p0} \sqrt{1 + 2\varepsilon}$	$V_{p0}(1 + \varepsilon)$
$\beta$	$\sqrt{c_{44} / \rho}$	$V_{s0} \sqrt{1 + 2\gamma}$	$V_{s0}(1 + \gamma)$
$\beta^\perp$	$\sqrt{c_{55} / \rho}$	$V_{s0}$	$V_{s0}$
$\delta^{(v)}$	$\frac{(c_{13} + c_{55})^2 - (c_{33} - c_{55})^2}{2c_{33}(c_{33} - c_{55})}$	$\frac{\delta - 2\varepsilon(1 + \frac{\varepsilon}{f})}{(1 + 2\varepsilon)(1 + \frac{2\varepsilon}{f})}$	$\delta - 2\varepsilon$
$\varepsilon^{(v)}$	$\frac{c_{11} - c_{33}}{2c_{33}}$	$-\frac{\varepsilon}{1 + 2\varepsilon}$	$-\varepsilon$
$\gamma^{(v)}$	$\frac{c_{66} - c_{44}}{2c_{44}}$	$-\frac{\gamma}{1 + 2\gamma}$	$-\gamma$
$\gamma$	$\frac{c_{44} - c_{66}}{2c_{66}}$	$\gamma$	$\gamma$

*Note:* The  $c_{ij}$  corresponds to the symmetry axis pointing in the  $x_i$ -direction.  $\beta$  denotes SH-wave and  $\beta^\perp$  denotes SV-wave. The equations in the far right column are approximations in weak anisotropy media; all other expressions are exact.

## 2.7 Phase velocity and group velocity

Phase velocity and group velocity are two important concepts for anisotropic media. The raypath for the phase velocity is perpendicular to a surface of constant phase in anisotropic media. And the group velocity is the velocity with which the energy in the wavetrain travels (Sheriff, 1991). The relationship between phase velocity ( $V_p$ ) and group velocity ( $V_g$ ) can be written as

$$V_p = V_g \cdot \mathbf{n} \quad , \quad (2.22)$$

where  $\mathbf{n}$  is a unit vector along the wave normal.

Figure 2.2 illustrates the relationship between ray angle,  $\phi$ , and phase angle,  $\theta$ . The direction of the wave vector follows the direction that has the maximum rate of increase in phase. And the wave vector is always perpendicular to the wave front. However, the direction of the ray vector, which is the direction of energy propagation, is always from source to the wave front.

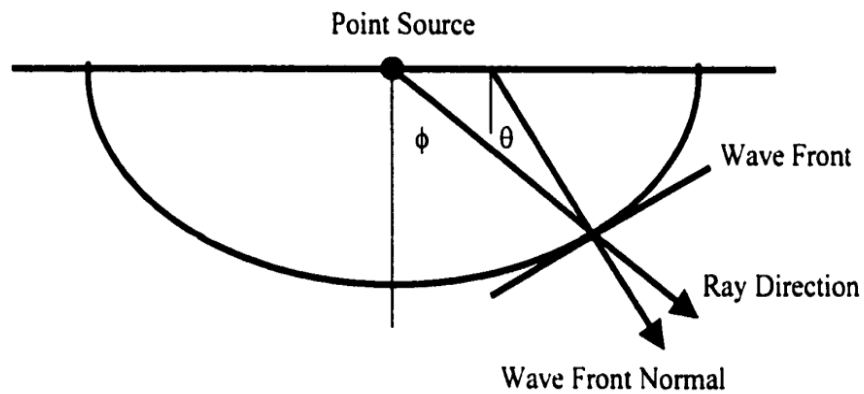


Figure 2.2. The relationship between phase angle and group angle (Chen, 2000).

Daley and Hron (1977, 1979) provide an analytic solution for phase velocity in a transversely isotropic medium with a vertical symmetry axis (VTI). To calculate the phase velocity for arbitrary anisotropy media, it is necessary to use the Green-Christoffel equation

$$[\Gamma_{ik} - \rho V^2 \delta_{ik}] U_k = 0, \quad (2.23)$$

where  $\rho$  is density,  $V$  is the phase velocity of the wave,  $\delta_{ik}$  is the Kronecker delta,  $U_k$  is the unit displacement, and  $\Gamma_{ik}$  is the Green-Christoffel second-rank symmetric tensor which equals

$$\Gamma_{ik} = C_{ijkl} n_j n_l, \quad (2.24)$$

where  $C_{ijkl}$  is the stiffness tensor of the medium and  $n$  is the wave direction (phase angle) for the incident wave. The Green-Christoffel equation has a unique solution when

$$\det(\Gamma_{ik} - \rho V^2 \delta_{ik}) = 0, \quad (2.25)$$

or in a matrix form

$$\begin{vmatrix} \Gamma_{11} - \rho V^2 & \Gamma_{12} & \Gamma_{13} \\ \Gamma_{12} & \Gamma_{22} - \rho V^2 & \Gamma_{23} \\ \Gamma_{13} & \Gamma_{23} & \Gamma_{33} - \rho V^2 \end{vmatrix} = 0. \quad (2.26)$$

In order to calculate the phase velocity, we have to solve the determinant of the equation.

The equation can be expanded as

$$C_3(\rho V^2)^3 + C_2(\rho V^2)^2 + C_1 \rho V^2 + C_0 = 0, \quad (2.27)$$

where

$$\begin{cases} C_0 = \Gamma_{11}\Gamma_{22}\Gamma_{33} + \Gamma_{12}\Gamma_{23}\Gamma_{31} + \Gamma_{13}\Gamma_{21}\Gamma_{32} - \Gamma_{31}\Gamma_{13}\Gamma_{22} - \Gamma_{23}\Gamma_{32}\Gamma_{11} - \Gamma_{21}\Gamma_{12}\Gamma_{33} \\ C_1 = \Gamma_{31}\Gamma_{13} + \Gamma_{23}\Gamma_{32} + \Gamma_{21}\Gamma_{12} - \Gamma_{11}\Gamma_{33} - \Gamma_{33}\Gamma_{22} - \Gamma_{22}\Gamma_{11} \\ C_2 = \Gamma_{11} + \Gamma_{22} + \Gamma_{33} \\ C_3 = -1 \end{cases} \quad (2.28)$$

Then we can solve for phase velocity  $V$  of the given incident angle by solving the cubic polynomial for  $\rho V^2$ .

Before calculating the group velocity, we have to solve the Green-Christoffel equation to obtain the polarization for the wave. We can write the Green-Christoffel equation in a component form

$$\begin{cases} (\Gamma_{11} - \rho V^2)U_1 + \Gamma_{12}U_2 + \Gamma_{13}U_3 = 0 \\ \Gamma_{12}U_1 + (\Gamma_{22} - \rho V^2)U_2 + \Gamma_{23}U_3 = 0 \\ \Gamma_{13}U_1 + \Gamma_{23}U_2 + (\Gamma_{33} - \rho V^2)U_3 = 0 \end{cases} \quad (2.29)$$

And we have one more equation comes from the definition of the normalized polarization

$$U_1^2 + U_2^2 + U_3^2 = 1 \quad (2.30)$$

In order to find  $U_i$ , we have to solve the Green-Christoffel equation. And to do this, let us rewrite it in a form

$$\begin{cases} \frac{(\Gamma_{11} - \rho V^2) U_1}{\Gamma_{13} U_3} + \frac{\Gamma_{12} U_2}{\Gamma_{13} U_3} + 1 = 0 \\ \frac{\Gamma_{12} U_1}{\Gamma_{23} U_3} + \frac{(\Gamma_{22} - \rho V^2) U_2}{\Gamma_{23} U_3} + 1 = 0 \\ \frac{\Gamma_{13} U_1}{(\Gamma_{33} - \rho V^2) U_3} + \frac{\Gamma_{23} U_2}{(\Gamma_{33} - \rho V^2) U_3} + 1 = 0 \end{cases}, \quad (2.31)$$

or

$$\begin{cases} A_{11}x_1 + A_{12}x_2 = -1 \\ A_{21}x_1 + A_{22}x_2 = -1 \\ A_{31}x_1 + A_{32}x_2 = -1 \end{cases}, \quad (2.32)$$

where

$$\begin{cases} x_1 = \frac{U_1}{U_3}, x_2 = \frac{U_2}{U_3} \\ A_{11} = \frac{(\Gamma_{11} - \rho V^2)}{\Gamma_{13}}, A_{12} = \frac{\Gamma_{12}}{\Gamma_{13}} \\ A_{21} = \frac{\Gamma_{12}}{\Gamma_{23}}, A_{22} = \frac{(\Gamma_{22} - \rho V^2)}{\Gamma_{23}} \\ A_{31} = \left( \frac{(\Gamma_{33} - \rho V^2)}{\Gamma_{13}} \right)^{-1}, A_{32} = \left( \frac{(\Gamma_{33} - \rho V^2)}{\Gamma_{23}} \right)^{-1} \end{cases}.$$

The first two equations above yield

$$\begin{cases} A_{11}x_1 + A_{12}x_2 = -1 \\ A_{21}x_1 + A_{22}x_2 = -1 \end{cases}, \quad (2.33)$$

and

$$\begin{cases} x_1 = \frac{U_1}{U_3} = \frac{A_{12} - A_{22}}{A_{11}A_{22} - A_{21}A_{12}} \\ x_2 = \frac{U_2}{U_3} = \frac{A_{21} - A_{11}}{A_{11}A_{22} - A_{21}A_{12}} \\ x_3 = \frac{U_1}{U_2} = \frac{x_1}{x_2} = \frac{A_{12} - A_{22}}{A_{21} - A_{11}} \end{cases}. \quad (2.34)$$

From the above equations, we find

$$\begin{cases} U_1 = x_1 U_3 \\ U_2 = x_2 U_3 \\ U_3 = \frac{1}{x_1} U_1 \end{cases} \quad (2.35)$$

Using the above equation and the definition of normalized polarization, we obtain

$$(x_1^2 + x_2^2 + 1)U_3^2 = 1, \quad (2.36)$$

and

$$U_3^2 = \frac{1}{(x_1^2 + x_2^2 + 1)}. \quad (2.37)$$

Analogously, for  $U_1$  and  $U_2$

$$\begin{cases} U_1^2 = \frac{1}{\left(\frac{x_2}{x_1}\right)^2 + \left(\frac{1}{x_1}\right)^2 + 1} \\ U_2^2 = \frac{1}{\left(\frac{x_1}{x_2}\right)^2 + \left(\frac{1}{x_2}\right)^2 + 1} \end{cases} \quad (2.38)$$

Thus the three components  $U_1$ ,  $U_2$ , and  $U_3$  of the polarization have been obtained.

Knowing the phase velocity and polarization, the group velocity can be calculated. Group

velocity is defined as  $V_g = \frac{\partial \omega}{\partial k}$ . From the second Green-Christoffel equation, we have

$$C_{ijkl} n_j n_l U_i = \rho V^2 U_k. \quad (2.39)$$

And we multiply  $U_k$  and  $\frac{4\pi^2}{\lambda^2}$  on both side of above equation, we obtain

$$C_{ijkl}U_i k_j k_l U_k = \rho\omega^2 \quad (2.40)$$

After differentiation with respect to  $k$  and using the definition of the group velocity, we can write the group velocity in terms of the phase velocity as

$$V_g = \frac{\partial\omega}{\partial k} = \frac{1}{\rho V} C_{ijkl} U_i U_k n_l \quad (2.41)$$

It is necessary to introduce the second Green-Christoffel tensor here to simplify the equation for group velocity. The second Green-Christoffel tensor can be written as:

$$G_{jl} = C_{ijkl} U_i U_k, \quad (2.42)$$

where  $C_{ijkl}$  is the stiffness tensor for the medium and,  $U_i$  and  $U_k$  are two components of the polarization. Then the group velocity has the form

$$V_g = \frac{\partial\omega}{\partial k} = \frac{1}{\rho V} G_{jl} n_l \quad (2.43)$$

Illite which has VTI symmetry is used to illustrate how the phase and group velocities change with respect to the angles measured from the three axes (see Figure 2.3 and Figure 2.4). From the three-dimensional plots of phase and group velocities, it is obvious that triplication occurs in the group velocity for SV-wave. It is difficult to understand this phenomenon in the symmetry models lower than TI and its significance to seismic interpretation.

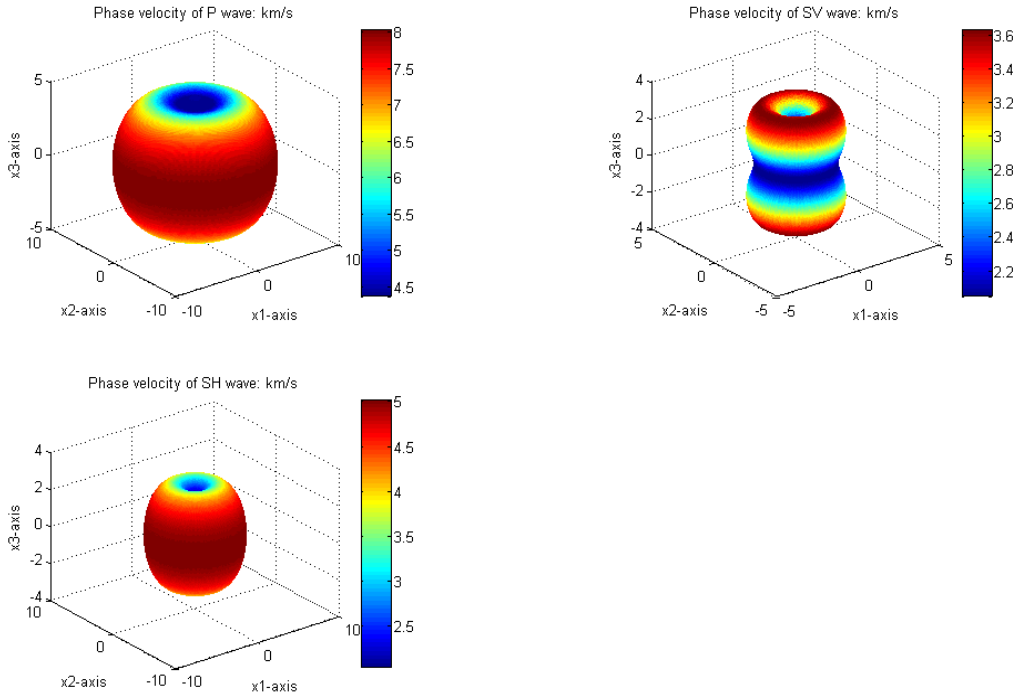


Figure 2.3. The phase velocities of P-wave, SV-wave, and SH-wave for illite. The elastic constants for illite are given in Appendix A.

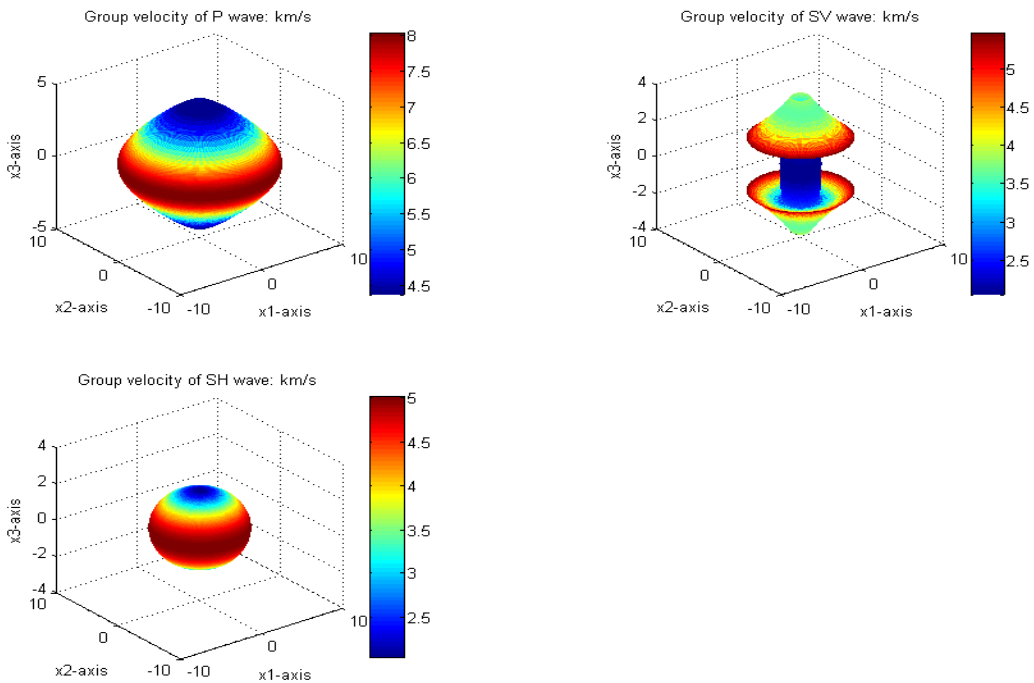


Figure 2.4. The group velocities of P-wave, SV-wave, and SH-wave for illite. The elastic constants for illite are given in Appendix A.

## 2.8 Conclusion

For both isotropic and anisotropic media, the relationship between stress and strain can be expressed by the Hooke's law. Voigt notation, which is the abbreviated notation, is used to simplify the  $3 \times 3 \times 3 \times 3$  stiffness tensor into  $6 \times 6$  stiffness matrix. Because of the symmetry property, only 21 independent elastic constants are required to specify the lowest symmetry model (triclinic model). Thomsen's notation, which contains three anisotropy parameters, can be used to describe TI media. In order to obtain phase and group velocities for arbitrary anisotropic media, the first and second Green-Christoffel equations need to be used.

## CHAPTER 3

# REFLECTION AND TRANSMISSION COEFFICIENTS FOR ANISOTROPIC MEDIA

### 3.1 Introduction

Reflection and transmission phenomenon of elastic waves is considered to be the hot topic for the past several years in the field of exploration seismology, especially in the area of amplitude-versus-offset (AVO) technology. When fractures are embedded in an isotropic host rock, azimuthal amplitude-versus-offset (AVOZ) technology is widely used for predicting the properties of fractures. Depending on the accuracy required, it can be significantly more difficult to calculate the reflection and transmission coefficients in anisotropic media compared to isotropic media. The propagation of body waves and surface waves in anisotropic media are different from their propagation in isotropic media because velocity in anisotropic media is dependent on the direction of propagation.

In Chapter 2, the method to solve for phase velocity and polarization are discussed. In this chapter, two different methods are presented for calculating anisotropic reflection and transmission coefficients for a plane wave at the interface between two arbitrary anisotropic half-spaces. The often used Rüger's linear approximation for PP reflection coefficients for transversely isotropic media with a horizontal axis (HTI) is also included in this chapter.

### 3.2 Reflection and transmission coefficients (Chattopadhyay)

The following development for the anisotropic reflection and transmission coefficients was developed by Chattopadhyay (2004).

For a half-space model with two arbitrary anisotropic layers (see Figure 3.1), we assume the upper layer is the region  $x_3 \leq 0$  and the lower layer is the region  $x_3 \geq 0$ . A quasi-P-wave is incident at the surface of the boundary  $x_3 = 0$ .

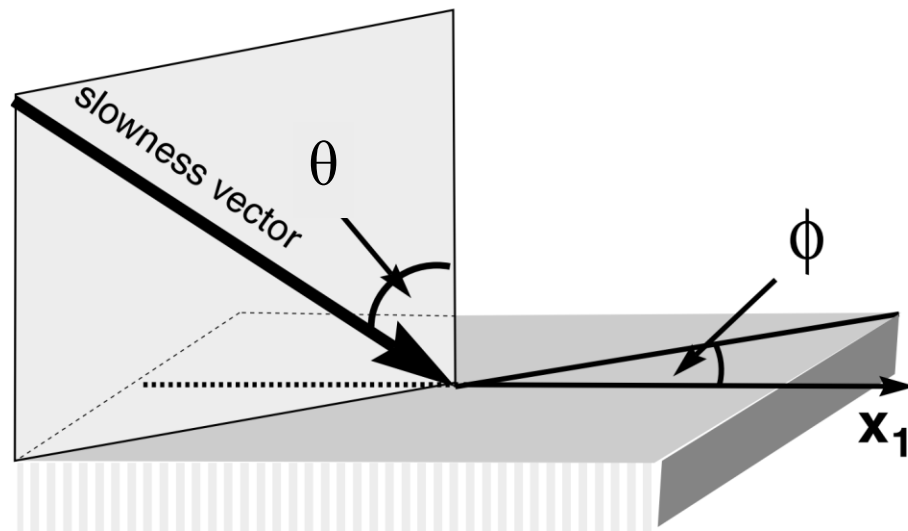


Figure 3.1. Scheme of an incident wave hits an interface.  $\theta$  denotes the angle between the slowness vector of the incident wave and vertical axis.  $\phi$  is the azimuthal angle which is defined with respect to the symmetry axis pointing in the  $x_1$ -direction (Rüger, 2002).

The incident wave generates three reflected waves which are quasi-P-wave, fast quasi-S-wave, and slow quasi-S-wave in the upper layer and three transmitted waves which are quasi-P-wave, fast quasi-S-wave, and slow quasi-S-wave in the lower layer. We assume  $n = 0, 1, 2, 3, 4, 5, 6$  are for the incident quasi-P-wave, reflected quasi-P-wave, fast quasi-S-wave, and slow quasi-S-wave and transmitted quasi-P-wave, fast quasi-S-

wave, and slow quasi-S-wave respectively. The angles made by the incident quasi-P-wave, reflected quasi-P-wave, fast quasi-S-wave, and slow quasi-S-wave and transmitted quasi-P-wave, fast-quasi-S wave, and slow quasi-S-wave with the  $x_3$ -axis which is vertically downward are  $\theta_0, \theta_1, \theta_2, \theta_3, \theta_4, \theta_5$ , and  $\theta_6$ , respectively (see Figure 3.2).

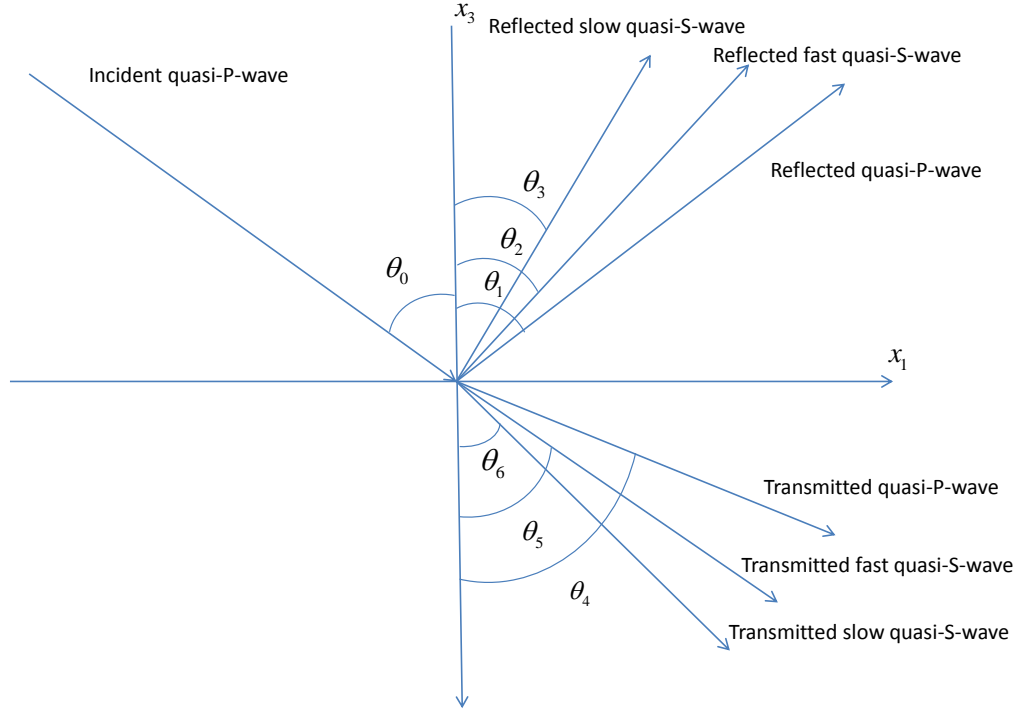


Figure 3.2. Reflected and transmitted waves caused by an incident quasi-P-wave hits the interface between two anisotropic half-spaces.

At the interface where  $x_3 = 0$ , the displacement and stress of waves in both half-spaces are written in the following forms

$$\begin{pmatrix} u_1^n \\ u_2^n \\ u_3^n \end{pmatrix} = A_n \begin{pmatrix} d_1^n \\ d_2^n \\ d_3^n \end{pmatrix} e^{ik_n(x_1 p_1^n + x_2 p_2^n + x_3 p_3^n - c_n t)} \quad , \quad (3.1)$$

$$\begin{aligned}
\sigma_{13} &= C_{13kl} \varepsilon_{kl} = ik_n A_n e^{ik_n(x_1 p_1^n + x_2 p_2^n + x_3 p_3^n - c_n t)} P_n, \\
\sigma_{23} &= C_{23kl} \varepsilon_{kl} = ik_n A_n e^{ik_n(x_1 p_1^n + x_2 p_2^n + x_3 p_3^n - c_n t)} Q_n, \\
\sigma_{33} &= C_{33kl} \varepsilon_{kl} = ik_n A_n e^{ik_n(x_1 p_1^n + x_2 p_2^n + x_3 p_3^n - c_n t)} R_n,
\end{aligned} \tag{3.2}$$

where

$$\begin{aligned}
P_n &= c_{51} p_1^n d_1^n + c_{52} p_2^n d_2^n + c_{53} p_3^n d_3^n + c_{54} (p_3^n d_2^n + p_2^n d_3^n) \\
&\quad + c_{55} (p_3^n d_1^n + p_1^n d_3^n) + c_{56} (p_2^n d_1^n + p_1^n d_2^n), \\
Q_n &= c_{41} p_1^n d_1^n + c_{42} p_2^n d_2^n + c_{43} p_3^n d_3^n + c_{44} (p_3^n d_2^n + p_2^n d_3^n) \\
&\quad + c_{45} (p_3^n d_1^n + p_1^n d_3^n) + c_{46} (p_2^n d_1^n + p_1^n d_2^n), \\
R_n &= c_{31} p_1^n d_1^n + c_{32} p_2^n d_2^n + c_{33} p_3^n d_3^n + c_{34} (p_3^n d_2^n + p_2^n d_3^n) \\
&\quad + c_{35} (p_3^n d_1^n + p_1^n d_3^n) + c_{36} (p_2^n d_1^n + p_1^n d_2^n),
\end{aligned} \tag{3.3}$$

and

$$n = \begin{cases} 0: \text{incident quasi-P-wave} \\ 1: \text{reflected quasi-P-wave} \\ 2: \text{reflected fast quasi-S-wave} \\ 3: \text{reflected slow quasi-S-wave} \\ 4: \text{transmitted quasi-P-wave} \\ 5: \text{transmitted fast quasi-S-wave} \\ 6: \text{transmitted slow quasi-S-wave} \end{cases}$$

$p$  denotes the unit propagation vector,  $d$  is the component of a unit displacement vector, and  $c_n$  is the phase velocity of the incident quasi-P-wave, reflected quasi-P-wave, fast quasi-S-wave, and slow quasi-S-wave and transmitted quasi-P-wave, fast quasi-S-wave, and slow quasi-S-wave. The capital  $C$  here denotes the fourth-rank stiffness tensor and the miniscule  $c$  is used for the Voigt notation.

For  $n=4, 5,$  and  $6,$  which denote the waves in the lower medium, the elastic constants  $c_{ij}$  are to be replaced by  $c_{ij}'$  and then equations (3.1), (3.2), and (3.3) can be written for the transmitted waves in the lower half-space.

The boundary conditions at  $x_3 = 0$  can be written as

$$\begin{aligned}
 u_1^I &= u_1^{II} \\
 u_2^I &= u_2^{II} \\
 u_3^I &= u_3^{II} \\
 \sigma_{13}^I &= \sigma_{13}^{II} \\
 \sigma_{23}^I &= \sigma_{23}^{II} \\
 \sigma_{33}^I &= \sigma_{33}^{II},
 \end{aligned} \tag{3.4}$$

where  $I$  denotes the upper half-space and  $II$  denotes the lower half-space. When one plane wave is considered at the interface, we can write the equation as

$$\begin{aligned}
 u_1^0 + u_1^1 + u_1^2 + u_1^3 &= u_1^4 + u_1^5 + u_1^6 \\
 u_2^0 + u_2^1 + u_2^2 + u_2^3 &= u_2^4 + u_2^5 + u_2^6 \\
 u_3^0 + u_3^1 + u_3^2 + u_3^3 &= u_3^4 + u_3^5 + u_3^6 \\
 \sigma_{13}^0 + \sigma_{13}^1 + \sigma_{13}^2 + \sigma_{13}^3 &= \sigma_{13}^4 + \sigma_{13}^5 + \sigma_{13}^6 \\
 \sigma_{23}^0 + \sigma_{23}^1 + \sigma_{23}^2 + \sigma_{23}^3 &= \sigma_{23}^4 + \sigma_{23}^5 + \sigma_{23}^6 \\
 \sigma_{33}^0 + \sigma_{33}^1 + \sigma_{33}^2 + \sigma_{33}^3 &= \sigma_{33}^4 + \sigma_{33}^5 + \sigma_{33}^6.
 \end{aligned} \tag{3.5}$$

By substituting the displacement and stress into boundary conditions, we have

$$\begin{pmatrix} \frac{d_1^1}{d_1^0} & \frac{d_1^2}{d_1^0} & \frac{d_1^3}{d_1^0} & -\frac{d_1^4}{d_1^0} & -\frac{d_1^5}{d_1^0} & -\frac{d_1^6}{d_1^0} \\ \frac{d_2^1}{d_2^0} & \frac{d_2^2}{d_2^0} & \frac{d_2^3}{d_2^0} & -\frac{d_2^4}{d_2^0} & -\frac{d_2^5}{d_2^0} & -\frac{d_2^6}{d_2^0} \\ \frac{d_3^1}{d_3^0} & \frac{d_3^2}{d_3^0} & \frac{d_3^3}{d_3^0} & -\frac{d_3^4}{d_3^0} & -\frac{d_3^5}{d_3^0} & -\frac{d_3^6}{d_3^0} \\ \frac{P_1 k_1}{P_0 k_0} & \frac{P_2 k_2}{P_0 k_0} & \frac{P_3 k_3}{P_0 k_0} & -\frac{P_4 k_4}{P_0 k_0} & -\frac{P_5 k_5}{P_0 k_0} & -\frac{P_6 k_6}{P_0 k_0} \\ \frac{Q_1 k_1}{Q_0 k_0} & \frac{Q_2 k_2}{Q_0 k_0} & \frac{Q_3 k_3}{Q_0 k_0} & -\frac{Q_4 k_4}{Q_0 k_0} & -\frac{Q_5 k_5}{Q_0 k_0} & -\frac{Q_6 k_6}{Q_0 k_0} \\ \frac{R_1 k_1}{R_0 k_0} & \frac{R_2 k_2}{R_0 k_0} & \frac{R_3 k_3}{R_0 k_0} & -\frac{R_4 k_4}{R_0 k_0} & -\frac{R_5 k_5}{R_0 k_0} & -\frac{R_6 k_6}{R_0 k_0} \end{pmatrix} \begin{pmatrix} A_1 \\ A_2 \\ A_3 \\ A_4 \\ A_5 \\ A_6 \end{pmatrix} = \begin{pmatrix} -1 \\ -1 \\ -1 \\ -1 \\ -1 \\ -1 \end{pmatrix}, \quad (3.6)$$

where  $k_n$  is the wave number for three reflected waves and three transmitted waves, and  $d_n^m$  denotes the  $n$ -th component of the unit displacement for the  $m$ -th type wave.  $A_n$  is the reflection or transmission coefficients for three reflected waves and three transmitted waves. In order to obtain these coefficients, solve the inversion of the matrix.

### 3.3 Reflection and transmission coefficients (Schoenberg and Protazio)

Our second method for computing anisotropic reflection and transmission coefficients was introduced by Schoenberg and Protazio (1992). This solution involves submatrices of the coefficient matrix for the Zoeppritz equation. Before the submatrices are obtained, we need to calculate the slowness of three reflected waves and three transmitted waves, because Snell's law predicts that the two components of the slowness, which are parallel to the interface, are the same for all waves: incident, reflected, and transmitted. There is one very important assumption made and that is the frequency and

phase of the reflected and transmitted waves are equal to that of the incident wave. Based on this assumption, we can obtain the relationship for two components of the slowness,  $s$ , which are parallel to the interface as follows

$$\begin{cases} s_1^0 = s_1^1 = s_1^2 = s_1^3 = s_1^4 = s_1^5 = s_1^6 \\ s_2^0 = s_2^1 = s_2^2 = s_2^3 = s_2^4 = s_2^5 = s_2^6 \end{cases}, \quad (3.7)$$

where  $m$  and  $n$  in  $s_m^n$  denote the component of the slowness and the type of wave. The number  $n$  from 0 to 6 are incident wave, reflected quasi-P-wave, fast quasi-S-wave, and slow quasi-S-wave as well as transmitted quasi-P-wave, fast quasi-S-wave, and slow quasi-S-wave. The third components  $s_3^n$  ( $n=1, 2, \dots, 6$ ) are perpendicular to the interface, and these are the only parameters we are going to calculate. They can be obtained by solving a sixth-order equation which is from Green-Christoffel equation but in terms of slowness

$$[\Gamma_{ik}(s) - \rho I]U_i = 0, \quad (3.8)$$

where

$$\Gamma_{ik} = C_{ijkl}s_i s_k.$$

The above equation can be written in the following form

$$D_{ik}s_3^2 + E_{ik}s_3 + F_{ik} = \Gamma_{ik}(s) - \rho I, \quad (3.9)$$

where

$$\begin{cases} D_{ik} = \frac{C_{i3k3}}{\rho} \\ E_{ik} = \frac{(C_{i1k3} + C_{i3k1})s_1 + (C_{i2k3} + C_{i3k2})s_2}{\rho} \\ F_{ik} = \frac{(C_{i1k2} + C_{i2k1})s_1 s_2 + C_{i1k1}s_1^2 + C_{i2k2}s_2^2}{\rho} + \delta_{ik} \end{cases}$$

We can write the equation (3.9) in matrix as follows and solve the determinant of the matrix in order to obtain the  $s_3$

$$\begin{vmatrix} D_{11}s_3^2 + E_{11}s_3 + F_{11} & D_{12}s_3^2 + E_{12}s_3 + F_{12} & D_{13}s_3^2 + E_{13}s_3 + F_{13} \\ D_{21}s_3^2 + E_{21}s_3 + F_{21} & D_{22}s_3^2 + E_{22}s_3 + F_{22} & D_{23}s_3^2 + E_{23}s_3 + F_{23} \\ D_{31}s_3^2 + E_{31}s_3 + F_{31} & D_{32}s_3^2 + E_{32}s_3 + F_{32} & D_{33}s_3^2 + E_{33}s_3 + F_{33} \end{vmatrix} = 0 \quad (3.10)$$

The determinant of the matrix can be written as a sixth-order equation and thus there will be six roots for the equation, denoted by  $\pm\sqrt{s_{3p}^2}$ ,  $\pm\sqrt{s_{3s1}^2}$ ,  $\pm\sqrt{s_{3s2}^2}$ , with their associated polarization respectively. As convention for  $s_{3p}^2$ ,  $s_{3s1}^2$ , and  $s_{3s2}^2$ ,

$$s_{3p}^2 < s_{3s1}^2 < s_{3s2}^2,$$

where  $s_{3i}$  is the vertical slowness component for the  $i$ -th type wave. Any imaginary values for the vertical slowness component indicate that the corresponding wave is inhomogeneous or evanescent (Schoenberg and Protazio, 1992). The impedance matrices can be written as:

$$\begin{aligned}
X &= \begin{bmatrix} e_{1p} & e_{1s1} & e_{1s2} \\ e_{1p} & e_{2s1} & e_{2s2} \\ \{-(c_{13}e_{1p} + c_{36}e_{2p})s_1 & \{-(c_{13}e_{1s1} + c_{36}e_{2s1})s_1 & \{-(c_{13}e_{1s2} + c_{36}e_{2s2})s_1 \\ -(c_{23}e_{2p} + c_{36}e_{1p})s_2 & -(c_{23}e_{2s1} + c_{36}e_{1s1})s_2 & -(c_{23}e_{2s2} + c_{36}e_{1s2})s_2 \\ -c_{33}e_{3p}s_{3p}\} & -c_{33}e_{3s1}s_{3s1}\} & -c_{33}e_{3s2}s_{3s2}\} \end{bmatrix}, \\
Y &= \begin{bmatrix} \{-(c_{55}s_1 + c_{45}s_2)e_{3p} & \{-(c_{55}s_1 + c_{45}s_2)e_{3s1} & \{-(c_{55}s_1 + c_{45}s_2)e_{3s2} \\ -(c_{55}e_{1p} + c_{45}e_{2p})s_{3p}\} & -(c_{55}e_{1s1} + c_{45}e_{2s1})s_{3s1}\} & -(c_{55}e_{1s2} + c_{45}e_{2s2})s_{3s2}\} \\ \{-(c_{45}s_1 + c_{44}s_2)e_{3p} & \{-(c_{45}s_1 + c_{44}s_2)e_{3s1} & \{-(c_{45}s_1 + c_{44}s_2)e_{3s2} \\ -(c_{45}e_{1p} + c_{44}e_{2p})s_{3p}\} & -(c_{45}e_{1s1} + c_{44}e_{2s1})s_{3s1}\} & -(c_{45}e_{1s2} + c_{44}e_{2s2})s_{3s2}\} \\ e_{3p} & e_{3s1} & e_{3s2} \end{bmatrix}, \\
\end{aligned} \tag{3.11}$$

where  $s_1$  and  $s_2$  are the horizontal components of the slowness which are constant for the incident, reflected, and transmitted wave;  $s_{3p}$ ,  $s_{3s1}$ , and  $s_{3s2}$  are the vertical components of the slowness for quasi-P-wave, fast quasi-S-wave, and slow quasi-S-wave;  $e_{ip}$ ,  $e_{is1}$ , and  $e_{is2}$  are the  $i$ -th components of the associated eigenvectors calculated by Green-Christoffel equation; and  $c_{ij}$  are the elements of stiffness matrix in Voigt notation.  $X'$  and  $Y'$ , which are the impedance matrices for the lower medium, have the same form but all the parameters of the upper half-space are replaced with parameters of lower half-space.

$T$  and  $R$  are the solutions of Zoeppritz equation can be written as

$$\begin{aligned}
T &= 2(X^{-1}X' + Y^{-1}Y')^{-1}, \\
R &= (X^{-1}X' - Y^{-1}Y')(X^{-1}X' + Y^{-1}Y')^{-1}, \\
\end{aligned} \tag{3.12}$$

where  $T$  and  $R$  are the transmission and reflection coefficient matrices.  $T$  and  $R$  can be expressed as

$$R = \begin{bmatrix} R_{pp} & R_{s1p} & R_{s2p} \\ R_{ps1} & R_{s1s1} & R_{s2s1} \\ R_{ps2} & R_{s1s2} & R_{s2s2} \end{bmatrix}, \quad T = \begin{bmatrix} T_{pp} & T_{s1p} & T_{s2p} \\ T_{ps1} & T_{s1s1} & T_{s2s1} \\ T_{ps2} & T_{s1s2} & T_{s2s2} \end{bmatrix}, \quad (3.13)$$

where the first subscript denotes the type of incident wave and the second subscript denotes the type of reflected or transmitted wave. And we assume that  $X$  and  $Y$  are singular and  $X'$  and  $Y'$  are invertible, the solutions can finally be written as

$$\begin{aligned} R &= (Y'^{-1}Y + X'^{-1}X)^{-1}(Y'^{-1}Y - X'^{-1}X) \\ T &= 2X'^{-1}X(Y'^{-1}Y + X'^{-1}X)^{-1}Y'^{-1}Y \\ \text{or} \\ T &= 2Y'^{-1}Y(Y'^{-1}Y + X'^{-1}X)^{-1}X'^{-1}X \end{aligned} \quad (3.14)$$

The limitation of this method is we can only use these formulas to calculate the reflection and transmission coefficients when both upper and lower half-spaces have at least monoclinic symmetry with a horizontal symmetry plane (Mavko *et al.*, 2009). Numerical tests of exact reflection coefficients are shown in Figures 3.3 to 3.5.

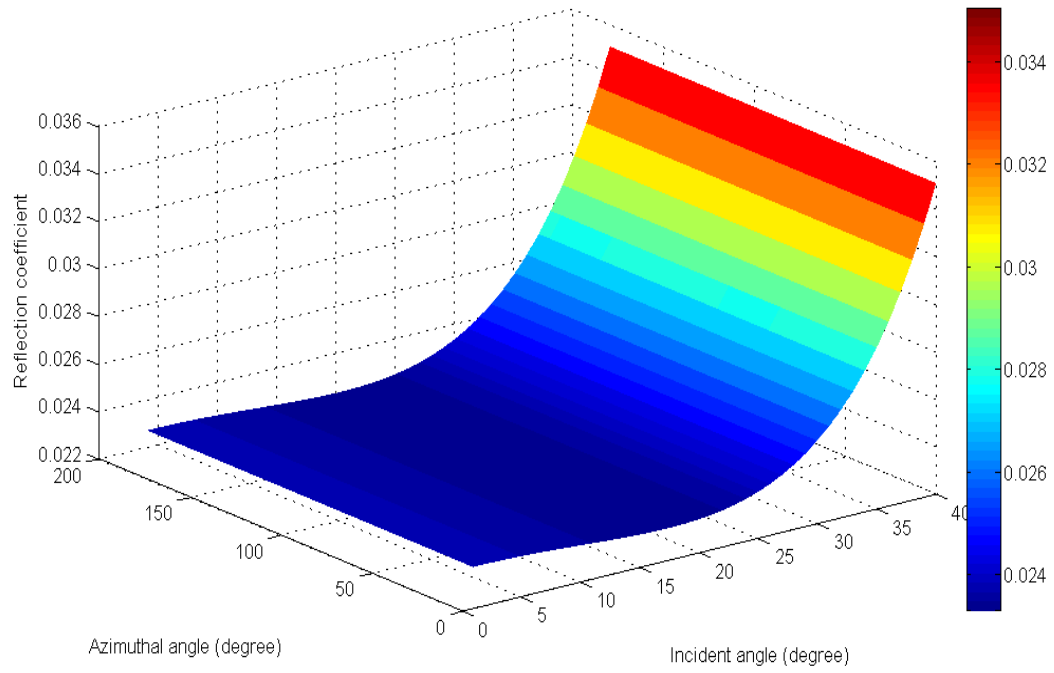


Figure 3.3. Exact reflection coefficients for an isotropic half-space over a VTI half-space with elastic constants given in Appendix B.

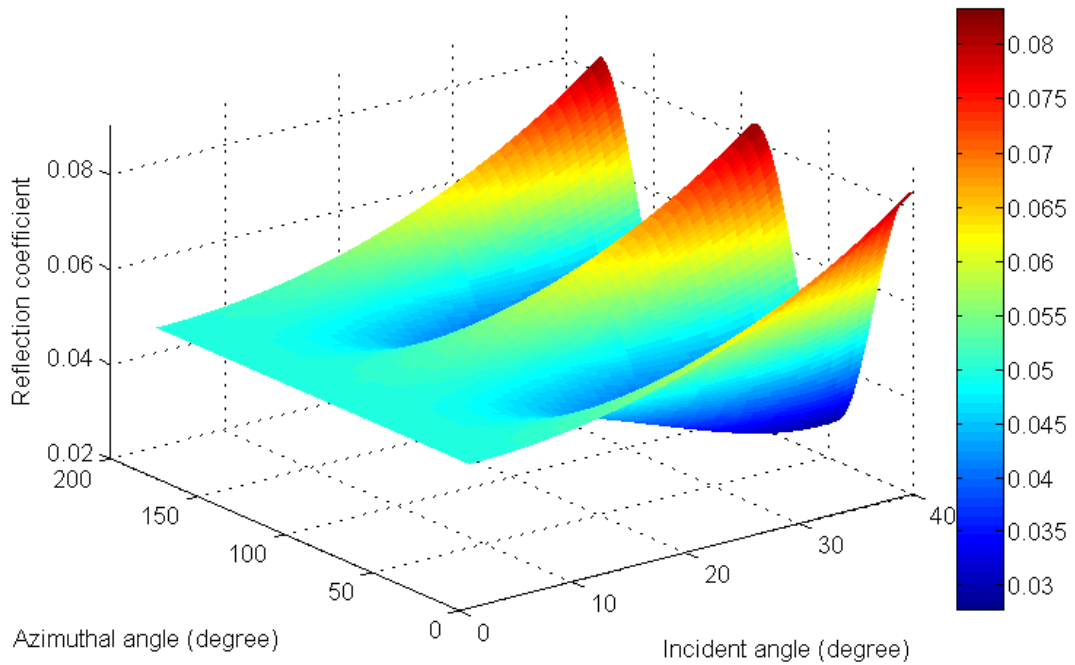


Figure 3.4. Exact reflection coefficients for an isotropic half-space over a HTI half-space with elastic constants given in Appendix B.

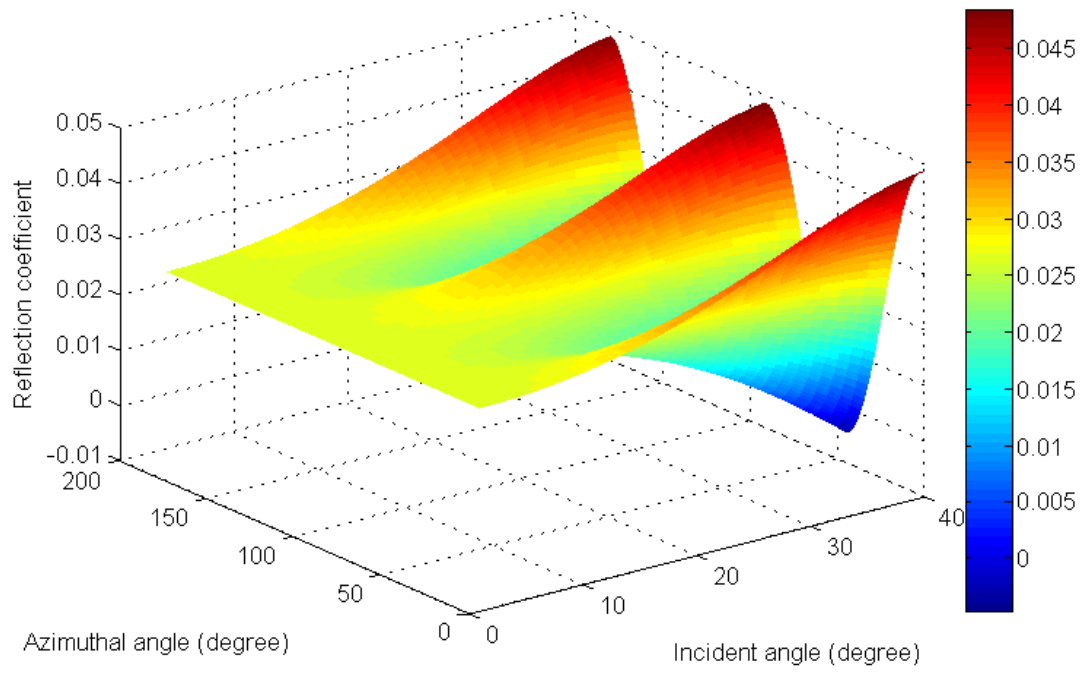


Figure 3.5. Exact reflection coefficients for a VTI half-space over a HTI half-space with elastic constants given in Appendix B.

Figure 3.3 shows the exact reflection coefficients for an isotropic half-space over a VTI half-space. The phase velocity in the VTI medium does not change with azimuth, thus the reflection coefficients in Figure 3.3 are azimuthally invariant. The exact reflection coefficients for an isotropic half-space over a HTI half-space are illustrated in Figure 3.4. The coefficients vary with both incident angle and azimuthal angle. The azimuthal variation has a constant period due to the special properties of the lower HTI half-space. So analyzing these variations, caused by incident angle and azimuthal angle, will give us an instructive view of the interface. Figure 3.5 has similar variation trends to that of Figure 3.4. The difference of models used in Figure 3.4 and Figure 3.5 is the upper half-space. An isotropic medium is used in Figure 3.4 as the upper half-space while a VTI medium is used in Figure 3.5. Values in Figure 3.5 are smaller than that in Figure 3.4 and the lowest value even goes down to negative. For the case like shown in Figure 3.5 which is an anisotropic half-space over another anisotropic half-space with different symmetry model is very difficult to recover the elastic information about the upper and lower half-space.

### **3.4 Reflection coefficient approximations for HTI media (Rüger)**

The analytic expressions for exact and approximate reflection coefficients have been studied for a long time. But most of these studies are focused on VTI models (Daley and Hron, 1977; Banik, 1987; Graebner, 1992; Thomsen, 1993; Blangy, 1994). However, Rüger (2002) introduces both the exact and approximate reflection coefficients for HTI models. When a plane P-wave is incident on an interface, three plane waves with different polarization directions in the lower HTI half-space will be generated if the

incident wave is outside either the vertical symmetry plane or the isotropic plane (Rüger, 1997). The three waves are:

- A quasi-P-wave. The polarization of this wave has a slight deviation angle from its propagating direction.
- A quasi-SV-wave. The polarization of this wave is in the plane formed by the slowness vector and the symmetry axis.
- A quasi-SH-wave. The polarization of quasi-SH-wave is orthogonal to the quasi-P-wave and quasi-SV-wave and it is within the isotropic plane.

Based on the assumption that the anisotropic media is weakly anisotropy, Rüger derived the approximate compressional plane wave reflection coefficient as the function of incident and azimuthal phase angles

$$R_{PP}^{HTI}(i, \phi) = \frac{1}{2} \frac{\Delta Z}{\bar{Z}} + \frac{1}{2} \left\{ \frac{\Delta \alpha}{\bar{\alpha}} - \left( \frac{2\bar{\beta}}{\bar{\alpha}} \right)^2 \frac{\Delta G}{\bar{G}} + \left[ \Delta \delta^{(V)} + 2 \left( \frac{2\bar{\beta}}{\bar{\alpha}} \right)^2 \Delta \gamma \right] \cos^2 \phi \right\} \sin^2 i + \frac{1}{2} \left\{ \frac{\Delta \alpha}{\bar{\alpha}} + \Delta \varepsilon^{(V)} \cos^4 \phi + \Delta \delta^{(V)} \sin^2 \phi \cos^2 \phi \right\} \sin^2 i \tan^2 i \quad (3.15)$$

where

$$\begin{aligned} \beta &= \sqrt{\frac{C_{44}}{\rho}}, \\ \alpha &= \sqrt{\frac{C_{33}}{\rho}}, \\ G &= \rho \beta^2, \\ Z &= \rho \alpha. \end{aligned}$$

And  $i$  is the incident phase angle and  $\phi$  is the azimuthal phase angle with the symmetry axis. All the elastic constants are written in their average values and relative differences across the interface. For example

$$\bar{\alpha} = \frac{(\alpha_1 + \alpha_2)}{2},$$

$$\Delta\alpha = (\alpha_2 - \alpha_1).$$

Note that  $\alpha$  and  $\beta$  in Thomsen's notation denote the P-wave and S-wave velocities propagating along the symmetry axis. However, here we use  $\alpha$  and  $\beta$  to represent the P-wave and SH-wave velocities propagating in the isotropic plane.

Before quickly using this approximation, it is instructive first to compare some exact reflection coefficients with their approximations. Model parameters listed in Table 3.1 are used. By analyzing the difference between exact reflection coefficients and the approximations with different anisotropy, it is easy to study the accuracy of the approximation equation.

TABLE 3.1. Model parameters used to study the accuracy of the approximation equation.

Model	$\frac{\Delta\alpha}{\bar{\alpha}}$	$\frac{\Delta Z}{\bar{Z}}$	$\frac{\Delta G}{\bar{G}}$	$\delta^{(v)}$	$\varepsilon^{(v)}$	$\gamma$
A	0.1	0.1	0.2	0	0	0.1
B	0.1	0.1	0.2	-0.1	0	0
C	0.1	0.1	0.2	0	-0.1	0
D	0.1	0.1	0.2	-0.05	-0.05	0.15

*Note:* The model has an isotropic half-space on the top and an anisotropic half-space on the bottom with the following parameters: vertical P-wave velocity in the isotropic plane  $\alpha_2 = 2.5$ , vertical SH-wave velocity in the isotropic plane  $\beta_2 = 1.5$  and  $\rho_2 = 2.7$ . The units for velocity and density are km/s and g/cm<sup>3</sup>.

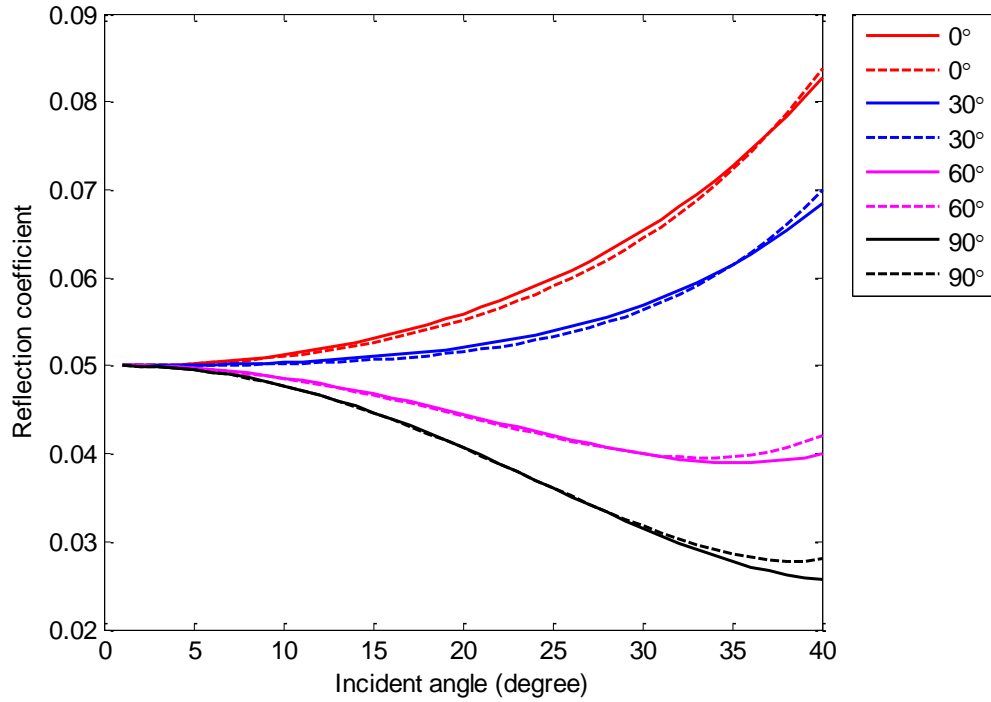


Figure 3.6. Reflection coefficients for an isotropic half-space over a HTI half-space. Dashed lines are the exact results and solid lines are the results calculated by linearized approximation for azimuths of  $0^\circ$ ,  $30^\circ$ ,  $60^\circ$ , and  $90^\circ$ . Model parameters are given in Table 3.1 (A).

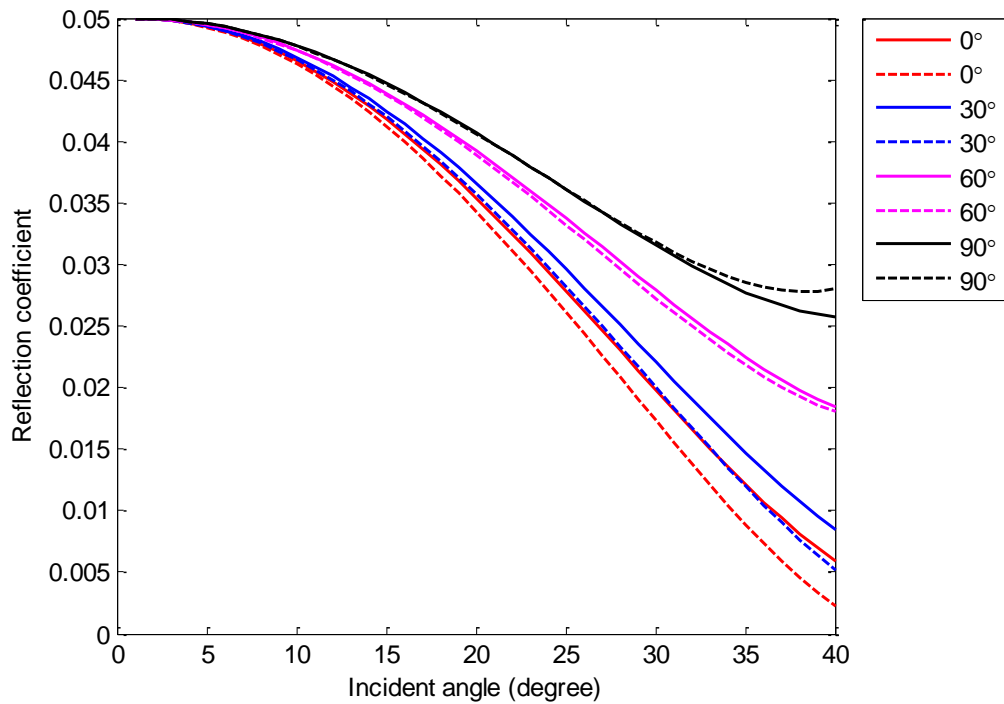


Figure 3.7. Reflection coefficients for an isotropic half-space over a HTI half-space. Dashed lines are the exact results and solid lines are the results calculated by linearized approximation for azimuths of  $0^\circ$ ,  $30^\circ$ ,  $60^\circ$ , and  $90^\circ$ . Model parameters are given in Table 3.1 (B).

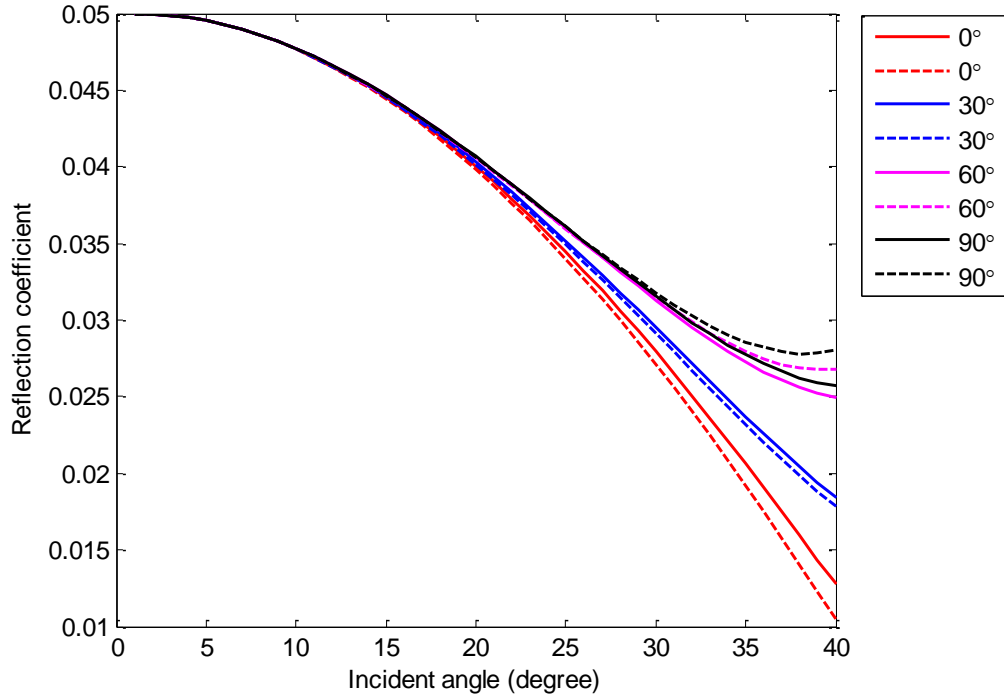


Figure 3.8. Reflection coefficients for an isotropic half-space over a HTI half-space. Dashed lines are the exact results and solid lines are the results calculated by linearized approximation for azimuths of  $0^\circ$ ,  $30^\circ$ ,  $60^\circ$ , and  $90^\circ$ . Model parameters are given in Table 3.1 (C).

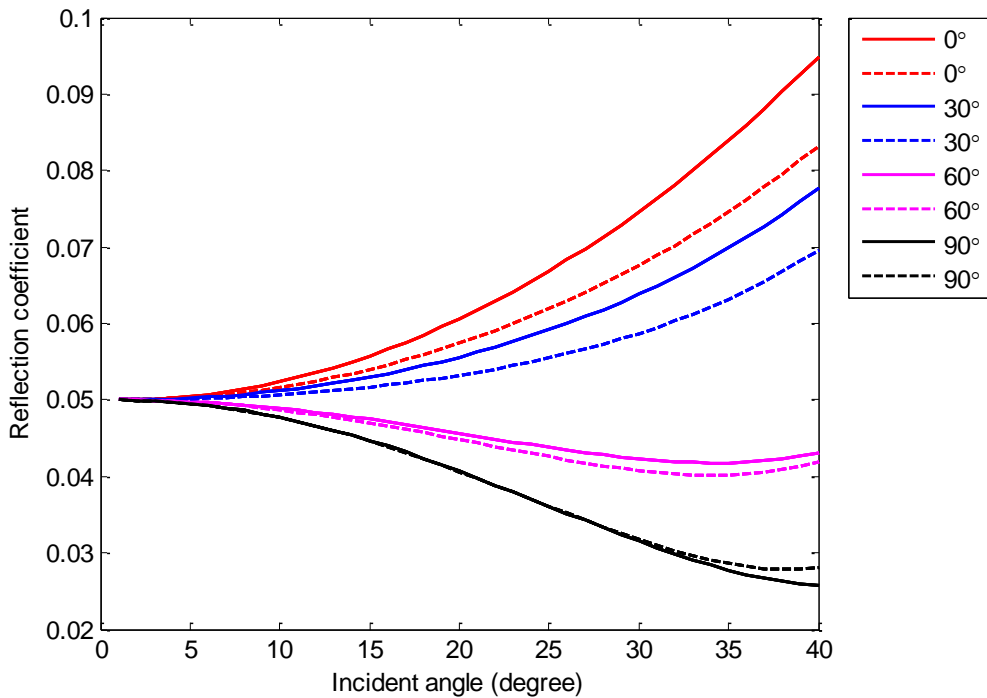


Figure 3.9. Reflection coefficients for an isotropic half-space over a HTI half-space. Dashed lines are the exact results and solid lines are the results calculated by linearized approximation for azimuths of  $0^\circ$ ,  $30^\circ$ ,  $60^\circ$ , and  $90^\circ$ . Model parameters are given in Table 3.1 (D).

The first three sets of parameters in the Table 3.1 only have one non-zero anisotropy parameter for each model. Figure 3.6, which corresponds to Model A, shows reflections from a transversely isotropic medium with a horizontal symmetry axis which has a 10% shear-wave splitting parameter. The approximations have almost the same values as the exact reflection coefficients for all azimuths but a small visible deviation for the 60° and 90° azimuths at the incident angles beyond 30°. The reflection coefficients of Model B which has a non-zero  $\delta^{(V)}$  in the reflecting medium are shown in Figure 3.7. The approximations have a good fit to the exact reflection coefficients for 60° and 90° azimuths. However, approximation of reflection coefficients for 0° and 30° underestimated the exact values especially for large incident angles. Model C shown in Figure 3.8 only has a non-zero value for  $\varepsilon^{(V)}$ . According to Rüger's approximation, the value of  $\varepsilon^{(V)}$  hardly affects the reflection coefficients and it will only make a small difference at large incident angles which matches the results in Figure 3.8. Even for the incident angle between 0° to 20°, the exact reflection coefficients for different azimuths are very similar and only split when the incident angle beyond 20°. Model D is a more realistic case which has three non-zero anisotropy parameters with shear wave splitting coefficients of 15%. The deviations between the approximations and the exact reflection coefficients as shown in Figure 3.9 are larger than the previous three models. The accuracy of the approximation increases with increasing azimuths from 0° to 90°.

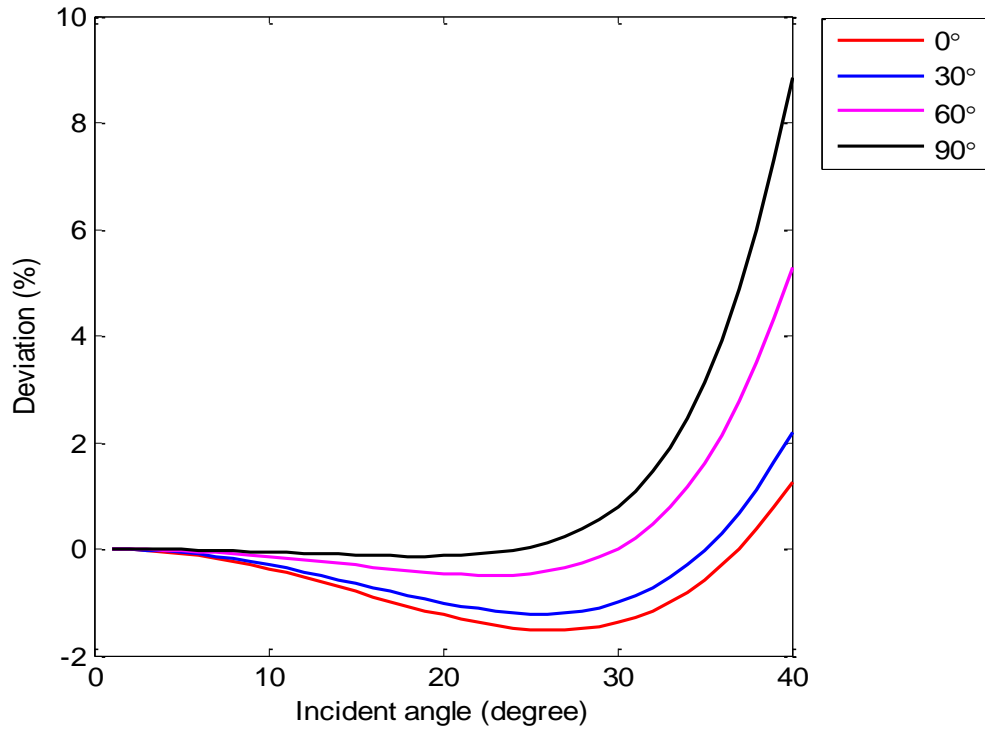


Figure 3.10. Deviation between exact P-wave reflection coefficients and approximations for Model A. The exact reflection coefficients and the linearized approximations are shown in Figure 3.6.

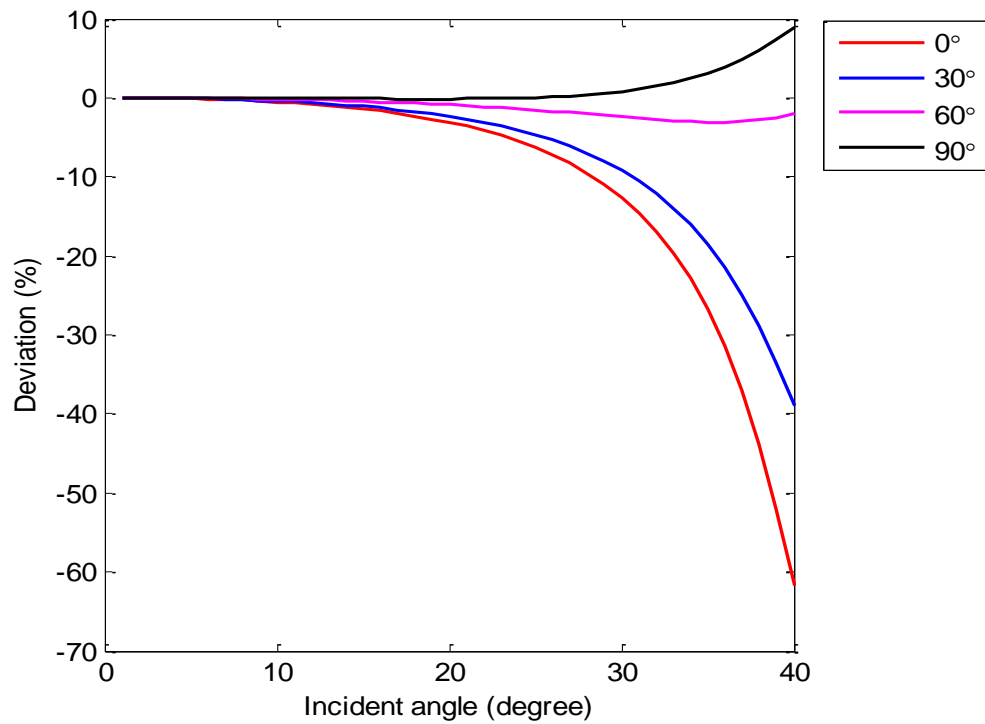


Figure 3.11. Deviation between exact P-wave reflection coefficients and approximations for Model B. The exact reflection coefficients and the linearized approximations are shown in Figure 3.7.

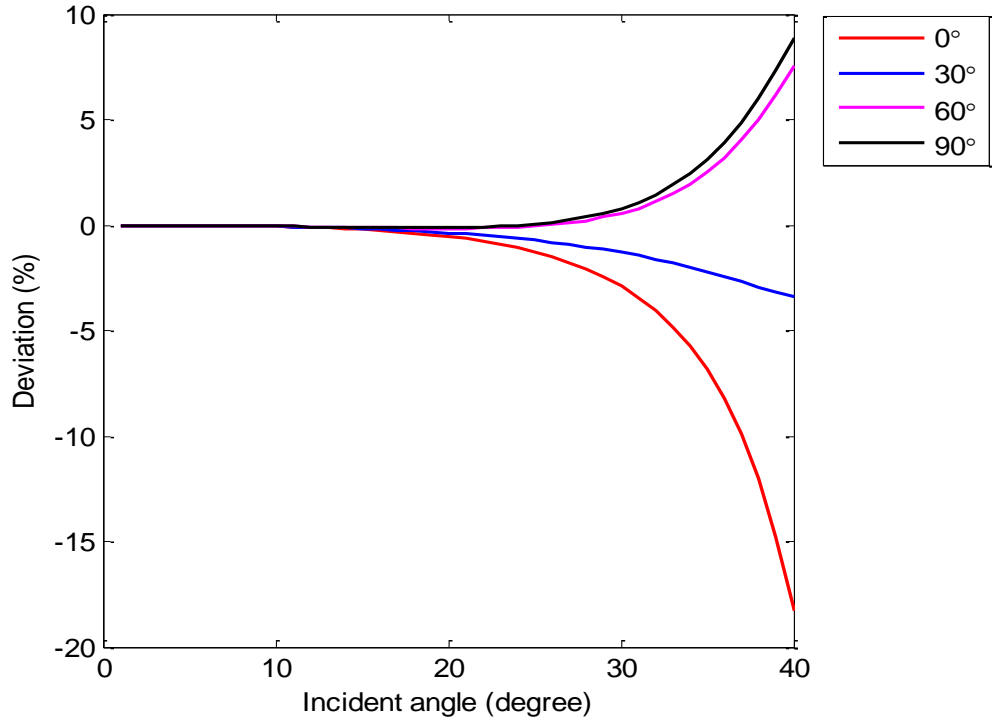


Figure 3.12. Deviation between exact P-wave reflection coefficients and approximations for Model C. The exact reflection coefficients and the linearized approximations are shown in Figure 3.8.

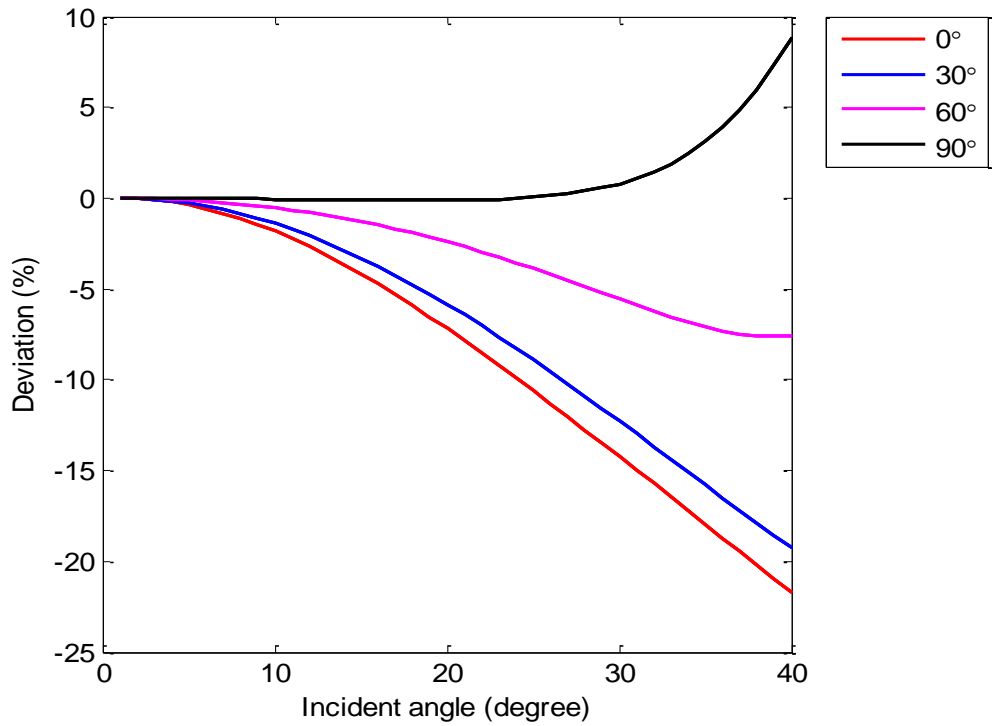


Figure 3.13. Deviation between exact P-wave reflection coefficients and approximations for Model D. The exact reflection coefficients and the linearized approximations are shown in Figure 3.9.

Figures 3.10 to 3.13 show the deviations between the exact reflection coefficients and its approximation for Models A, B, C, and D respectively. By comparing these four figures, it is obviously that non-zero value of  $\delta^{(l)}$  makes the largest difference to reflection coefficients. And except for Figure 3.10, the  $0^\circ$  azimuth, which is the vertical symmetry axis, has the lowest accuracy for the reflection coefficients. Rüger (2002) states that this phenomenon is because we use the S-wave velocity  $\beta^\perp$  in terms of  $\beta$  and  $\gamma$ . The error in the approximation of phase velocity will propagate and even increase when we use it to calculate the reflection coefficients. In order to increase the accuracy for azimuths near  $0^\circ$ , we need to replace  $\beta$  with  $\beta^\perp$  in the approximation equation.

To obtain more accurate approximations, the background and the anisotropy parameters need to be specified for specific azimuth observation (Rüger, 2002). In the isotropic plane, it is better to use the fast S-wave to calculate the reflection coefficients. And the slow S-wave is the best choice for calculating the reflection coefficients in the vertical symmetry plane.

### **3.5 Incident angle versus average angle**

Both the analytic derivation of the plane-wave Aki and Richards (1980) approximation for isotropy and its extension by Rüger (1997) for HTI, “ $i$ ” is the incident angle. However, Shuey (1985) suggests using the average angle (average of the incident and transmission angles across the boundary) for “ $i$ ” for isotropic case. The average angle yields better approximation than the incident angle. In order to study the validation of this suggestion in anisotropy, Model D in Table 3.1 is used to compare the reflection coefficients calculated by incident and average angle.

The reflection coefficients approximation obtained by incident angle and average angle are shown in Figures 3.14 to 3.17. At small azimuthal angles, which are shown in Figure 3.14 and Figure 3.15, the approximation calculated by incident angle is closer to the exact reflection coefficients compared to the approximation calculated by average angle. When the azimuthal angle increases to  $60^\circ$  which shown in Figure 3.16, the approximation obtained by average angle has better fit. However, Figure 3.17 shows that the approximation calculated by incident angle almost accurately estimate the exact reflection coefficients. Consequently, the incident angle gives better approximation at least in this model. But the value of the difference between the reflection coefficients approximation obtained by incident and average angle is very small. Thus both angles can provide an accurate result in R uger's approximation.

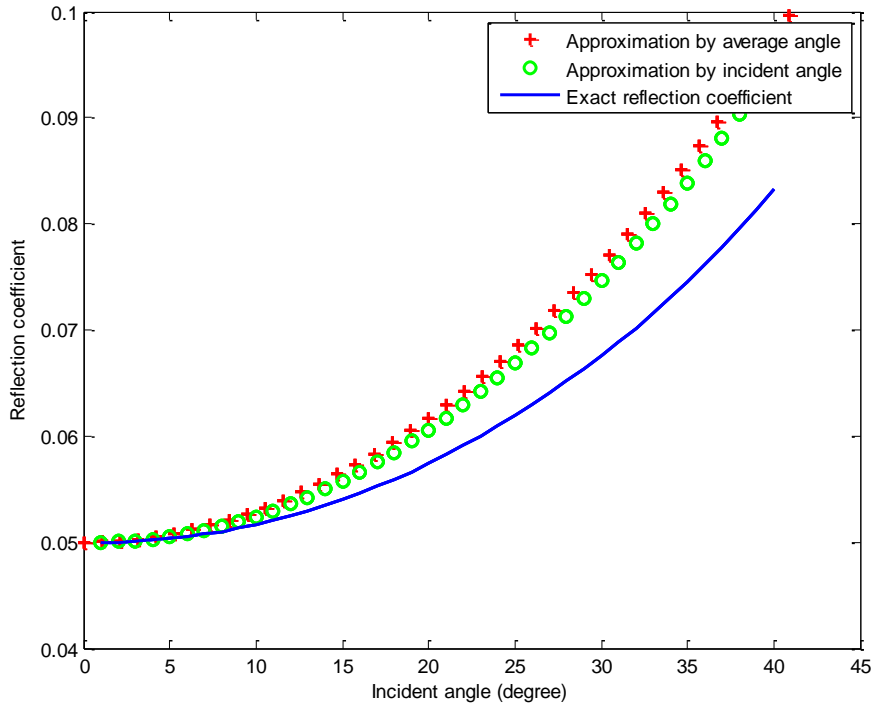


Figure 3.14. Reflection coefficients with azimuthal angle of  $0^\circ$  calculated by incident angle and average angle. Exact reflection coefficients are calculated by azimuthal angle of  $0^\circ$ .

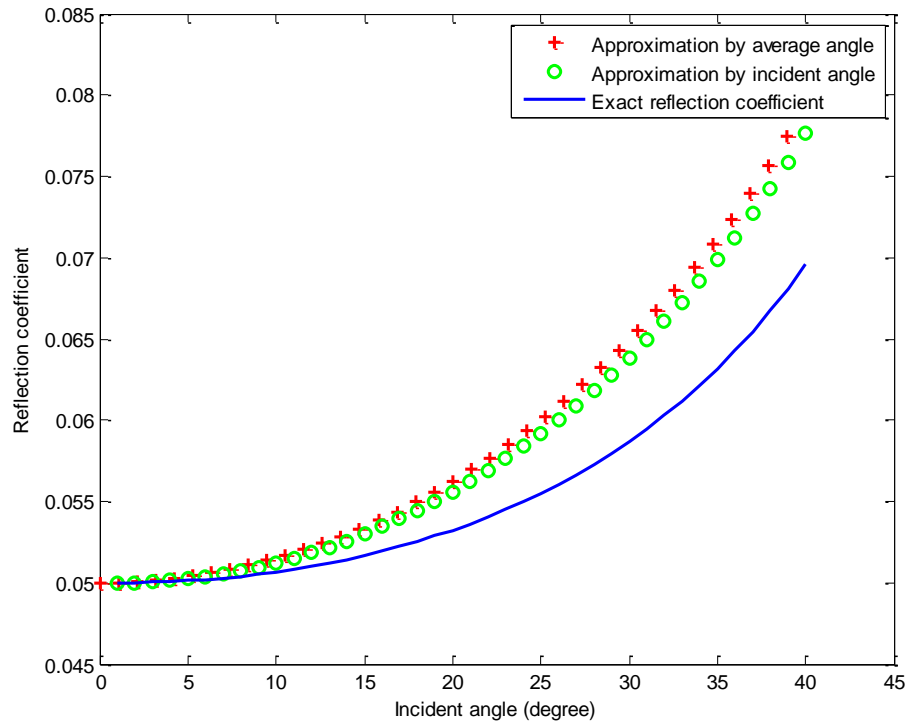


Figure 3.15. Reflection coefficients with azimuthal angle of  $30^\circ$  calculated by incident angle and average angle. Exact reflection coefficients are calculated by azimuthal angle of  $30^\circ$ .

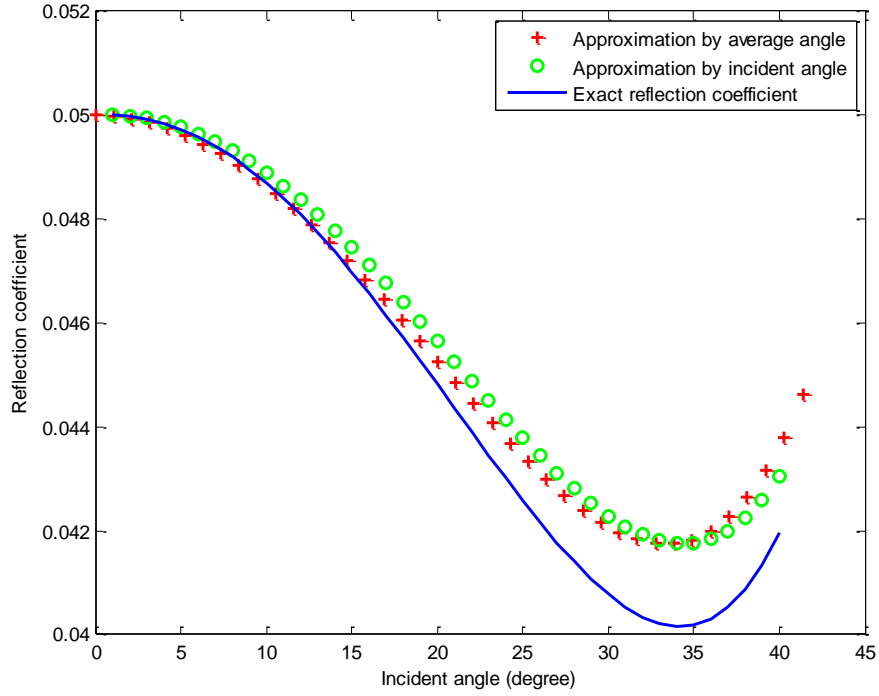


Figure 3.16. Reflection coefficients with azimuthal angle of  $60^\circ$  calculated by incident angle and average angle. Exact reflection coefficients are calculated by azimuthal angle of  $60^\circ$ .

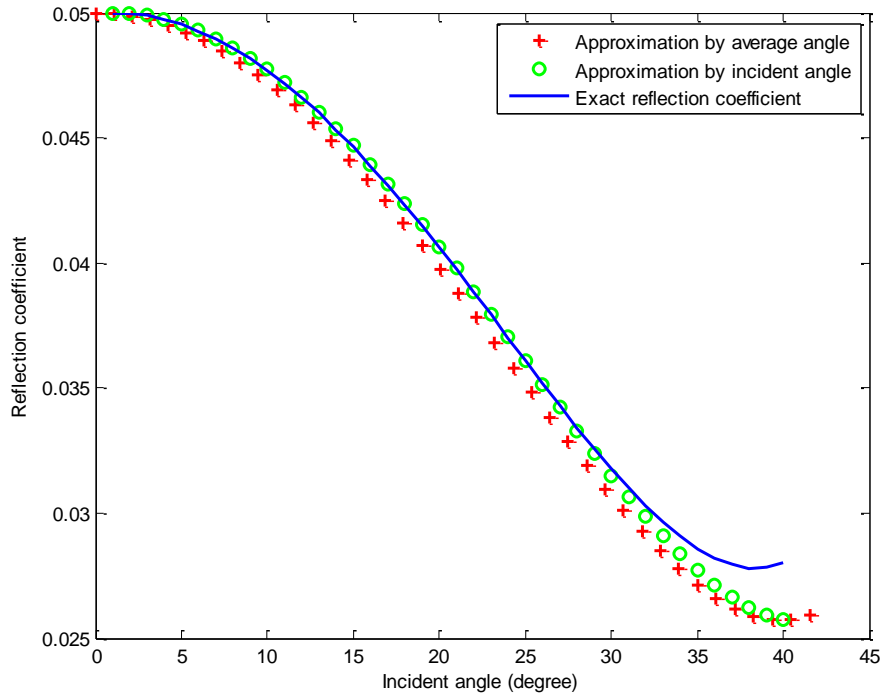


Figure 3.17. Reflection coefficients with azimuthal angle of  $90^\circ$  calculated by incident angle and average angle. Exact reflection coefficients are calculated by azimuthal angle of  $90^\circ$ .

### **3.6 Conclusion**

Chattopadhyay (2004), and Schoenberg and Protazio (1992) provide different methods to calculate the exact reflection coefficients for arbitrary anisotropic media. Knowledge for calculating phase velocity and polarization (discussed in Chapter 2) is required to calculate exact reflection coefficients. Rüger's linear approximation for reflection coefficients for HTI provides an explicit equation to obtain the reflection coefficients. And the approximation is accurate enough to estimate the exact reflection coefficients. Thus, both for forward modeling and linear inversion, Rüger's linear equation is widely used. Shuey (1985) introduces the average angle (average of the incident and transmission angles across the boundary), instead of incident angle, for the approximation in order to obtain more accurate results. However, the choice of average angle and incident angle will not affect the accuracy of the approximation.

## **CHAPTER 4**

### **EFFECTIVE MEDIUM THEORY**

#### **4.1 Introduction**

Sheriff states that fractures are planar discontinuities in rocks (Sheriff, 1991). Fractures are of interest in hydrocarbon exploration because they may significantly affect the flow characteristics of the reservoir (Schoenberg and Sayers, 1995). The flow characteristics depend on whether the fractures are open (increasing formation fluid flow) or sealed (decreasing formation fluid flow). Fracture orientation and density are two main parameters that can be recovered from seismic wave propagation to describe sets of fractures. For instance, the permeability anisotropy has the same orientation as the fracture sets and thus, the determination of the orientation of fracture sets by seismic anisotropy is of great value.

For fracture research, using borehole logs or cores are the direct and intuitive methods to study the subsurface fractures. However, there are some limitations and problems from the method itself and the sampling problem is the most important one. For example, commonly fractures in the subsurface are nearly vertical. And most boreholes are vertical which means the wellbores are parallel to the fractures. If the wellbores do not intercept the fracture sets, the information recovered from the logs might be of limited value. Because of this limitation, a more challenging method, based on seismic exploration, is required and it leads to a valuable and reliable tool for fracture characterization. In order to determine the orientation and density of fracture sets from

seismic data, assumptions are made about fracture orientation, openness, size, shape, and spatial distribution.

Numerous articles have been published that introduce different theories to specify the fracture-induced anisotropy. Most of the literature (O’Connell and Budiansky, 1974; Budiansky and O’Connell, 1976; Bruner, 1976; Hoenig, 1979; Henyey and Pomphrey, 1982; Hudson, 1980, 1981, and 1986) assumes fractures have ellipsoidal cavities with a low aspect ratio. In this chapter, I restrict my discussion to those cracks which have a size much smaller than the seismic wavelength. Based on this assumption, the low-frequency seismic response of a fractured medium can be specified as an appropriate selected homogeneous and anisotropic medium. Therefore, we can use the effective medium theory to replace the micro-heterogeneous material with a homogenous one which has the same elastic properties as the former one. Numerous papers have been published to address the issue of seismic exploration in fracture characterization. But even after substantial progresses in effective medium theory, the theory published by Hudson (1980) and Schoenberg (1980) are still widely used today.

In this chapter, I will introduce Schoenberg’s linear slip theory and compare it with Hudson’s theory. I will also discuss the situation that violates some assumptions we made in effective medium theory.

## **4.2 Crack density**

In exploration geophysics, the crack density as defined by Barton (2006) is

$$e = \frac{Na^3}{V}, \quad (4.1)$$

where  $a$  is the crack radius which is cubed because of the argument that this relates to the

energy of elastic deformation associated with the crack (O'Connell and Budiansky, 1974).  $N$  is the number of cracks in the volume  $V$ . The value for crack density ranges from 0.01 to 0.05 in most geological and tectonic situations (Leary *et al.*, 1990). Based on the definition of crack density, I am going to present three different fracture scenarios that have the same crack density: (1) ten million microcracks with 10 $\mu$ m crack radius in a 10cm cube host rock; (2) ten fractures with 1m crack radius in a 10m cube host rock; and (3) ten minor faults with 100m crack radius in a 1km cube host rock. These three different scenarios have the same value for crack density but certainly would have totally different mechanical and fluid flow properties. However, the elastic properties especially the anisotropic properties, once adjusted for scale, are supposed to be the same for the three scenarios.

### **4.3 Parallel fractures: linear slip theory**

Schoenberg (1980, 1983) treats orientated fractures as: (1) planes of weakness or (2) infinitely thin and soft layers that obey the linear-slip boundary conditions regardless of the shape and microstructure of the fractures. These two representations limit this effective medium theory to low-frequency seismic exploration which has a long wavelength compared to the size and spacing of the fracture sets. According to Schoenberg's theory, the seismic response of the wave propagating through the fractured medium can be determined by the elastic modulus and density, and the presence of fracture sets can be recovered from the elastic modulus of the equivalent medium. The fractured rock density is considered to be the same as the unfractured host rock because of the assumption that the fracture volume is infinitesimal compared to the entire volume.

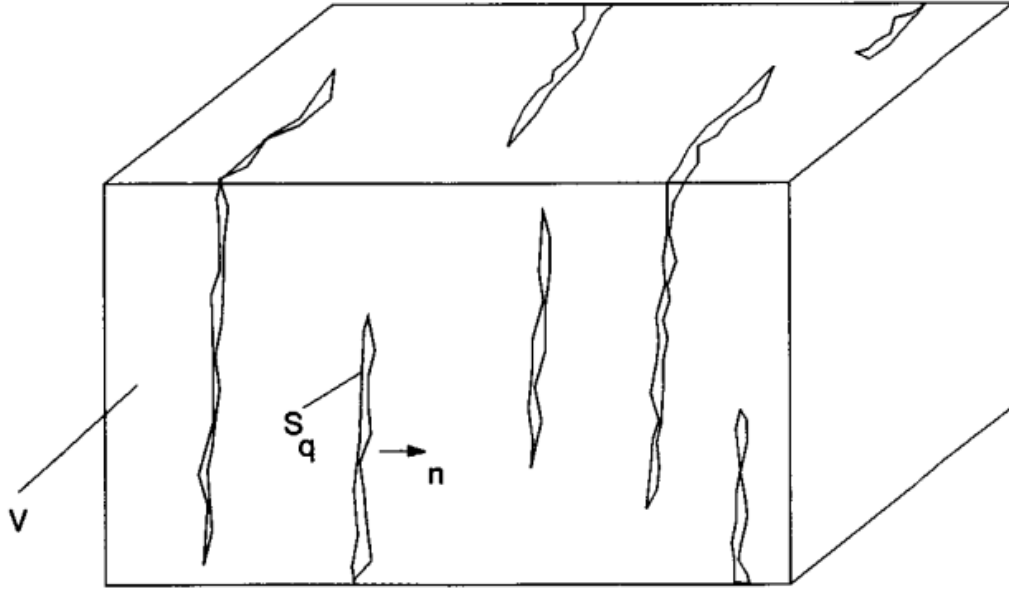


Figure 4.1. Diagrammatic view of a vertically fractured medium (Schoenberg and Sayers, 1995).

In an unfractured host rock, the relationship between strain ( $\varepsilon_{ij}$ ) and stress ( $\sigma_{kl}$ ) can be expressed by the elastic compliance tensor ( $S_{ijkl}$ ) as

$$\varepsilon_{ij} = S_{ijkl} \sigma_{kl} \quad (4.2)$$

When the medium has fracture sets, we can write the strain over a representative volume  $V$  as

$$\varepsilon_{ij} = S_{ijklb} \sigma_{kl} + \frac{1}{2V} \sum_q \int_{s_q} ([u_i] n_j + [u_j] n_i) ds \quad , \quad (4.3)$$

where  $S_{ijklb}$  is the compliance tensor, where  $b$  denotes the unfractured host rock, which can have arbitrary anisotropy.  $s_q$  is the surface of the  $q$ -th fracture located within the medium (See Figure 4.1).  $n_i$  is the component of the unit normal to the fracture surface. The brackets  $[ ]$  in the formula denotes the discontinuous jump in displacement. Here we

make the assumption that the interaction between fractures can be ignored or there is no interaction so that the displacement can be specified in stress.

When there are more than one fracture set in the host rock, which is a common situation for naturally occurring fractures, orientation of different fractures can be used as a standard to divide them into different sets. Figure 4.2 is an example of joint traces in two different directions which are exposed on a horizontal limestone unit of the Pennsylvanian-Permian Rico Formation.

According to the boundary conditions of linear slip theory, the jump in displacement vector  $[u]$  across a plane of weakness can be expressed by stress, “fracture system compliance tensor”, and unit normal as

$$\frac{1}{V} \sum_q \int_{s_q} [u_i] ds \equiv Z_{ij} \sigma_{jk} n_k , \quad (4.4)$$

Where  $Z_{ij}$  is defined as the symmetric and non-negative compliance tensor which is similar to the crack compliance tensor used by Kachanov (1992). The extra strain in equation (4.3) can be written in the same form as the strain for the host rock

$$\varepsilon_{ij} = S_{ijklf} \sigma_{kl} . \quad (4.5)$$

By substituting equation (4.4) into equation (4.3), the extra strain yields

$$\begin{aligned} S_{ijklf} \sigma_{kl} &= \frac{1}{2} (Z_{ir} \sigma_{rs} n_s n_j + Z_{jr} \sigma_{rs} n_s n_i) \\ &= \frac{1}{2} (Z_{ir} n_s n_j + Z_{jr} n_s n_i) \frac{\delta_{rk} \delta_{sl} + \delta_{rl} \delta_{sk}}{2} \sigma_{kl} . \end{aligned} \quad (4.6)$$

And, we can obtain the expression for  $S_{ijklf}$

$$S_{ijklf} = \frac{1}{4} (Z_{ik} n_l n_j + Z_{jk} n_l n_i + Z_{il} n_k n_j + Z_{jl} n_k n_i) . \quad (4.7)$$

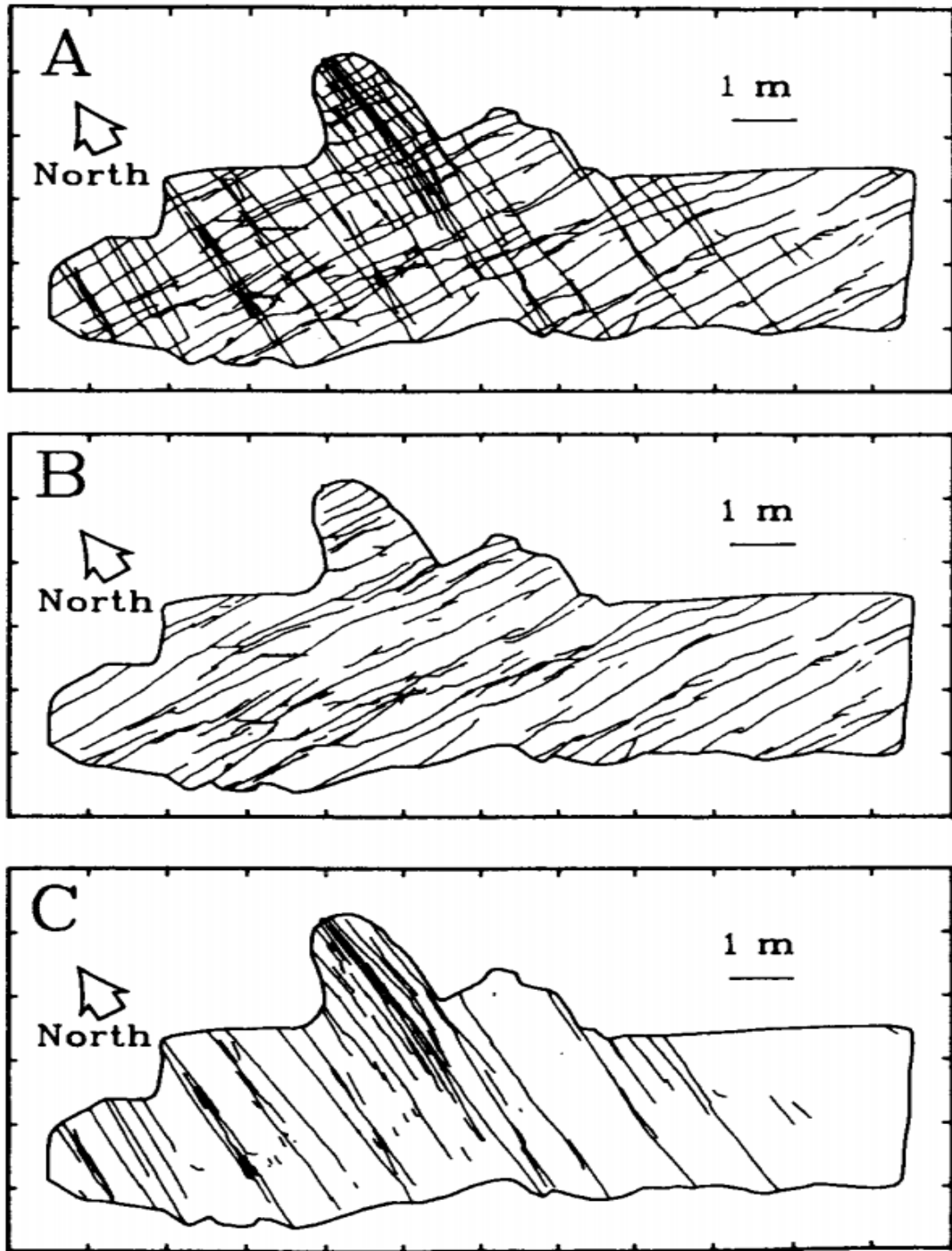


Figure 4.2. Maps of joint traces in two directions on bedding surface of Rico Formation, Monument upwarp, southeastern Utah (Schoenberg and Sayers, 1995).  
*Note:* (a) Both joint sets. (b) East-West set. (c) North-South set.

We apply this excess compliance tensor to equation (4.3). For more than one set of aligned fractures, the unit normal, fracture system compliance tensor, and excess compliance tensor of each set can be expressed as  $n_j^{(m)}$ ,  $Z_{ij}^{(m)}$ , and  $S_{ijkl}^{(m)}$ . The compliance of the medium with multiple sets of aligned fracture is

$$\begin{aligned} S_{ijkl} &= S_{ijklb} + S_{ijklf}^{(m)} \\ &= S_{ijklb} + \frac{1}{4} \sum_m (Z_{ik}^{(m)} n_l^{(m)} n_j^{(m)} + Z_{jk}^{(m)} n_l^{(m)} n_i^{(m)} + Z_{il}^{(m)} n_k^{(m)} n_j^{(m)} + Z_{jl}^{(m)} n_k^{(m)} n_i^{(m)}) \end{aligned} \quad (4.8)$$

Note that even if the host rock is isotropic, sets of aligned fractures in arbitrary orientation can result in a triclinic medium as the effective medium. In order to calculate the phase velocity, group velocity, and the reflection coefficient for waves propagating in the fractured medium, we have to obtain the stiffness tensor of the effective medium by simply inverting the compliance tensor.

For rotationally invariant fracture sets, we let the normal compliance of the fractures be given by  $Z_N$  and the tangential compliance by  $Z_T$ . The behavior of the rotationally invariant fracture is going to be invariant with respect to rotation about the axis normal to the fracture so that we can write the compliance as

$$\begin{aligned} Z_{ij} &= Z_N n_i n_j + Z_T (\delta_{ij} - n_i n_j) \\ &= Z_T \delta_{ij} + (Z_N - Z_T) n_i n_j \end{aligned} \quad (4.9)$$

For a single rotationally invariant fracture set, we substitute the compliance in equation (4.9) into equation (4.7)

$$S_{ijklf} = \frac{Z_T}{4} (\delta_{ik} n_l n_j + \delta_{jk} n_l n_i + \delta_{il} n_k n_j + \delta_{jl} n_k n_i) + (Z_N - Z_T) n_i n_j n_k n_l. \quad (4.10)$$

As an example, we take a single set of rotationally invariant vertical fracture which has a

unit normal as  $(1, 0, 0)$ . The fracture set is parallel to the  $x_2$ -axis and its normal is parallel to the  $x_1$ - axis. For this case

$$S_{1111f} = Z_N,$$

$$S_{1212f} = S_{2121f} = S_{1221f} = S_{2112f} = S_{1313f} = S_{3131f} = S_{1331f} = S_{3113f} = \frac{Z_T}{4}. \quad (4.11)$$

The other compliance components, which are not mentioned in the above equation, are equal to zero. In order to write the compliance in a compact form, we follow the method published by Nye (1957). In the condensed compliance matrix, we have the following relationship

$$\begin{aligned} 11 &\rightarrow 1, \\ 22 &\rightarrow 2, \\ 33 &\rightarrow 3, \\ 23 &\rightarrow 4, \\ 13 &\rightarrow 5, \\ 12 &\rightarrow 6. \end{aligned}$$

Because of the symmetry property of compliance tensor, factors 2 and 4 are

$$\begin{aligned} S_{ijkl} &\rightarrow S_{pq} \text{ when both } p, q \text{ are } 1, 2, \text{ or } 3; \\ 2 S_{ijkl} &\rightarrow S_{pq} \text{ when one of } p, q \text{ are } 4, 5, \text{ or } 6; \\ 4 S_{ijkl} &\rightarrow S_{pq} \text{ when both } p, q \text{ are } 4, 5, \text{ or } 6. \end{aligned}$$

Then we write equation (4.11) in a condensed 6x6 matrix form as

$$\begin{bmatrix} Z_N & 0 & 0 & 0 & 0 & 0 \\ 0 & 0 & 0 & 0 & 0 & 0 \\ 0 & 0 & 0 & 0 & 0 & 0 \\ 0 & 0 & 0 & 0 & 0 & 0 \\ 0 & 0 & 0 & 0 & Z_T & 0 \\ 0 & 0 & 0 & 0 & 0 & Z_T \end{bmatrix}. \quad (4.12)$$

Considering a single set of aligned rotationally invariant fractures embedded in an isotropic host rock, the effective medium of the fractured rock becomes transversely isotropic with its symmetry axis perpendicular to the set of fractures. But this TI medium is little different from general TI medium due to it is only controlled by two elastic modulus of the host rock, say Lamé parameters  $\mu_b$  and  $\lambda_b$ , and two non-negative fracture compliance  $Z_N$  and  $Z_T$ . And we called such TI medium as TI (LSD). We can write the compliance of TI (LSD) as

$$S = \begin{bmatrix} \frac{\lambda_b + \mu_b}{\mu_b(3\lambda_b + 2\mu_b)} + Z_N & -\frac{\lambda_b}{2\mu_b(3\lambda_b + 2\mu_b)} & -\frac{\lambda_b}{2\mu_b(3\lambda_b + 2\mu_b)} & 0 & 0 & 0 \\ -\frac{\lambda_b}{2\mu_b(3\lambda_b + 2\mu_b)} & \frac{\lambda_b + \mu_b}{\mu_b(3\lambda_b + 2\mu_b)} & -\frac{\lambda_b}{2\mu_b(3\lambda_b + 2\mu_b)} & 0 & 0 & 0 \\ -\frac{\lambda_b}{2\mu_b(3\lambda_b + 2\mu_b)} & -\frac{\lambda_b}{2\mu_b(3\lambda_b + 2\mu_b)} & \frac{\lambda_b + \mu_b}{\mu_b(3\lambda_b + 2\mu_b)} & 0 & 0 & 0 \\ 0 & 0 & 0 & \frac{1}{\mu_b} & 0 & 0 \\ 0 & 0 & 0 & 0 & \frac{1}{\mu_b} + Z_T & 0 \\ 0 & 0 & 0 & 0 & 0 & \frac{1}{\mu_b} + Z_T \end{bmatrix}. \quad (4.13)$$

Since  $Z_N$  and  $Z_T$  are assumed to be positive, there are some constraints we can find in the compliance matrix of TI (LSD) medium,

$$\begin{aligned}
S_{44} &\leq S_{55}, \\
-2S_{33} &< -2S_{13} < S_{33} \leq S_{11}, \\
S_{13} &\equiv S_{23} \equiv S_{33} - \frac{S_{44}}{2}.
\end{aligned} \tag{4.14}$$

Any transversely isotropic media satisfying the constraints in equation (4.14) can be defined as TI (LSD) medium (Schoenberg and Sayers, 1995). With a full knowledge of the TI (LSD) compliance, the parameters of the host rock and fracture compliance are possible to be recovered (Hsu and Schoenberg, 1993).

In order to obtain the stiffness matrix of the effective medium, we invert the compliance matrix as

$$c = \begin{bmatrix} M_b(1-\Delta N) & \lambda_b(1-\Delta N) & \lambda_b(1-\Delta N) & 0 & 0 & 0 \\ \lambda_b(1-\Delta N) & M_b(1-r_b^2\Delta N) & \lambda_b(1-r_b\Delta N) & 0 & 0 & 0 \\ \lambda_b(1-\Delta N) & \lambda_b(1-r_b\Delta N) & M_b(1-r_b^2\Delta N) & 0 & 0 & 0 \\ 0 & 0 & 0 & \mu_b & 0 & 0 \\ 0 & 0 & 0 & 0 & \mu_b(1-\Delta T) & 0 \\ 0 & 0 & 0 & 0 & 0 & \mu_b(1-\Delta T) \end{bmatrix}, \tag{4.15}$$

where

$$\begin{aligned}
M_b &= \lambda_b + 2\mu_b, \\
r_b &= \frac{\lambda_b}{M_b}.
\end{aligned}$$

$\Delta N$  and  $\Delta T$ , called normal and tangential weaknesses (Bakulin and Molotkov, 1997), are dimensionless quantities introduced by Hsu and Schoenberg (1993). They can be written in terms of  $Z_N$  and  $Z_T$  as

$$\begin{aligned}
\Delta N &= \frac{(\lambda_b + 2\mu_b) K_N}{1 + (\lambda_b + 2\mu_b) K_N}, \\
\Delta T &= \frac{\mu_b K_T}{1 + \mu_b K_T}.
\end{aligned} \tag{4.16}$$

Both of these two weaknesses are from 0 to 1 according to the mathematical definition. And we can also find some constraints in the stiffness matrix which are similar to equation (4.14),

$$\begin{aligned}
c_{55} &\leq c_{44}, \\
-\frac{c_{11}}{2} &< c_{13} < c_{11} \leq c_{33}, \\
c_{11}c_{33} - c_{13}^2 &= 2c_{44}(c_{11} + c_{13}).
\end{aligned} \tag{4.17}$$

By simply inverting equation (4.13) and substituting the fracture compliance  $Z_N$  and  $Z_T$  with  $\Delta N$  and  $\Delta T$ , we can write the stiffness matrix of the fracture as

$$c_f = \begin{pmatrix} (\lambda_b + 2\mu_b)\Delta N & \lambda_b\Delta N & \lambda_b\Delta N & 0 & 0 & 0 \\ \lambda_b\Delta N & \frac{\lambda_b^2}{\lambda_b + 2\mu_b}\Delta N & \frac{\lambda_b^2}{\lambda_b + 2\mu_b}\Delta N & 0 & 0 & 0 \\ \lambda_b\Delta N & \frac{\lambda_b^2}{\lambda_b + 2\mu_b}\Delta N & \frac{\lambda_b^2}{\lambda_b + 2\mu_b}\Delta N & 0 & 0 & 0 \\ 0 & 0 & 0 & 0 & 0 & 0 \\ 0 & 0 & 0 & 0 & \mu_b\Delta T & 0 \\ 0 & 0 & 0 & 0 & 0 & \mu_b\Delta T \end{pmatrix}. \tag{4.18}$$

When a S-wave is propagating in the isotropic plane of the effective medium, it propagates with two different velocities depending on its polarization. The fast S-wave velocity which has a polarization parallel to the isotropic plane is controlled by  $c_{44}$ . The slower S-wave velocity which has a polarization perpendicular to the isotropic plane is controlled by  $c_{55}$ . So the difference of the two S-wave velocities can be written as

$$V_{s-fast} - V_{s-slow} = \sqrt{c_{44} / \rho_b} - \sqrt{c_{55} / \rho_b} = \sqrt{\mu_b / \rho_b} (1 - \sqrt{1 - \Delta T}) . \tag{4.19}$$

#### 4.4 Aligned penny-shaped crack

One of the simplest fracture rock models is an isotropic host rock with a set of

aligned penny-shaped cracks which have the similar form of oblate spheroids. The aspect ratio  $\alpha \equiv c/a$  for penny-shaped crack ( $a$  denotes the semi-major axis of the spheroid and  $c$  denotes the semi-minor axis) is much smaller than unity because the thickness of the crack is very small. Thomsen (1988) suggests that the crack density of isolated penny-shaped cracks is valid when the crack density is smaller than 0.05.

Hudson (1980, 1981) introduces a first-term expression for excess stiffness caused by thin isolated penny-shaped cracks as

$$c_f = \begin{pmatrix} \frac{e(\lambda+2\mu)^2}{\mu} U_{11} & \frac{e\lambda(\lambda+2\mu)}{\mu} U_{11} & \frac{e\lambda(\lambda+2\mu)}{\mu} U_{11} & 0 & 0 & 0 \\ \frac{e\lambda(\lambda+2\mu)}{\mu} U_{11} & \frac{e\lambda^2}{\mu} U_{11} & \frac{e\lambda^2}{\mu} U_{11} & 0 & 0 & 0 \\ \frac{e\lambda(\lambda+2\mu)}{\mu} U_{11} & \frac{e\lambda^2}{\mu} U_{11} & \frac{e\lambda^2}{\mu} U_{11} & 0 & 0 & 0 \\ 0 & 0 & 0 & 0 & 0 & 0 \\ 0 & 0 & 0 & 0 & e\mu U_{33} & 0 \\ 0 & 0 & 0 & 0 & 0 & e\mu U_{33} \end{pmatrix}, \quad (4.20)$$

where  $U_{11}$  and  $U_{33}$  are dimensionless quantities. This method simulates high-frequency behavior which is appropriate to ultrasonic experiments in laboratory. Because the wave-induced pore-pressure increment to flow equilibrates in the low-frequency case, it is suggested to use Brown and Korringa low-frequency relations to saturate the dry cracks with fluid in order to use Hudson's method to calculate the effective stiffness of fluid-filled cracks embedded in a host rock. Several assumptions are required before using this method. They are

- Cracks inside the host rock are idealized penny-shaped cracks with very small aspect ratios and small crack density. And the crack radius and the distance between cracks are assumed to be much smaller than a wavelength.
- Cracks are isolated which means no fluid will flow from one crack to another. The interaction between cracks is not considered in this method.

Comparing equation (4.18) to equation (4.20), both equations of the stiffness matrix, calculated by Schoenberg's method and Hudson's method, give exactly the same form of the excess stiffness caused by a set of vertical aligned fractures if the fracture weaknesses satisfy the following relations

$$\begin{aligned}\Delta N &= \frac{(\lambda + 2\mu)}{\mu} U_{11} e, \\ \Delta T &= U_{33} e.\end{aligned}\tag{4.21}$$

The results of  $U_{11}$  and  $U_{33}$  can be written in terms of  $\Delta N$  and  $\Delta T$  for fractures which are filled with a weak solid with bulk modulus  $k'$  and shear modulus  $\mu'$  by substituting the expressions for  $U_{11}$  and  $U_{33}$  given by Hudson (1981) into equation (4.21),

$$\begin{aligned}\Delta N &= \frac{4e}{3g(1-g)\left[1 + \frac{\alpha}{\pi g(1-g)} \left(\frac{k' + 4/3\mu'}{\mu_b}\right)\right]}, \\ \Delta T &= \frac{16e}{3(3-2g)\left[1 + \frac{4\alpha}{\pi(3-2g)} \left(\frac{\mu'}{\mu_b}\right)\right]},\end{aligned}\tag{4.22}$$

where

$$g \equiv \frac{\mu_b}{\lambda_b + 2\mu_b},$$

and  $\alpha$  is the aspect ratio of cracks.  $V_P$  and  $V_S$  are P-wave and S-wave velocities in the isotropic host rock.

Isolated penny-shaped dry cracks that are embedded in an isotropic host rock are a special case which has simpler expressions for  $\Delta N$  and  $\Delta T$  as shown in equation (4.22). For dry cracks, both the bulk and shear modulus of the infill material are close to zero, so we have

$$\begin{aligned}\Delta N &= \frac{4e}{3g(1-g)}, \\ \Delta T &= \frac{16e}{3(3-2g)}.\end{aligned}\tag{4.23}$$

The effective medium for an isotropic host rock with a set of vertical isolated penny-shaped dry cracks equals a special transversely isotropic medium with a horizontal axis (HTI). And we can use two elastic constants and three anisotropy parameters to specify a HTI medium according to Chapter 2. Thus, we write the anisotropic parameters ( $\delta^{(V)}$ ,  $\varepsilon^{(V)}$ ,  $\gamma^{(V)}$ ) which are introduced by Rüger (1997) in terms of the crack density  $e$  and the squared  $V_S/V_P$  ratio ( $g$ ) of the host rock as

$$\begin{aligned}\delta^{(V)} &= -\frac{8}{3}e\left[1 + \frac{g(1-2g)}{(3-2g)(1-g)}\right], \\ \varepsilon^{(V)} &= -\frac{8}{3}e, \\ \gamma^{(V)} &= -\frac{8e}{3(3-2g)}.\end{aligned}\tag{4.24}$$

Note that expressions in equation (4.24) are linear approximations. If we make an assumption that  $V_S/V_P$  ratio is between 0.35 and 0.65, which is common for most cases, the range of three anisotropic parameters can be obtained according to equation (4.24) as

$$\begin{aligned}\delta^{(V)} &= (-2.82 \pm 0.05)e , \\ \varepsilon^{(V)} &= -2.68e , \\ \gamma^{(V)} &= (-1.10 \pm 0.13)e .\end{aligned}\tag{4.25}$$

The exciting evidence we can find in equation (4.25) is that the absolute value of  $\gamma^{(V)}$  is very close to the crack density  $e$  (Thomsen, 1995). This means the time delay in S-wave splitting at vertical incidence is a direct indication of the crack density. And in the next chapter, inversions based on this discover are applied to invert for crack density in an isotropic host rock with a set of vertical aligned dry cracks.

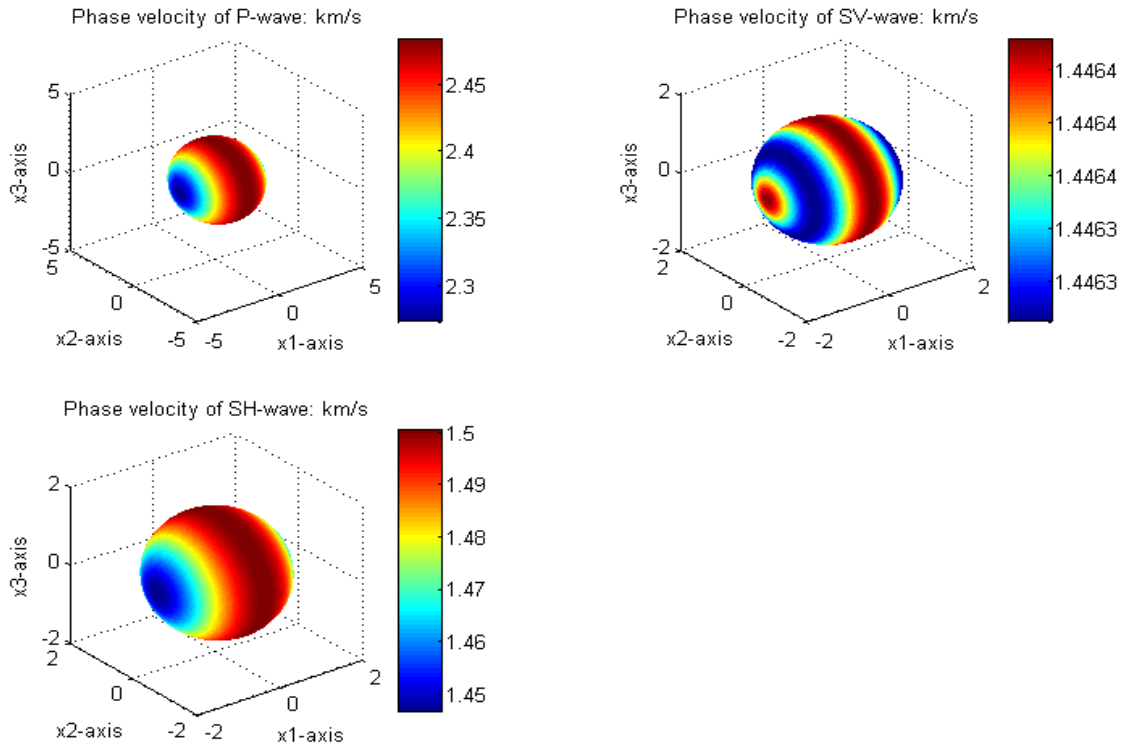


Figure 4.3. Phase velocities of P-wave, SV-wave, and SH-wave of a fractured medium, with P-wave velocity in the isotropic host rock equals to 2.5 km/s; S-wave velocity in the isotropic host rock, 1.5 km/s; density,  $2.7 \text{ g/cm}^3$ ; and, crack density, 0.03.

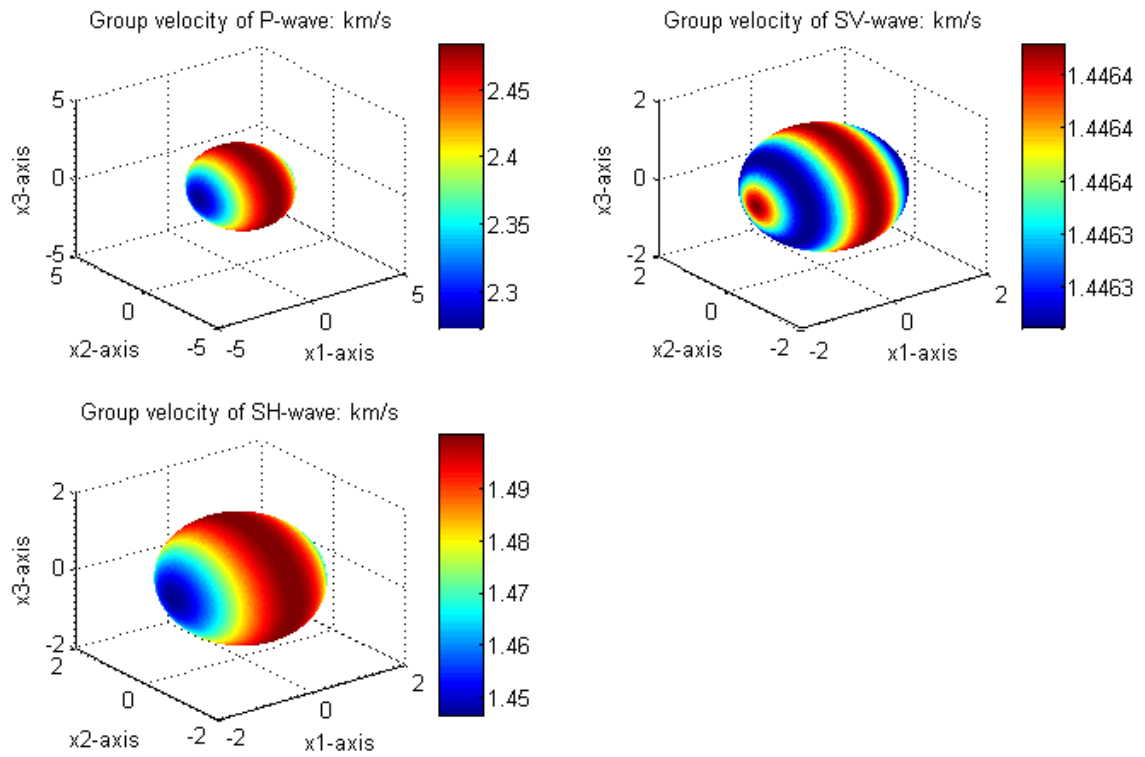


Figure 4.4. Group velocities of P-wave, SV-wave, and SH-wave of a fractured medium, with P-wave velocity in the isotropic host rock equals to 2.5 km/s; S-wave velocity in the isotropic host rock, 1.5 km/s; density,  $2.7 \text{ g/cm}^3$ , and, crack density, 0.03.

A numerical test is shown in Figure 4.3 (phase velocity) and Figure 4.4 (group velocity) for a set of vertical aligned dry cracks embedded in the isotropic rock, where P-wave velocity in the isotropic host rock is 2.5 km/s, S-wave velocity in the isotropic rock is 1.5 km/s, density is 2.7 g/cm<sup>3</sup>, and crack density is 0.03. The difference between phase velocity and group velocity is only in magnitude. However, the phase velocity will have different values for different crack densities. Figure 4.5 and Figure 4.6 show the change in P-wave velocity in the vertical symmetry plane and isotropic plane for different crack densities. In both figures, higher values of crack density have more variation in the P-wave phase velocity. An interesting phenomenon happens in Figure 4.7 where the SV-wave velocity is illustrated. When the crack density is 0.01, the SV-wave phase velocity is concave up while the velocity for a crack density 0.05 is concave down. Schoenberg and Sayers (1995) note that this phenomenon is caused by the sign of anellipticity and it can be expressed as

$$\frac{4\mu_b^2(M_b - \mu_b)}{(1 + Z_T \mu_b)(1 + Z_N M_b)} (Z_T - Z_N) . \quad (4.26)$$

If  $Z_T < Z_N$  the positive anellipticity will happen just like the red line of crack density 0.01 in Figure 4.7, and this is a usual geological situation. If  $Z_T = Z_N$ , the anellipticity will vanish and the medium simulates an elliptical medium, as shown by the black line for the crack density 0.03 in Figure 4.7. The SV-wave velocity in symmetry plane is almost a constant value. If  $Z_T > Z_N$ , the velocity will look like the blue line of density 0.05 in Figure 4.7, which has negative anellipticity. Another interesting point occurs in Figure 4.9 and Figure 4.10 where the SH-wave velocity is illustrated. In the isotropic plane, the SH-wave velocity does not change, no matter what crack density is given. The reason for the

constant velocity in the isotropic plane is that the SH-wave velocity in that plane is controlled by  $c_{44}$  of the effective stiffness matrix, and  $c_{44}$  is not affected by the crack density, as it is only dependent on the shear module  $\mu_b$  of the host matrix according to equation (4.15). This phenomenon is obvious in Figure 4.10 and also in Figure 4.9 when the incident angle equals 0. As mentioned before, the TI (LSD) has a special property that it is only controlled by four independent parameters, which is one less than general TI model.

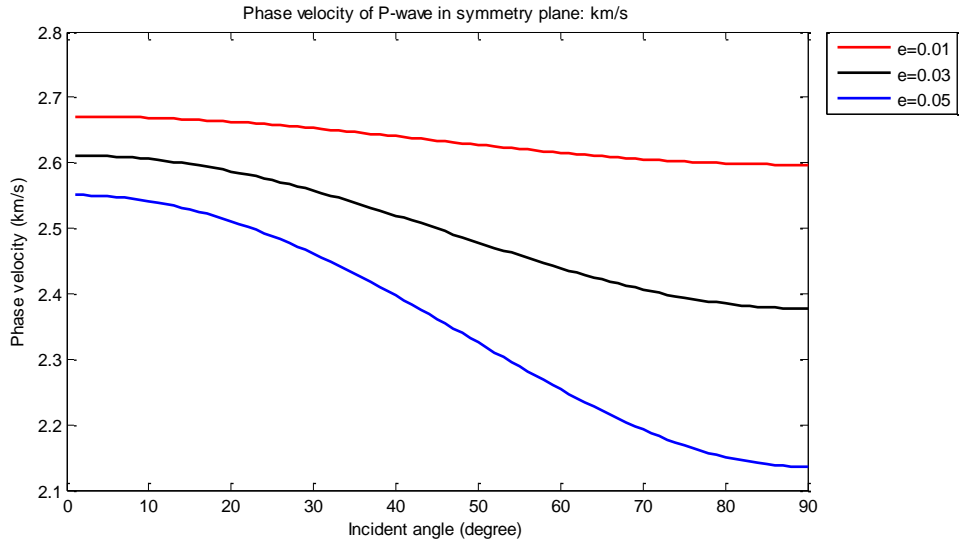


Figure 4.5. Phase velocity of P-wave in the vertical symmetry plane. Model parameters are the same as Figure 4.3 except for crack density.

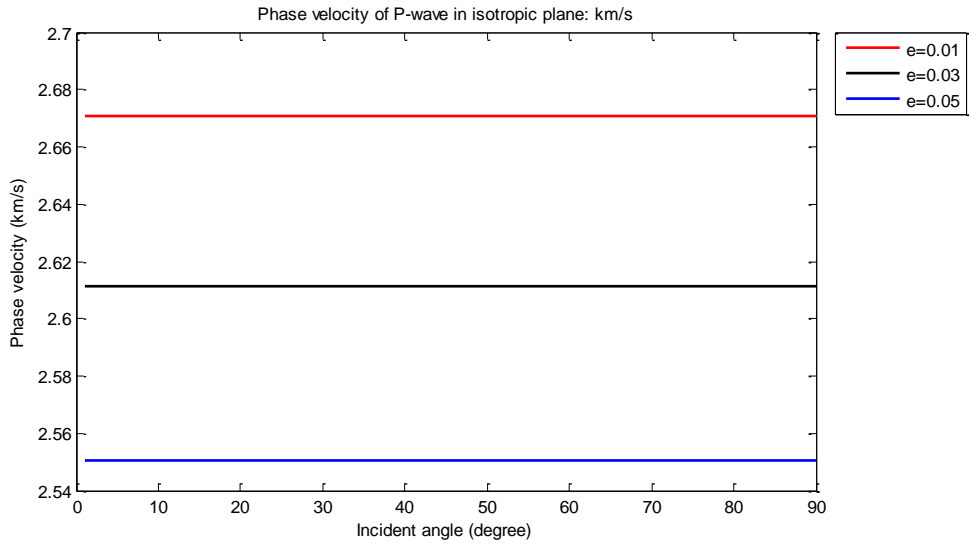


Figure 4.6. Phase velocity of P-wave in the isotropic plane. Model parameters are the same as Figure 4.3 except for crack density.

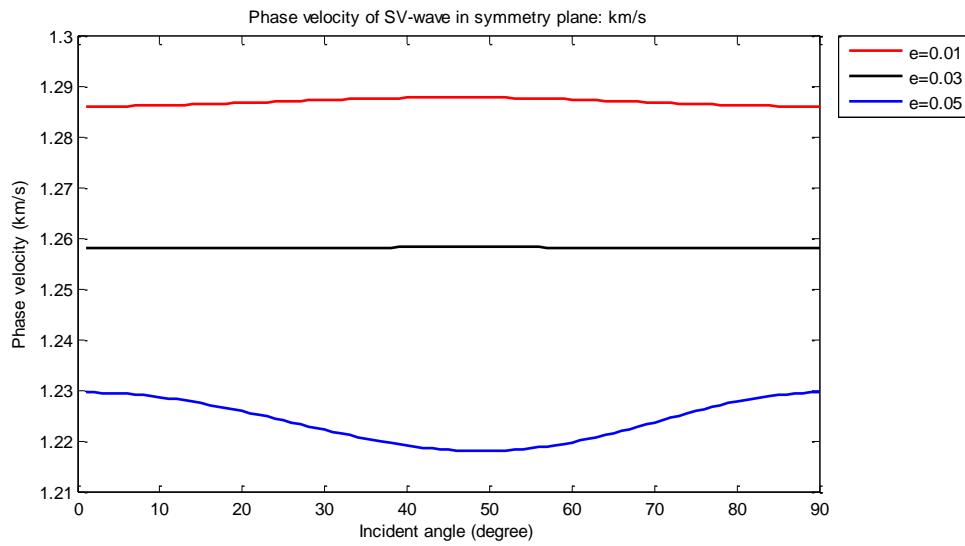


Figure 4.7. Phase velocity of SV-wave in the vertical symmetry plane. Model parameters are the same as Figure 4.3 except for crack density.

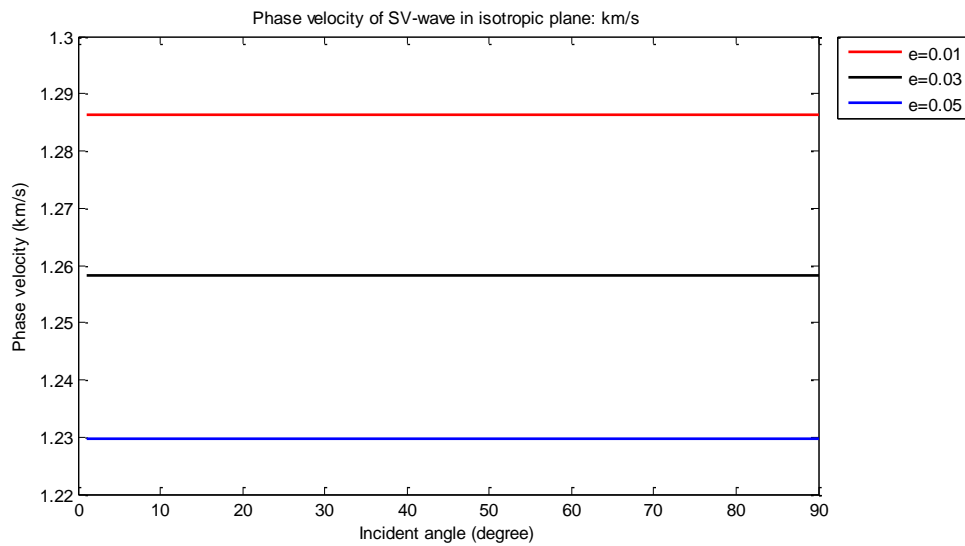


Figure 4.8. Phase velocity of SV-wave in the isotropic plane. Model parameters are the same as Figure 4.3 except for crack density.

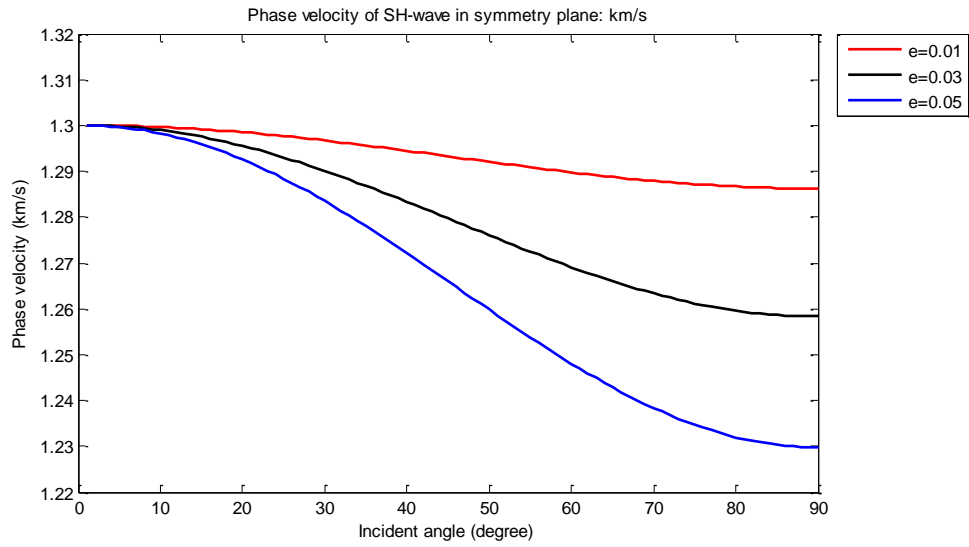


Figure 4.9. Phase velocity of SH-wave in the vertical symmetry plane. Model parameters are the same as Figure 4.3 except for crack density.

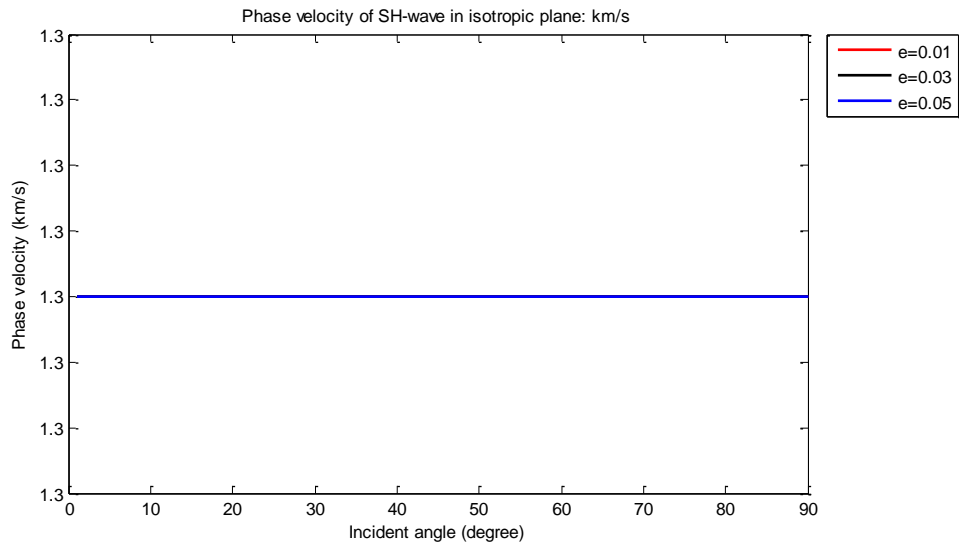


Figure 4.10. Phase velocity of SH-wave in the isotropic plane. Model parameters are the same as Figure 4.3 except for crack density.

Next I will illustrate the reflection coefficients for a model with an isotropic upper medium and a fractured lower medium (dry cracks). The isotropic medium has a P-wave velocity of 2.3 km/s, a S-wave velocity of 1.3 km/s, and a density of 2.7 g/cm<sup>3</sup>. The fractured medium is the same as that shown in Figure 4.3 and Figure 4.4.

Figure 4.11 shows the reflection coefficients for the interface between an isotropic medium and a fractured medium with different incident and azimuthal angles. The reflection coefficients change periodically with azimuthal angles. And this phenomenon is obvious at a large incident angle, whereas it is difficult to see this change for a small incident angle. Based on this change, the orientation and the crack density of the fracture can be recovered from the amplitude of the seismic wave. I will discuss this inversion problem in the next chapter.

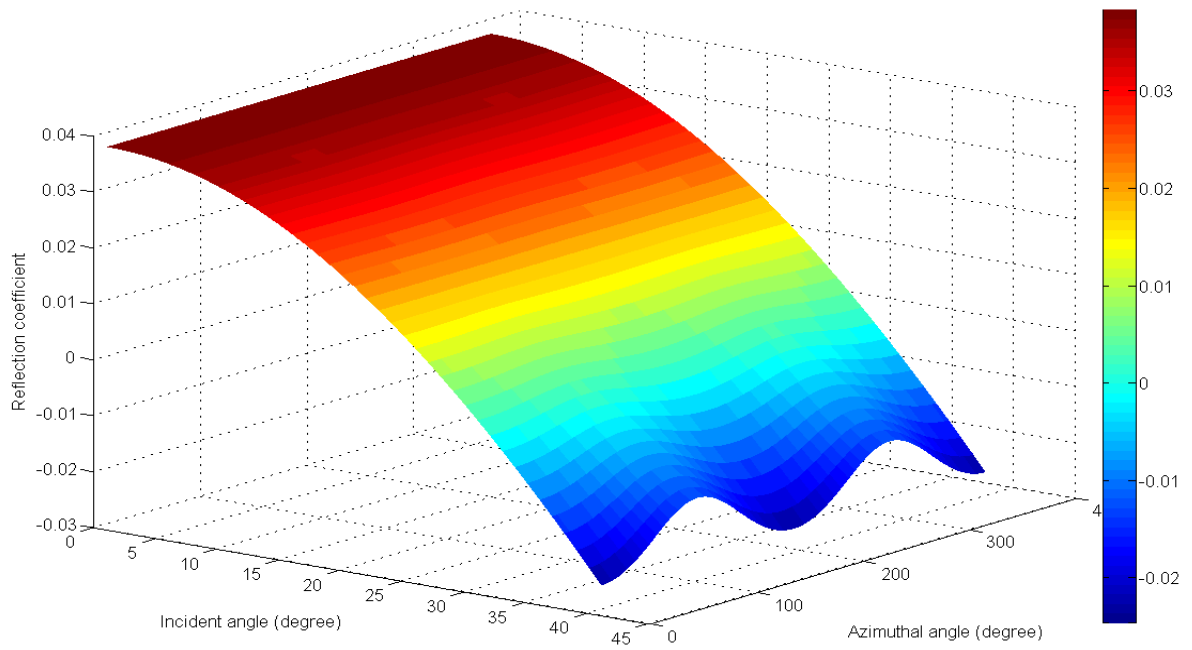


Figure 4.11. Reflection coefficients for the interface between an isotropic medium and a fractured medium.

## 4.5 Bond transformation

In real field studies, the orientation of the fractures or anisotropic medium is not exact the same as the orientation used in modeling. So, we have to rotate our coordinate system to fit the coordinate system of field data. In this study, I introduce Bond transformation to rotate the coordinates in order to obtain the effective medium of a set of vertical fractures which has different orientations. The azimuthal angle I gave in the rotation is equal to the fracture orientation. After using Voigt notation to specify a fourth-rank tensor in terms of a six by six matrix, the Voigt notation no longer obeys the tensor transformation, and we have to use Bond transformation to rotate the coordinates. I assume the three axes before rotation are X, Y, and Z and the three axes after rotation are X', Y', and Z'. The relationship of the cosine values between these two coordinate systems can be expressed as Table 4.1.

TABLE 4.1. Coordinate cosine values between pre- and post-rotation.

	X	Y	Z
X'	$\alpha_1$	$\beta_1$	$\gamma_1$
Y'	$\alpha_2$	$\beta_2$	$\gamma_2$
Z'	$\alpha_3$	$\beta_3$	$\gamma_3$

*Note:* Prime values are post- and unprimed are pre-rotation.

I assume that  $\sigma$ ,  $\epsilon$ , and  $c$ , and  $\sigma'$ ,  $\epsilon'$ , and  $c'$  are the stress, strain, and stiffness matrix before rotation and after rotation. Then, we can obtain two equations for strain and stress as

$$\sigma' = M \cdot \sigma , \quad (4.27)$$

$$\varepsilon = M^T \cdot \varepsilon' , \quad (4.28)$$

where

$$M = \begin{bmatrix} \alpha_1^2 & \beta_1^2 & \gamma_1^2 & 2\beta_1\gamma_1 & 2\alpha_1\gamma_1 & 2\alpha_1\beta_1 \\ \alpha_2^2 & \beta_2^2 & \gamma_2^2 & 2\beta_2\gamma_2 & 2\alpha_2\gamma_2 & 2\alpha_2\beta_2 \\ \alpha_3^2 & \beta_3^2 & \gamma_3^2 & 2\beta_3\gamma_3 & 2\alpha_3\gamma_3 & 2\alpha_3\beta_3 \\ \alpha_2\alpha_3 & \beta_2\beta_3 & \gamma_2\gamma_3 & \beta_2\gamma_3 + \beta_3\gamma_2 & \alpha_2\gamma_3 + \alpha_3\gamma_2 & \alpha_2\beta_3 + \alpha_3\beta_2 \\ \alpha_1\alpha_3 & \beta_1\beta_3 & \gamma_1\gamma_3 & \beta_1\gamma_3 + \beta_3\gamma_1 & \alpha_1\gamma_3 + \alpha_3\gamma_1 & \alpha_1\beta_3 + \alpha_3\beta_1 \\ \alpha_1\alpha_2 & \beta_1\beta_2 & \gamma_1\gamma_2 & \beta_1\gamma_2 + \beta_2\gamma_1 & \alpha_1\gamma_2 + \alpha_2\gamma_1 & \alpha_1\beta_2 + \alpha_2\beta_1 \end{bmatrix} .$$

We can write the relationship between stress and strain based on equation (4.27) and equation (4.28) as

$$\sigma' = M \cdot c \cdot M^T \cdot \varepsilon' . \quad (4.29)$$

Then  $c'$  can be written as

$$c' = M \cdot c \cdot M^T . \quad (4.30)$$

Following the steps presented above, I rotate the model, which has the same parameters shown in Figure 4.3 and Figure 4.4, by  $25^\circ$  in a clockwise direction. Figure 4.12 shows how the P-wave velocity changes after rotation. We can also invert for the orientation of fractures based on the amplitude method which will be discussed in the next chapter and then match the observation system with the effective medium.

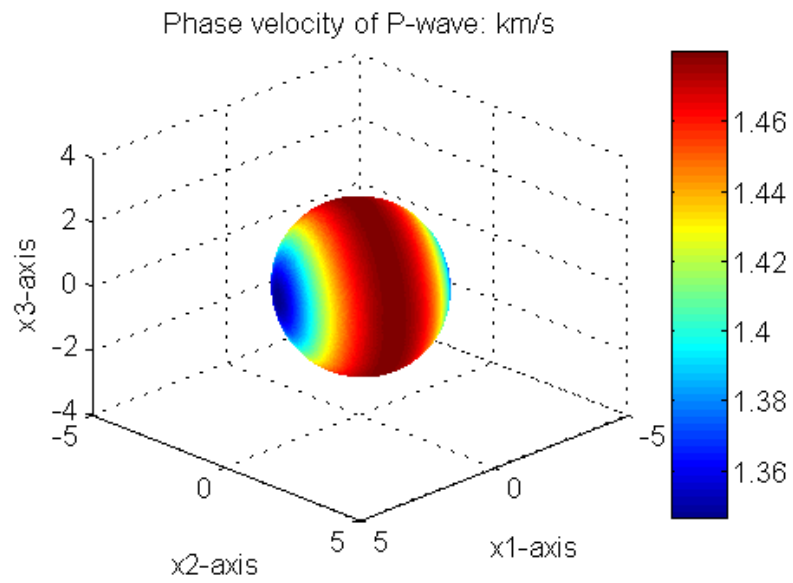
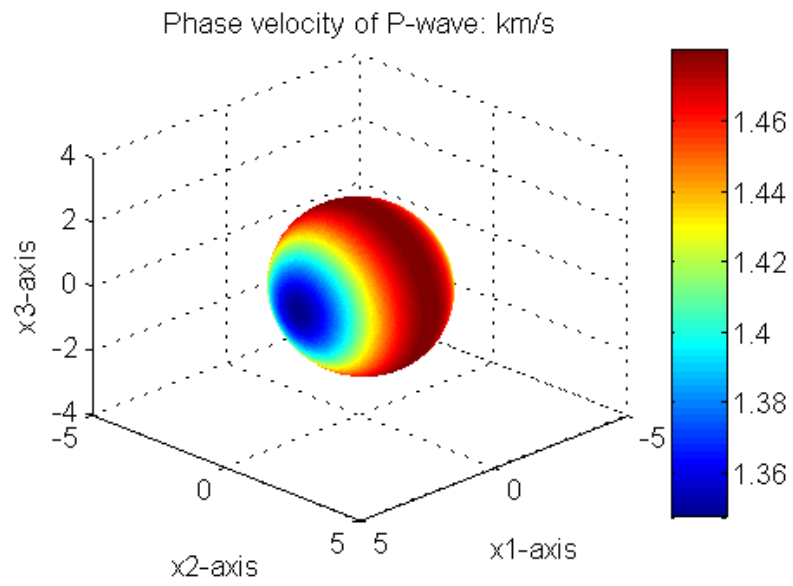


Figure 4.12. P-wave velocity of a fractured rock before rotation and after rotation. The model parameters are the same as those given for Figure 4.3.

## 4.6 Accuracy

We discussed the effective medium theory above based on several assumptions. The theory assumes that the cracks in the host rock are isolated and penny-shaped. Real fractures, however, are not always isolated voids with low aspect ratio in the host rock. So the validation of the effective medium theory to practical field data seems to be a critical issue for the use of this theory. It is very important to know if the results of this effective medium theory are accurate enough, in spite of the fact that some of the basic theoretical assumptions are violated.

For real field data, most aligned sets of fractures are connected, non-circular, microcorrugated, and have a considerable aspect ratio. If there is more than one fracture set in a host rock, intersecting fractures might occur. However, Grechka and Kachanov (2006) state that, “Micromechanics analysis identified a number of geometric features of cracks that are insignificant for the effective properties. These features are (1) Fracture intersections; (2) Microcorrugation of fracture faces; and (3) Random irregularities of fracture shapes, provided that the cracks are flat.” For a single set of fractures, I am mainly concerned with the effect caused by the interaction and the irregularities of fracture shapes which violate basic assumptions.

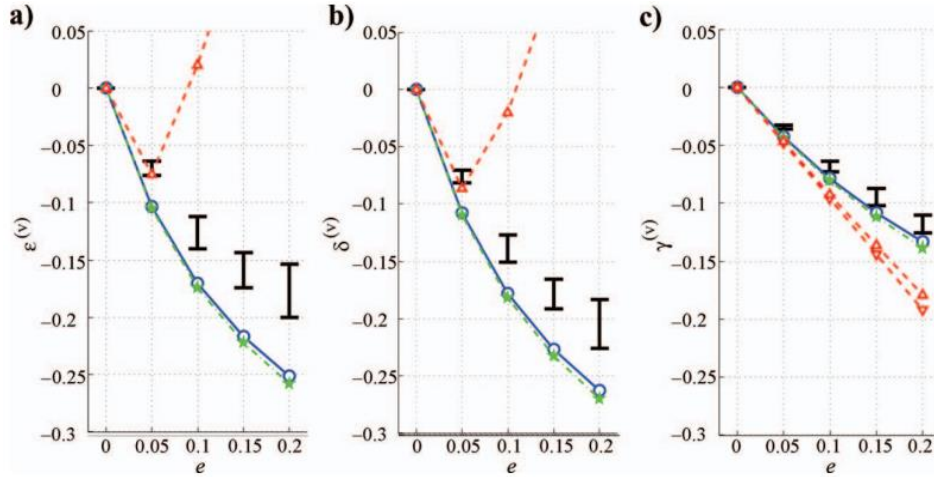


Figure 4.13. Anisotropic parameters (a)  $\varepsilon^{(v)}$  (b)  $\delta^{(v)}$  and (c)  $\gamma^{(v)}$  for a single set of vertical penny-shaped dry cracks (Grechka and Kachanov, 2006).  
*Note:* The background P-wave velocity is 3.0 km/s and S-wave velocity is 1.0 km/s; and density is 2.2 g/cm<sup>3</sup>. Symbols indicate different theoretical predictions: red  $\nabla$  - the first-order Hudson's method, red  $\Delta$  - the second-order Hudson's method,  $\star$  - Schoenberg's method, and blue  $\circ$  - the non-interaction approximation (Grechka and Kachanov, 2006) that takes into account the crack aspect equals 0.05 for all fractures. Bars correspond to the 95% confidence intervals (the mean values  $\pm 2$  standard deviations) of the numerically computed anisotropic parameters obtained for 100 random realizations of the fracture locations.

Figure 4.13 (Grechka and Kachanov, 2006) shows how the interaction of fractures affect the anisotropic parameters with increasing crack density. When the crack density is lower than 0.05, the effects in Figure 4.13(a) and Figure 4.13(b) for  $\varepsilon^{(v)}$  and  $\delta^{(v)}$  are tolerable. And with crack density decreasing, the effect is decreasing and it is vanished when crack density becomes 0 which is reasonable. We care more about the effect on  $\gamma^{(v)}$  in figure 4.13(c) which is the direct estimation of crack density. Surprisingly, the interaction almost has no effect on  $\gamma^{(v)}$  so that violating the assumption of non-interaction is not going to reduce the accuracy of the result calculating by Schoenberg's theory.

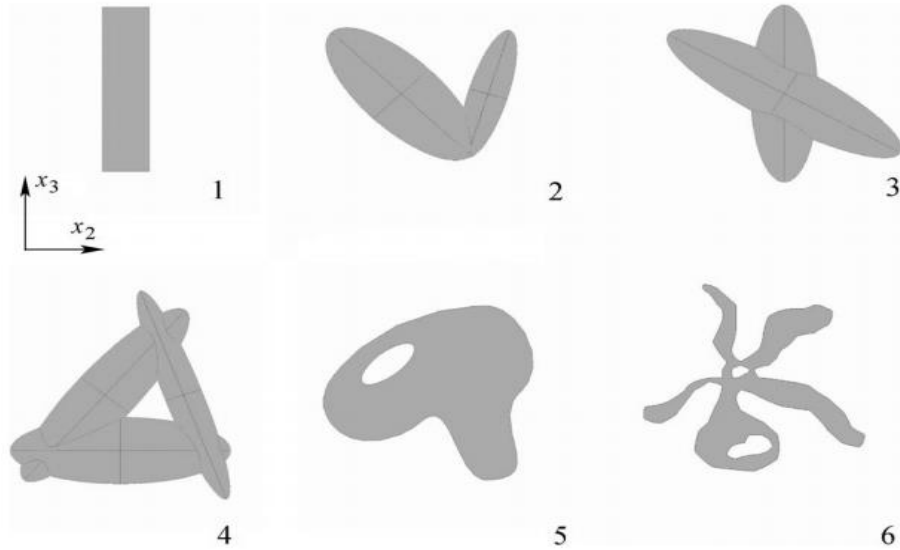


Figure 4.14. Irregular vertical cracks. All fractures are planar; Their normals are directed along the  $x_1$  - axis . The faces of cracks 2, 3, and 4 have sharp edges. Geometries 4, 5, and 6, that contain interior rock islands, represent partially closed fractures (Grechka and Kachanov, 2006).

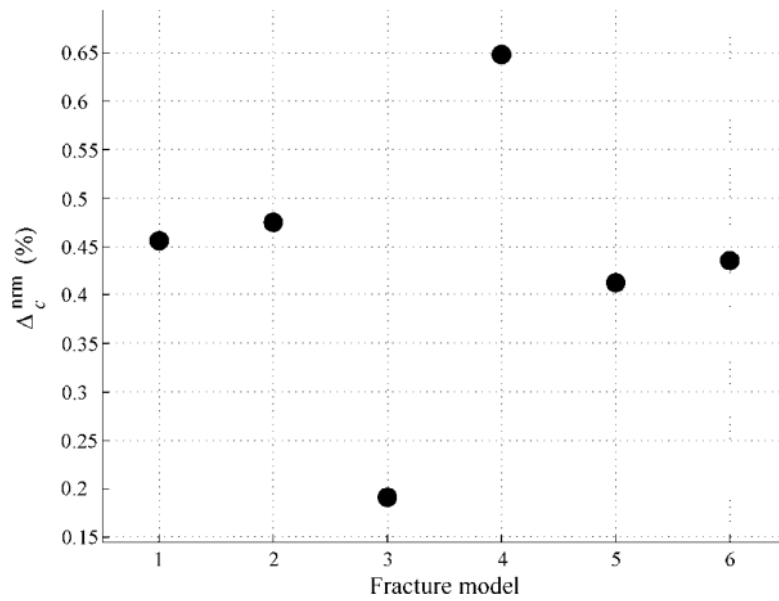


Figure 4.15. Misfits  $\Delta_c^{nm}$  for six fracture shapes in Figure 4.14 (Grechka and Kachanov, 2006).

For non-circular cracks, Grechka and Kachanov (2006) give six irregular fracture shapes, which are shown in Figure 4.14. They use each of the six irregular fractures to build a single vertical fracture. The fractures in the host rock have random locations and random orientations in the vertical plane. They compute the average rotations in effective stiffness  $\langle C_e \rangle$  and the excess stiffness can be written as

$$\langle \Delta C \rangle = \langle C_e \rangle - C_b . \quad (4.31)$$

And the fitting method is used to find the crack density and aspect ratio for each fracture in Figure 4.14. Then, the excess stiffness which caused by penny-shaped crack can be written as

$$\Delta C^P = C_e^P - C_b . \quad (4.32)$$

The stiffness misfit is expressed as

$$\Delta_c = \langle \Delta C \rangle - \Delta C^P . \quad (4.33)$$

The magnitude of the misfits of excess stiffness is evaluated by calculating the maximum norm,

$$\Delta_c^{nm} = \frac{\max |\Delta_c|}{\max |\langle \Delta C \rangle|} \times 100\% . \quad (4.34)$$

Figure 4.15 shows the maximum norm of the misfits of excess stiffness which is smaller than 0.65%. A conclusion can be made that the flat cracks with random shape and random location can be represented by penny-shaped cracks according to the effective elasticity. Although only dry cracks are discussed here, this conclusion is also valid for fluid-filled cracks due to much weaker influences are made on fluid-filled cracks.

## 4.7 Conclusion

When the seismic wavelengths are much larger than the fracture size and spacing, it is convenient to use elastic compliance to formulate the equivalent anisotropic medium problem for seismic modeling of sets of aligned fractures embedded in host medium. The linear slip theory (Schoenberg and Sayers, 1995) provides a direct method to relate the seismic signatures to the properties of fracture systems. Normal ( $\Delta N$ ) and tangential ( $\Delta T$ ) weaknesses, introduced by Hsu and Schoenberg (1993), are two essential parameters of linear slip theory for rotationally invariant fractures. For penny-shaped cracks, by comparing Schoenberg's method and Hudson's method (1981), the normal and tangential weaknesses can be expressed in terms of the crack density and the ratio of P-wave and S-wave velocities of the host rock. A set of vertical, aligned, rotationally invariant fracture leads to a particular HTI medium called TI (LSD). Only four independent parameters are required to specify a TI (LSD) medium. Rüger's anisotropic parameters for TI (LSD) media ( $\delta^{(V)}$ ,  $\varepsilon^{(V)}$ ,  $\gamma^{(V)}$ ) can be expressed in an approximated linear form in terms of the normal and tangential weaknesses and the ratio of P-wave and S-wave velocities. If the cracks are dry, the  $\gamma^{(V)}$  approximately equals the crack density. Interactions between fractures and the shape of cracks do not affect the accuracy of Schoenberg's method, according to Grechka and Kachanov (2006). The information that can be obtained from seismic data is only the fracture orientation and a rough estimate of crack density. The estimation of shape, size, and distribution of the fracture is beyond the capability of long wavelength seismic data.

# CHAPTER 5

## AVAZ INVERSION

### 5.1 Introduction

Reflectivity inversion of P-wave data for fracture orientation and density are discussed in this chapter. Two different inversion methods are applied. The first is based on Rüger's linear approximation and the second on the exact reflection coefficients, which are discussed in Chapter 2. This chapter follows the method suggested by Minsley *et al.* (2003) to invert for fracture orientation from P-wave reflectivity. After obtaining information about the fracture orientation, three anisotropic terms ( $\delta^{(V)}$ ,  $\varepsilon^{(V)}$ ,  $\gamma^{(V)}$ ) and three isotropic terms ( $\frac{\Delta\alpha}{\bar{\alpha}}$ ,  $\frac{\Delta\beta}{\bar{\beta}}$ , and  $\frac{\Delta\rho}{\bar{\rho}}$ ) are inverted by the modified Rüger's linear approximation. Moreover, errors caused by factors such as S/N ratio, maximum incident angle, and error propagation are analyzed in this chapter.

### 5.2 SVD inversion

Singular value decomposition (SVD) is a popular and precise method to solve linear least-squares problems (Sheriff, 1991). Jin *et al.* (1993) state that SVD is effective for the stabilization of AVO inversion, because it provides a precise way to analyze a matrix and obtain a stable but approximate inversion. Therefore, the SVD method is widely used for various linear inversions in geophysics. The SVD method decomposes a general rectangular matrix  $G$  of  $m$  rows and  $n$  columns in terms of a multiplication of three matrices as

$$G = U\Lambda V^T, \quad (5.1)$$

where  $U$  is the matrix of eigenvectors of  $GG^T$  which span the data space, and  $V$  is the matrix of eigenvectors of  $GG^T$  which span the model space.  $\Lambda$  is a rectangular diagonal matrix in decreasing order, which contains singular values (or principle values) of the matrix  $G$ . And the SVD matrix of  $G$  can also be written in a reduced SVD form as (Menke, 1989)

$$G = U\Lambda V^T = U_p \Lambda_p V_p^T, \quad (5.2)$$

where  $\Lambda_p$  is the diagonal matrix of matrix  $G$  with non-zero diagonal elements.  $U_p = [u_1 \dots u_p] \in \mathbb{R}^{p \times p}$  and  $V_p = [v_1 \dots v_p] \in \mathbb{R}^{n \times p}$  are the matrices which contain first  $p$  columns of  $U$  and  $V$ . Because of the non-zero diagonal elements in  $\Lambda_p$ , the generalized inversion which is the Lanczos inverse of matrix  $G$  can be defined as

$$G_g^{-1} = V_p \Lambda_p^{-1} U_p^T = V_p \left[ \text{diag} \left( \frac{1}{\sigma_p} \right) \right] U_p^T. \quad (5.3)$$

For the generalized inverse matrix in equation (5.3), we obtained the following equations,

$$G_g^{-1} G G_g^{-1} = G_g^{-1}, \quad (5.4)$$

$$G G_g^{-1} G = G. \quad (5.5)$$

Consider a matrix,

$$Gm = d, \quad (5.6)$$

where  $m$  is the matrix of the model,  $d$  is the matrix of the data and  $G$  is a mapping from the model space to the data space. We can apply the generalized inverse matrix  $G_g^{-1}$  to

both sides of equation (5.6) and yield

$$G_g^{-1}Gm = G_g^{-1}d . \quad (5.7)$$

Form equation (5.7), we can express the estimated solution vector  $m^{est}$  as

$$m^{est} = G_g^{-1}d . \quad (5.8)$$

According to equation (5.8) and equation (5.6),  $m^{est}$  becomes

$$m^{est} = G_g^{-1}d \cong (G_g^{-1}G)m = (V_p V_p^T)m , \quad (5.9)$$

where  $G_g^{-1}G$  is defined as model resolution matrix and yields the following form

$$R = G_g^{-1}G = V_p V_p^T . \quad (5.10)$$

The model resolution matrix evaluates how well the estimated solution  $m^{est}$  resolves the true solution  $m$ . When the resolution matrix becomes an identity matrix,  $m^{est}$  is the perfect solution for the inversion problem. And, it is a good way to analyze the diagonal elements of the resolution matrix in order to evaluate the model resolution. The non-unit diagonal elements means that the estimated values in  $m^{est}$  are linear combinations of the true values. Replacing the  $G_g^{-1}$  by its definition in equation (5.3), the estimated solution vector can be written as

$$m^{est} = V_p \Lambda_p^{-1} U_p^T d . \quad (5.11)$$

Based on equation (5.8),  $m^{est}$  can be obtained by knowing the data matrix  $d$  and the matrices  $V_p$ ,  $\Lambda_p^{-1}$ , and  $U_p$  from matrix  $G$ .

The condition number of a matrix, which is defined as the ratio of the largest to the smallest singular values, is a good measure for the singularity of the matrix. Jin *et al.*

(2002) suggest that a well-posed matrix has a condition number which is not far from unity, and a matrix is ill-posed when the condition number becomes very large. Consequently, the condition number is considered as an important factor to estimate the singularity of the matrix.

The matrix  $\Lambda$  is also an identifier for the possible instability in the numerical calculation of  $m^{est}$ . A common difficulty occurs in inverting a matrix when some elements in the matrix are very small, even close to zero, that the inverted results become very large and are dominated by numerical round off error. One way to overcome this problem is to pick some cutoff size for singular values and set the values which are smaller than this value to zero. This method excludes the small singular values in the matrix and thus a better solution is obtained with a smaller variance. Another way to solve this problem is to include these small singular values but damp them. Menke (1989) states “This change has little effect on the larger eigenvalues but prevents the smaller ones from leading to large variances.” The damped generalized inverse can be written as

$$G_g^{-1} = V_p \Lambda_p (\Lambda_p^2 + K^2 \mathbf{I})^{-1} U_p^T, \quad (5.12)$$

and the model resolution matrix yields the form

$$R = V_p \Lambda_p^2 (\Lambda_p^2 + K^2 \mathbf{I})^{-1} V_p^T, \quad (5.13)$$

where  $K^2$  is the damping factor. The value for the damping factor is chosen by a trial-and-error process which weighs the relative merits of having a solution with small variance against one that is well resolved (Menke, 1989). The ability to make reliable interpretations from an unknown parameter  $m^{est}$  requires good resolution and small

variance. However, it is always a trade-off to make a choice between resolution and variance. Thus, it is important to choose the appropriate value for the damping factor.

Comparing the SVD method and the least-squares method, both of their equations yield similar forms. The difference is that the SVD method is going to find the least-squares best compromise solution. The merit of SVD is it provides a solution when the matrix is singular or numerically very close to singular.

### 5.3 Generalized linear inversion

The generalized linear inversion (GLI) is discussed here following the notation introduced by Cooke and Schneider (1983). GLI is based on Taylor series expansion of the forward model and it yields the following form

$$F(\bar{\mathbf{I}}) = F(\bar{\mathbf{I}\bar{\mathbf{G}}}) + \frac{\partial F(\bar{\mathbf{I}\bar{\mathbf{G}}})}{\partial(\bar{\mathbf{I}\bar{\mathbf{G}}})}(\bar{\mathbf{I}} - \bar{\mathbf{I}\bar{\mathbf{G}}}) + \frac{\partial^2 F(\bar{\mathbf{I}\bar{\mathbf{G}}})(\bar{\mathbf{I}} - \bar{\mathbf{I}\bar{\mathbf{G}}})^2}{\partial(\bar{\mathbf{I}\bar{\mathbf{G}}})^2 2!} + \dots, \quad (5.14)$$

where,  $\bar{\mathbf{I}}$  = True solution,

$\bar{\mathbf{I}\bar{\mathbf{G}}}$  = Initial guess of the solution,

$\bar{\mathbf{I}} - \bar{\mathbf{I}\bar{\mathbf{G}}}$  = Error in the above guess,

F = Forward modeling function,

$F(\bar{\mathbf{I}})$  = Observed seismic data,

$F(\bar{\mathbf{I}\bar{\mathbf{G}}})$  = Data calculated using  $\bar{\mathbf{I}\bar{\mathbf{G}}}$  in the forward modeling algorithm, and

$\frac{\partial F(\bar{\mathbf{I}\bar{\mathbf{G}}})}{\partial(\bar{\mathbf{I}\bar{\mathbf{G}}})}$  = Partial derivative matrix.

From equation (5.14), we calculate  $(\bar{\mathbf{I}} - \bar{\mathbf{I}\bar{\mathbf{G}}})$  in order to correct the initial guess to make it closer or even equal to the true solution. However,  $(\bar{\mathbf{I}} - \bar{\mathbf{I}\bar{\mathbf{G}}})$  cannot be inverted from the

infinite series in equation (5.14). Thus a truncated linear equation is used to solve this problem. And it can be written as

$$F(\bar{I}) = F(\bar{IG}) + \frac{\partial F(\bar{IG})}{\partial(\bar{IG})}(\bar{I} - \bar{IG}) . \quad (5.15)$$

In equation (5.15),  $(F(\bar{I}) - F(\bar{IG}))$  is defined as the difference vector which is generated by subtracting the data computed by forward modeling from observed seismic data. The term  $\frac{\partial F(\bar{IG})}{\partial(\bar{IG})}$ , which is a partial derivative, is the so-called sensitivity matrix. And the

term to be solved for,  $(\bar{I} - \bar{IG})$ , is called the correction vector. This correction vector is used to solve for  $\bar{I}$  by adding the correction vector to initial guess as following

$$\bar{I} \approx \bar{IG} + (\bar{I} - \bar{IG}) . \quad (5.16)$$

Equation (5.16) is an approximation, because the equation (5.15), we used to calculate the correction vector, is not the infinite Taylor series, but a truncated linear equation. Consequently, the solution for  $\bar{I}$  is also an approximation. When there is more than one parameter to be inverted for, it is better to use the matrix form of equation (5.15) which can be expressed as

$$\begin{pmatrix} F(I_1) - F(IG_1) \\ F(I_1) - F(IG_2) \\ \cdot \\ \cdot \\ F(I_M) - F(IG_M) \end{pmatrix} = \begin{pmatrix} \frac{\partial F(IG_1)}{\partial(IG_1)} & \frac{\partial F(IG_1)}{\partial(IG_2)} & \cdot & \cdot & \frac{\partial F(IG_1)}{\partial(IG_N)} \\ \frac{\partial F(IG_2)}{\partial(IG_1)} & \frac{\partial F(IG_2)}{\partial(IG_2)} & \cdot & \cdot & \frac{\partial F(IG_2)}{\partial(IG_N)} \\ \cdot & \cdot & \cdot & \cdot & \cdot \\ \cdot & \cdot & \cdot & \cdot & \cdot \\ \frac{\partial F(IG_M)}{\partial(IG_1)} & \frac{\partial F(IG_M)}{\partial(IG_2)} & \cdot & \cdot & \frac{\partial F(IG_M)}{\partial(IG_N)} \end{pmatrix} \begin{pmatrix} I_1 - IG_1 \\ I_2 - IG_2 \\ \cdot \\ \cdot \\ I_M - IG_M \end{pmatrix} , \quad (5.17)$$

where  $M$  is the number of observations (points in the observed data), and  $N$  is the

number of parameters. In order to reduce the error in equation (5.16), iterations are applied where the corrected initial guess in equation (5.16) is used as a new initial guess in equation (5.15) or equation (5.17). The procedure is shown in Figure 5.1.

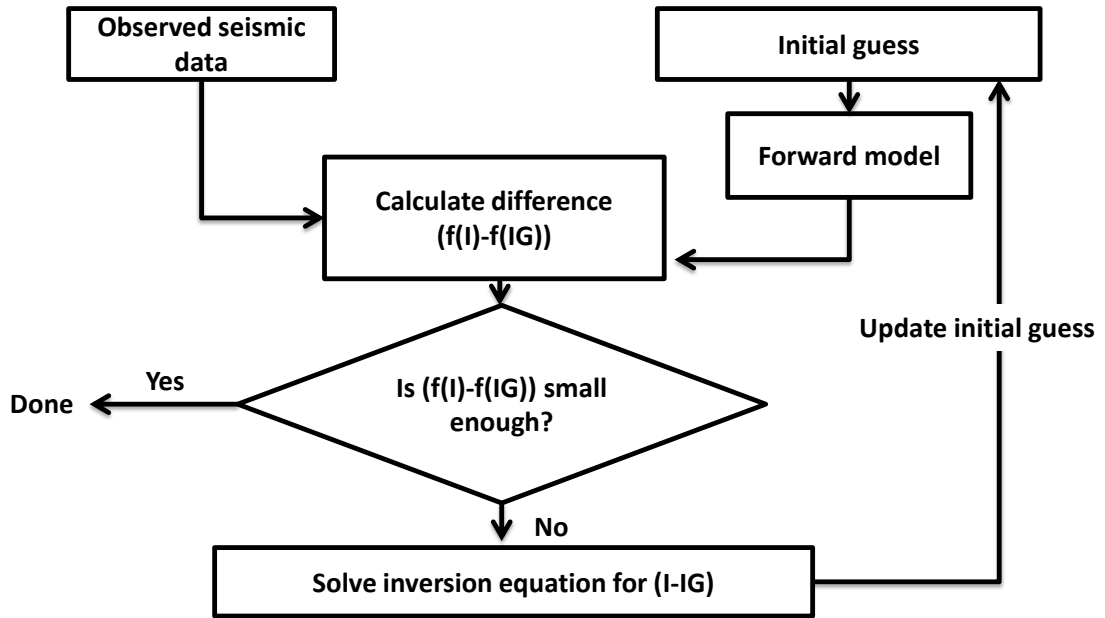


Figure 5.1. Workflow for generalized linear inversion (Cooke and Schneider, 1983).

If the initial guess lies within the range of convergence, the error decreases in a roughly exponential manner with each iteration. This error can be defined by the Euclidean norm as

$$\sum [F(IG) - F(I)]^2 . \quad (5.18)$$

Before the iteration, we have to choose a value for the error level. When the error drops below this level or the new loop cannot provide an improvement over the last iteration, the iteration stops.

In order to solve for the correction vector, the modified least-squares error procedure is applied. A damping factor is included in the modification and the

modification yields,

$$(I - IG) = (S^T S + K^2 I) S^T [F(IG) - F(I)] , \quad (5.19)$$

where

$$S = \frac{\partial F(IG)_i}{\partial IG_j} \text{ (sensitivity matrix),}$$

$K^2 =$  damping factor,

$I =$  identity matrix.

The role that the damping factor plays in GLI is similar to the prewhitening (adding white noise to diagonal of the matrix) usually applied in deconvolution. In real situations, there is always noise in the difference vector or sensitivity matrix, which can lead to a large error in the correction vector. By damping the magnitude of the difference vector, a solution for the difference vector, which favors signal and discriminates against noise, is possibly obtained. Instead of using a constant value for the damping factor, we use different values for each iteration. According to the book *Numerical Recipes (2007)*, damping factors are chosen in the following steps:

1. Pick a modest value for the damping factor like  $K^2 = 0.001$ .
2. Solve equation (5.17) for the correction vector and evaluate the difference vector.
3. If the Euclidean norm of the difference vector is equal or larger than the Euclidean norm of the difference vector of last iteration, then increase  $K^2$  by a factor of 10 and go back to step 2; if the Euclidean norm of the difference vector is less than the Euclidean norm of the difference vector of last iteration, then decrease  $K^2$  by a factor of 10 and go back to step 2.

Equation (5.17) is a system of linear equations which solves for the correction vectors. There is no priori information to constrain the results in the correction vector. Sometimes the correction vector, calculated from equation (5.17), is not realistic. For example, the inversion result of P-wave velocity may be negative. However, it does not necessarily mean that the inversion process is unstable. For this inversion problem, an experienced interpreter has some useful information about the range where the true solution probably lies; e.g. geology background, lithology analyzing, and even general physical constraints, like values for velocity and density are always positive. Constraints are applied to remove the non-sensical results and make the iteration process only work in the realistic bounds.

#### 5.4 Inversion for fracture orientation

When only small incident angle reflections are considered, the third term of Rüger's approximation for PP reflection coefficients can be ignored. The linear approximation equation for reflection coefficients in HTI medium yields

$$R_p^{HTI}(i, \phi) \approx \frac{1}{2} \frac{\Delta Z}{Z} + \frac{1}{2} \left\{ \frac{\Delta \alpha}{\bar{\alpha}} - \left( \frac{2\bar{\beta}}{\bar{\alpha}} \right)^2 \frac{\Delta G}{G} + \left[ \Delta \delta^{(v)} + 2 \left( \frac{2\bar{\beta}}{\bar{\alpha}} \right)^2 \Delta \gamma \right] \cos^2 \phi \right\} \sin^2 i \quad (5.20)$$

In a real field situation, however, the fracture orientation is unknown. Thus,  $\phi$  should be expressed by the difference between the azimuthal direction of the symmetry axis  $\phi_{sym}$  of the fractured medium and the azimuthal direction  $\phi_k$  of the  $k$ -th observed azimuth. So, equation (5.20) can be written as

$$R_{pp} \approx A + [B^{iso} + B^{ani} \cos^2(\phi_k - \phi_{sym})] \sin^2 i \quad (5.21)$$

where

$$A = \frac{1}{2} \frac{\Delta Z}{\bar{Z}},$$

$$B^{iso} = \frac{1}{2} \left[ \frac{\Delta \alpha}{\bar{\alpha}} - \left( \frac{2\bar{\beta}}{\bar{\alpha}} \right)^2 \frac{\Delta G}{\bar{G}} \right],$$

$$B^{ani} = \frac{1}{2} \left[ \Delta \delta^{(V)} + 2 \left( \frac{2\bar{\beta}}{\bar{\alpha}} \right)^2 \Delta \gamma \right] \cos^2(\varphi_k - \varphi_{sym})$$

In order to use SVD to do inversion, equation (5.21) must be linearized. Based on the two trigonometric identities

$$\cos^2(\varphi_k - \varphi_{sym}) = \frac{1}{2} (1 + \cos(2\varphi_k - 2\varphi_{sym})), \quad (5.22)$$

$$\cos(2\varphi_k - 2\varphi_{sym}) = \cos 2\varphi_k \cos 2\varphi_{sym} + \sin 2\varphi_k \sin 2\varphi_{sym}, \quad (5.23)$$

equation (5.21) can be written in a linear form as

$$R_{pp} \approx A + (B^{iso} + \frac{1}{2} B^{ani}) \sin^2 i + (\frac{1}{2} B^{ani} \cos 2\varphi_{sym}) \cos 2\varphi_k \sin^2 i + (\frac{1}{2} B^{ani} \sin 2\varphi_{sym}) \sin 2\varphi_k \sin^2 i, \quad (5.24)$$

or in terms of four unknowns

$$R_{pp} \approx C_1 + C_2 \sin^2 i + C_3 \cos 2\varphi_k \sin^2 i + C_4 \sin 2\varphi_k \sin^2 i, \quad (5.25)$$

where

$$\begin{aligned} A &= C_1, \\ B^{ani} &= \pm 2 \sqrt{C_3^2 + C_4^2}, \\ B^{iso} &= C_2 - \frac{1}{2} B^{ani}, \\ \phi_{sym} &= \frac{1}{2} \arctan \frac{C_4}{C_3}. \end{aligned}$$

According to the inversion results, the fracture orientation which is perpendicular to the symmetry axis can be recovered. Numerical tests are applied based on SVD and equation (5.25) to invert for the fracture orientation (or the direction of the symmetry axis). Exact reflection coefficients are acquired along 18 azimuths with an interval of  $10^\circ$ .

There are 40 receivers located in each azimuth with  $1^\circ$  incident-angle interval. The model

parameters in these tests are as follows:  $\frac{\Delta\alpha}{\bar{\alpha}} = 0.1$ ,  $\frac{\Delta Z}{\bar{Z}} = 0.1$ ,  $\frac{\Delta G}{\bar{G}} = 0.2$ ,  $\delta^{(v)} = -0.05$ ,

$\varepsilon^{(v)} = -0.05$ , and  $\gamma = 0.15$ . The P-wave velocity for the lower HTI medium in the isotropic plane is 2.5 km/s, the SH-wave velocity in the isotropic plane is 1.5 km/s, and the density is  $2.7 \text{ g/cm}^3$ . The data are calculated by the exact reflection coefficients method introduced by Chattopadhyay (2004). The Bond transformation, discussed in Chapter 4, is applied to rotate the symmetry axis in the lower HTI medium by  $20^\circ$  and  $110^\circ$ . The rotation angles have  $90^\circ$  difference, which is used to test the ambiguity of the inversion results. Figures 5.2 to 5.12 show the inversion results of the fracture orientation based on the SVD and Rüger's equation for reflection coefficients with different noise levels. Figure 5.13 and Figure 5.14 show the results which used GLI and Chattopadhyay's method. These two different sets of results provide some insight on how to choose the proper method to invert for fracture orientation. In Figure 5.2, the inversion result with S/N ratio of 20 is approaching  $20^\circ$  after using four azimuthal lines. Figure 5.3 shows the error is within a tolerable range when three azimuthal lines are used in the inversion. However, increasing the number of azimuthal lines does not decrease the error after five azimuthal lines. Five azimuthal lines have already provided an almost exact

solution for fracture orientation. Figure 5.4 shows the inversion result with the same S/N but with a different rotation angle. Although the rotation angle for Figure 5.4 is  $110^\circ$ , the inversion result is still approaching  $20^\circ$ , and it remains the same after using three azimuthal lines. This phenomenon also happens in Figures 5.8 and 5.11. If we ignore the  $90^\circ$  error in Figures 5.4, 5.8, and 5.11, all the numerical tests yield good results for S/N as low as 5. For the model with S/N=5, the damping factor is not required in the SVD inversion. The inversion for fracture orientation does not seem to be sensitive to mild noise contamination (S/N > 5), which means with reasonably high-quality field data, it is possible to obtain accurate enough information about the fracture orientation.

In order to analyze the  $90^\circ$  ambiguity, we have to look at equation (5.21) again. For a given incident angle, the reflection coefficients will plot as a sinusoid curve with a period of  $180^\circ$ . And the ambiguity is intrinsic when equation (5.21) is used for inversion. From a mathematical aspect, there is no unique solution for equation (5.21), even with redundant data. If the sign of  $B^{ani}$  is changed,  $B^{iso}$  will be regrouped in order to satisfy the equation, and at the meantime  $\phi_{sym}$  is rotated by  $90^\circ$ . In other words, for a given set of azimuthal reflection coefficients, there are always two sets of solutions,  $(A, B^{iso}, B^{ani}, \phi_{sym})$  and  $(A, B^{iso'}, B^{ani'}, \phi_{sym}')$  for equation (5.21), where  $B^{iso'} = B^{iso} + B^{ani}$ ,  $B^{ani'} = -B^{ani}$ , and  $\phi_{sym}' = \phi_{sym} - 90^\circ$ .

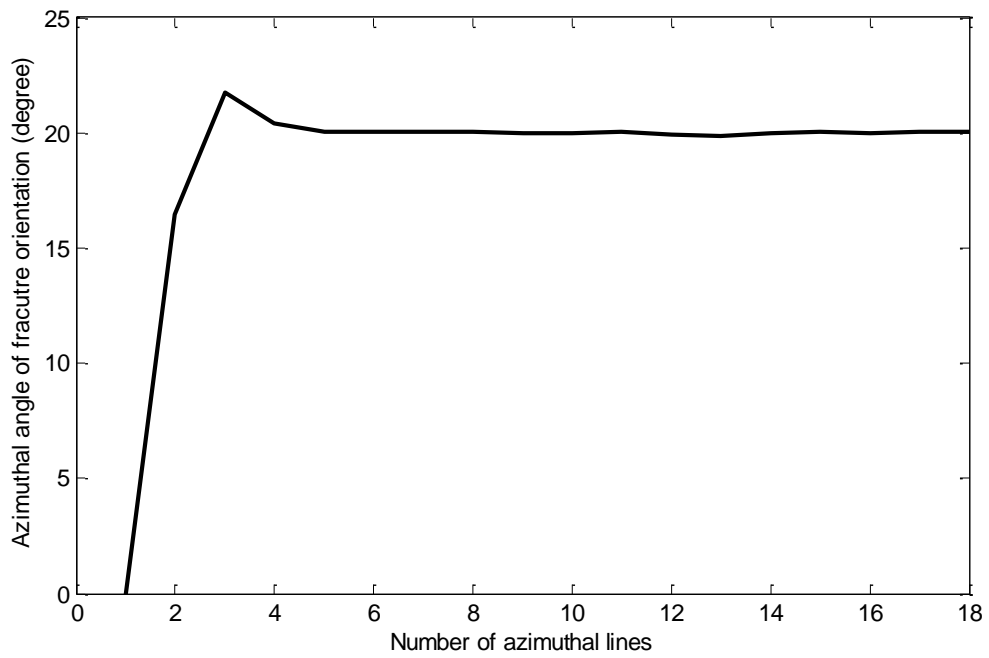


Figure 5.2. Inversion result for the fracture orientation. The lower HTI medium is rotated by 20°. S/N = 20.

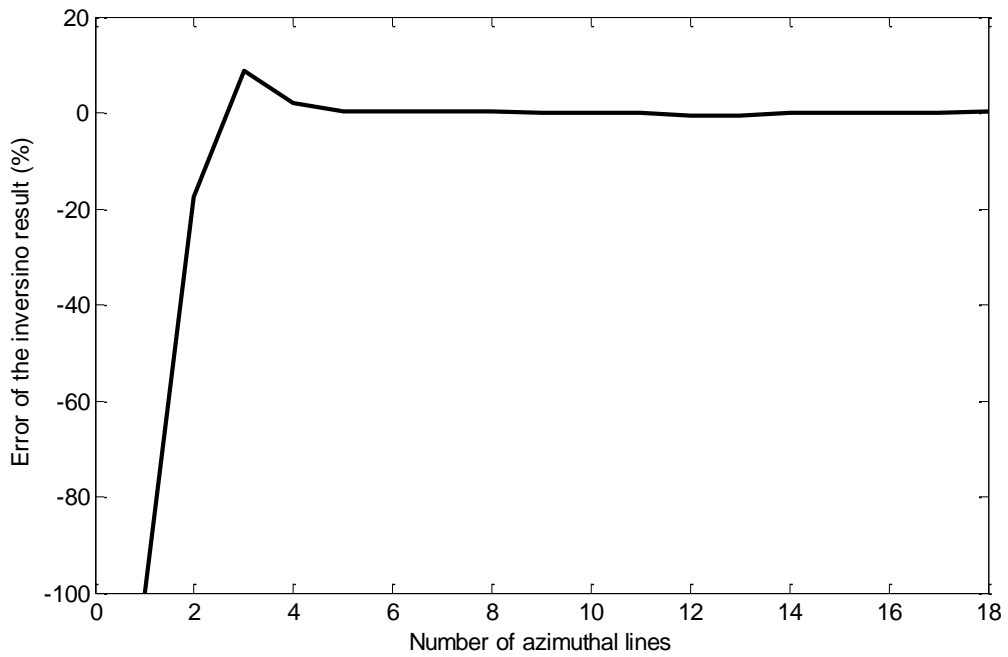


Figure 5.3. Error of inversion result for the fracture orientation. The lower HTI medium is rotated by 20°. S/N = 20.

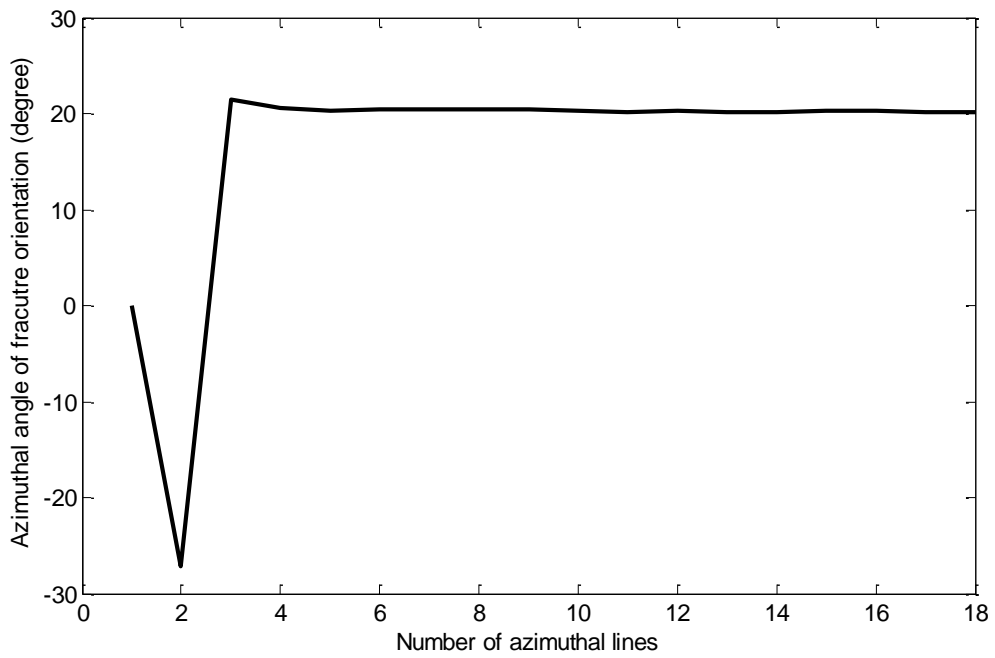


Figure 5.4. Inversion result for the fracture orientation. The lower HTI medium is rotated by  $110^\circ$ .  $S/N = 20$ .

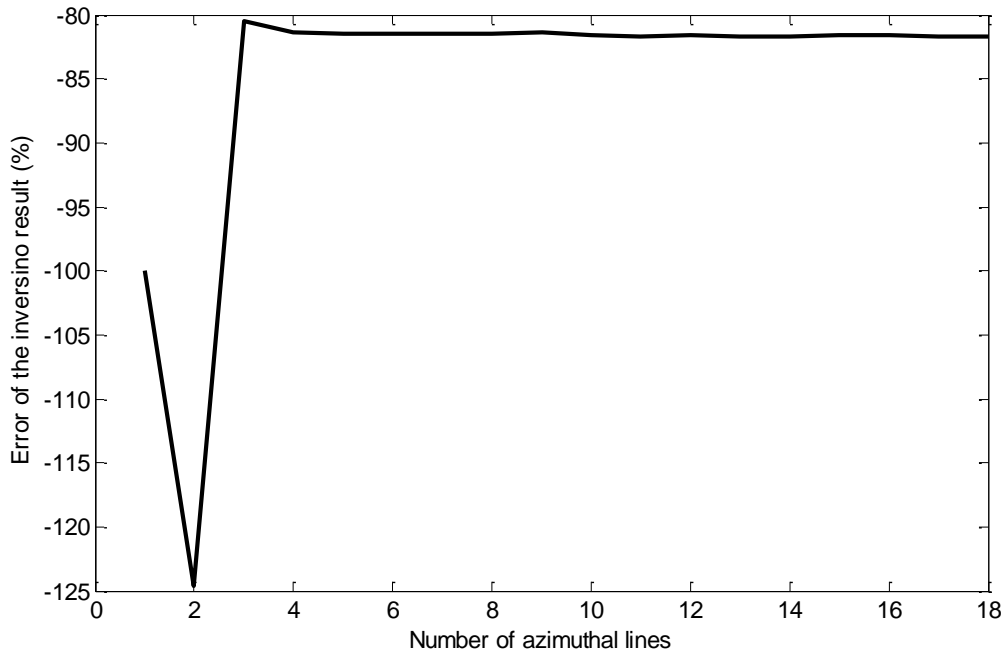


Figure 5.5. Error of inversion result for the fracture orientation. The lower HTI medium is rotated by  $110^\circ$ .  $S/N = 20$ .

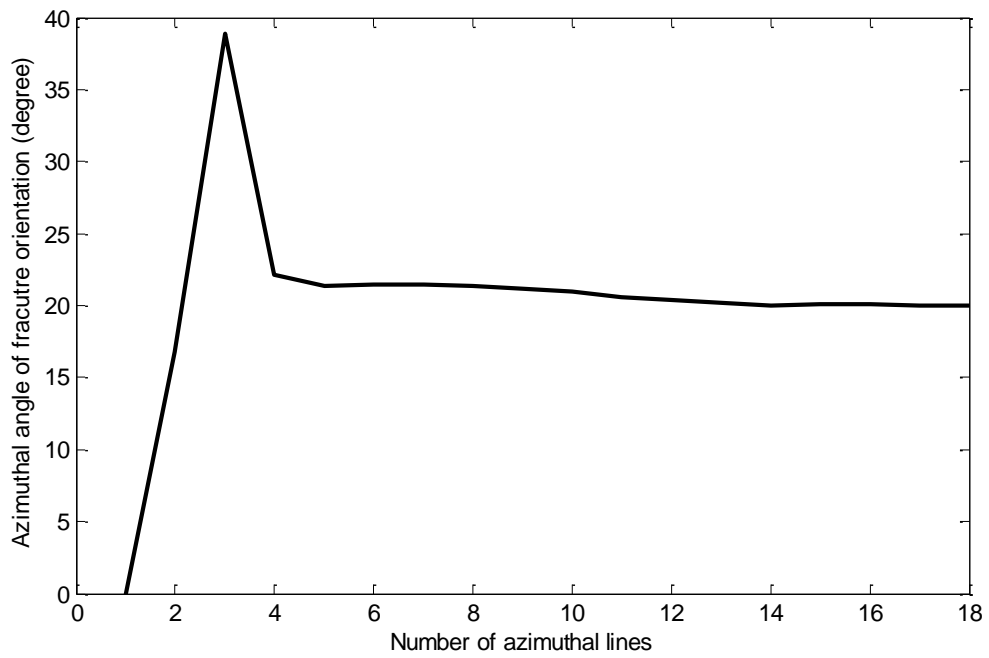


Figure 5.6. Inversion result for the fracture orientation. The lower HTI medium is rotated by 20°. S/N = 10.

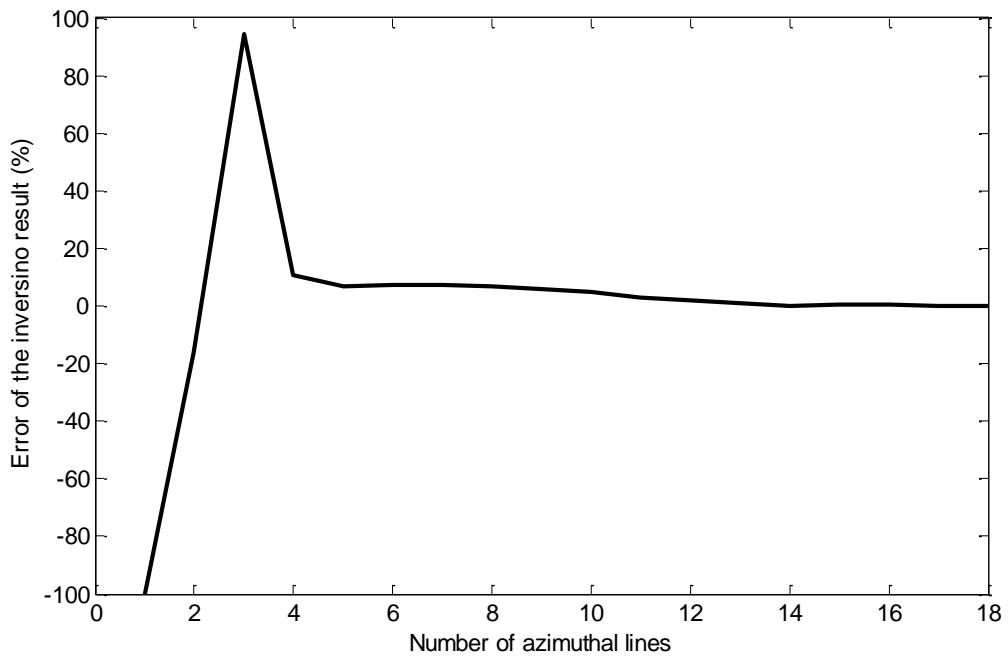


Figure 5.7. Error of inversion result for the fracture orientation. The lower HTI medium is rotated by 20°. S/N = 10.

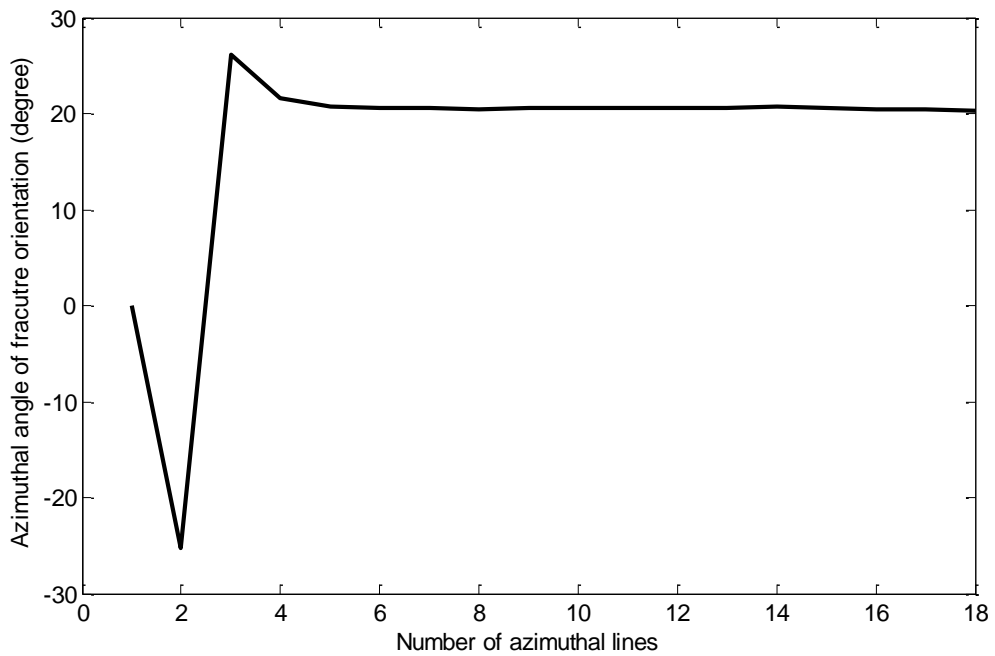


Figure 5.8. Inversion result for the fracture orientation. The lower HTI medium is rotated by  $110^\circ$ . S/N = 10.

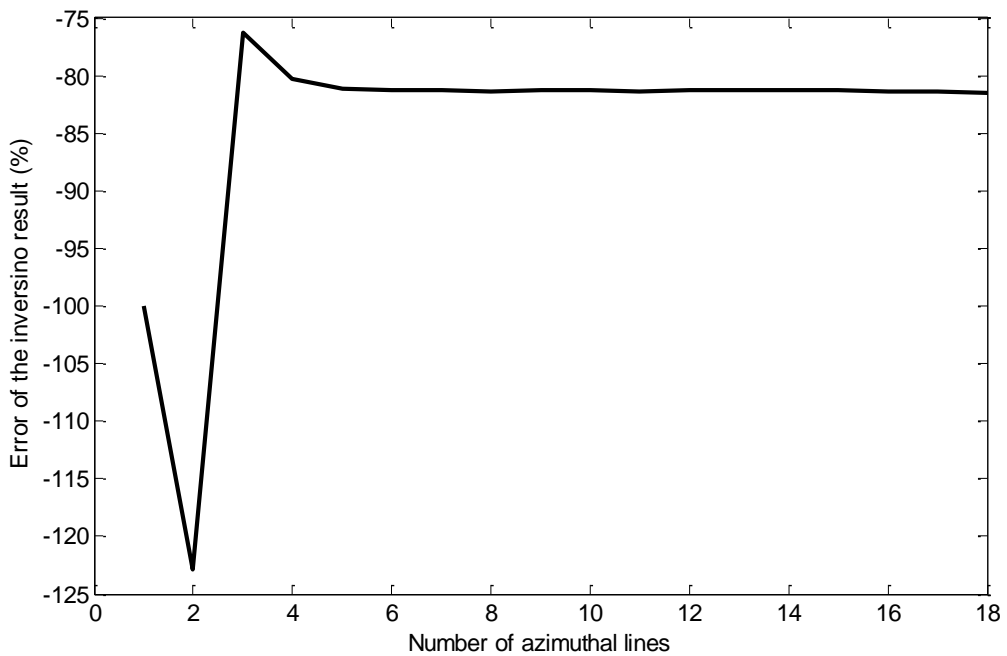


Figure 5.9. Error of inversion result for the fracture orientation. The lower HTI medium is rotated by  $110^\circ$ . S/N = 10.

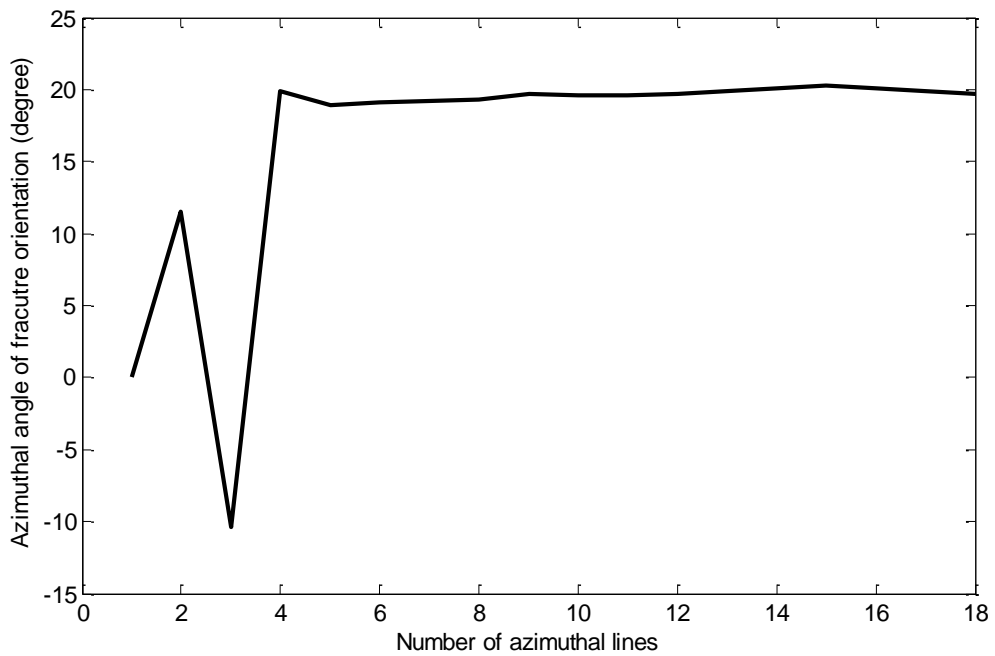


Figure 5.10. Inversion result for the fracture orientation. The lower HTI medium is rotated by 20°. S/N = 5.

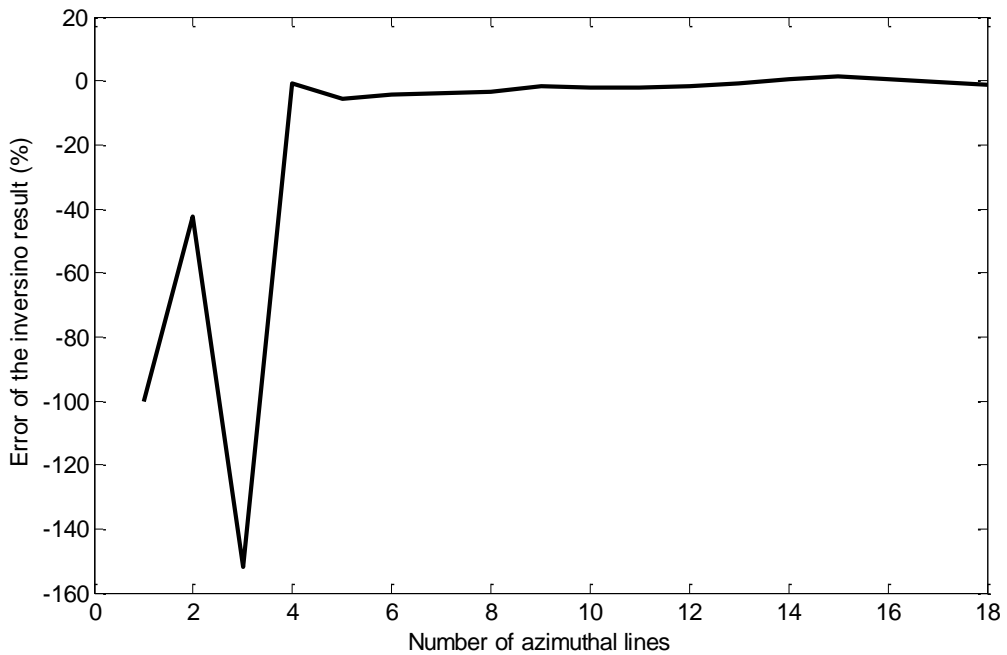


Figure 5.11. Error of inversion result for the fracture orientation. The lower HTI medium is rotated by 20°. S/N = 5.

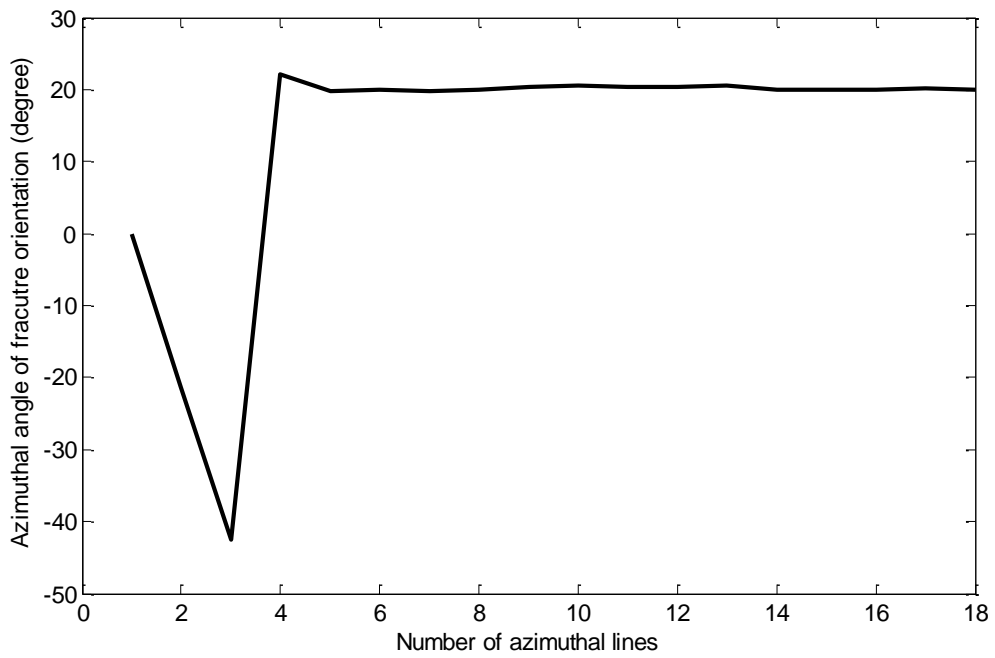


Figure 5.12. Inversion result for the fracture orientation. The lower HTI medium is rotated by  $110^\circ$ .  $S/N = 5$ .

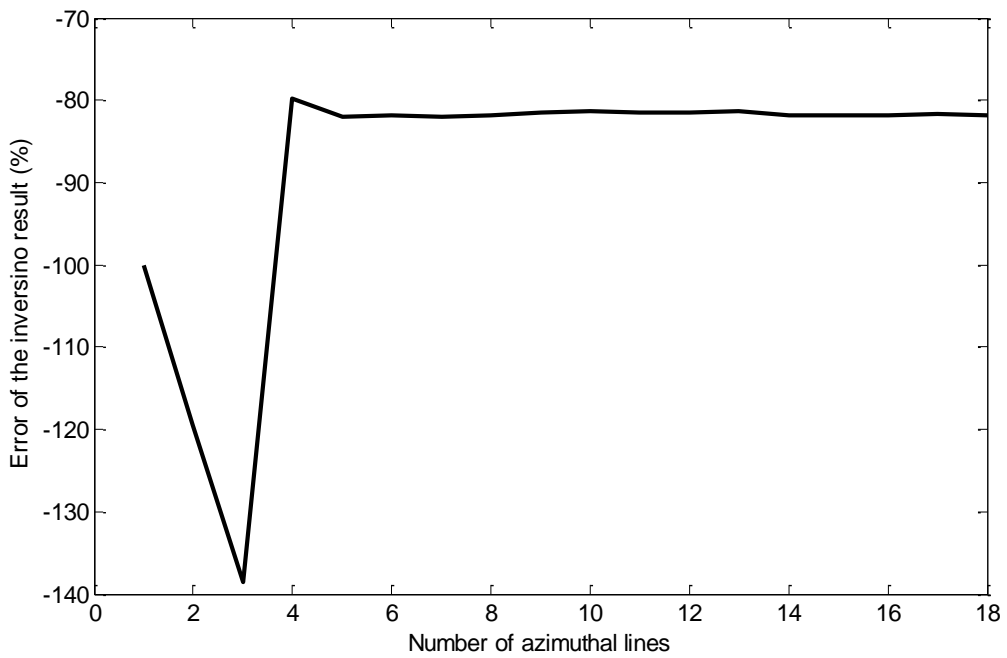


Figure 5.13. Error of inversion result for the fracture orientation. The lower HTI medium is rotated by  $110^\circ$ .  $S/N = 5$ .

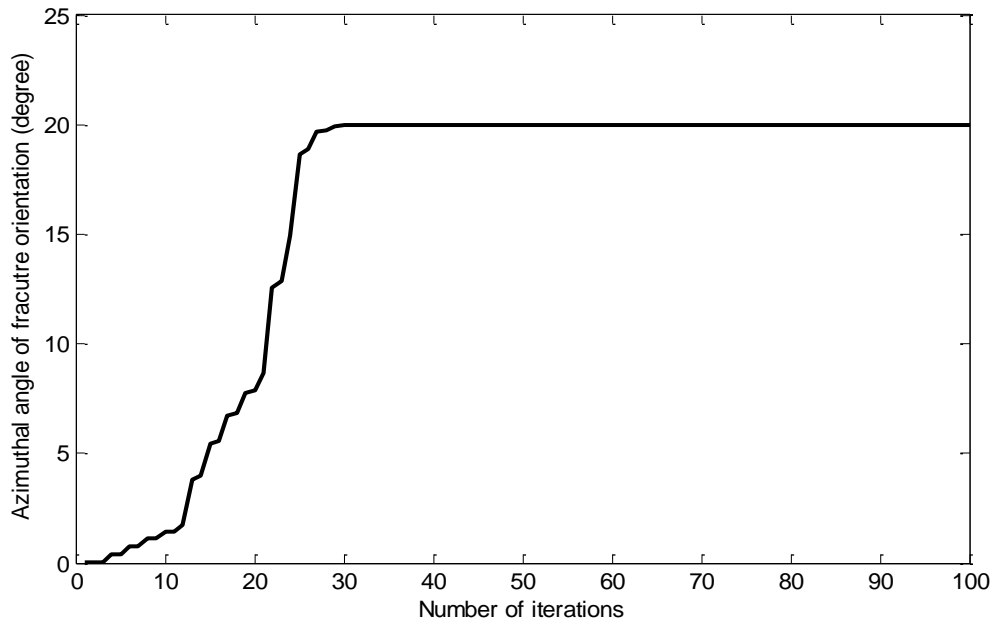


Figure 5.14. Inversion result for the fracture orientation based on the exact reflection coefficient inversion. The lower HTI medium is rotated by  $20^\circ$ .

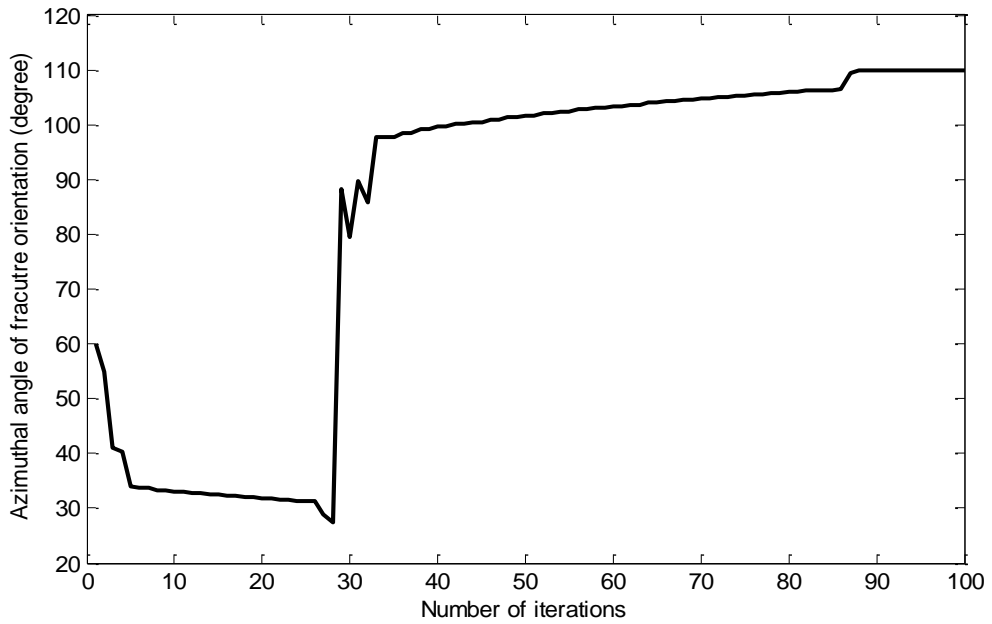


Figure 5.15. Inversion result for the fracture orientation based on the exact reflection coefficient inversion. The lower HTI medium is rotated by  $110^\circ$ .

Actually, there is no information about the sign of  $B^{ani}$  before inversion. Most practitioners of azimuthal anisotropy force  $B^{ani}$  to be positive and thus the estimated fracture orientation might have a  $90^\circ$  error, because  $B^{ani}$  could be either positive or negative. In addition, the polarity of the real seismic data also can cause an ambiguity in the inversion result. When the polarity is changed by  $180^\circ$ , which is equivalent to multiplying by -1 to the both sides of equation (5.21), most practitioners assume  $B^{ani}$  is always positive, thus the estimated fracture orientation will have a  $90^\circ$  error. Although the ambiguity always exists in the inversion of equation (5.21), this method still has some advantages. Because Rüger's approximation is a linear equation, there are few calculations in the inversion. It will help one save time and have a quick look at the data. Moreover, It is very stable, even for the lower quality data which have  $S/N = 5$  (See Figures 5.9 to 5.13).

In order to study this inversion problem, the GLI method, which is discussed in this chapter, and the method to calculate exact reflection coefficients are used to invert for the fracture orientation. Figure 5.14 shows the inversion result for a model with  $20^\circ$  rotation angle. The inverted angle is approaching  $20^\circ$  after 30 iterations and after that, it remains constant. Figure 5.15 shows the inversion result using the same method but with a different exact reflection coefficient model, which has a  $110^\circ$  orientation angle. After 35 iterations, the inverted angle is about  $110^\circ$  and has less than  $10^\circ$  error. It finally approaches  $110^\circ$  after 90 iterations. Comparing Figure 5.14 and Figure 5.15, it looks like that the problem of ambiguity of  $90^\circ$  is solved. Two models with  $90^\circ$  difference are used in these two figures and fracture orientations are recovered correctly, compared with

those results inverted by SVD method and Rüger's linear approximation. However, the GLI exact reflection coefficient inversion approach depends on the initial guess. If the initial guess is not close to the true solution, then a 90° ambiguity will happen again. Thus, more information is required to give an appropriate initial guess.

Although the method used in Figures 5.14 and 5.15 has advantage in recovering the fracture orientation, there are some limitations for using it. They are very sensitive to noise so that data with high S/N are required. Also the initial fracture orientation guess must be within the convergent region; otherwise, the result turns out to be incorrect. In short, the inversion results will be incorrect.

## 5.5 Inversion for anisotropy parameters

After obtaining the fracture orientation, Rüger's linear approximation in equation (3.15) can be written in terms of six parameters ( $\frac{\Delta\alpha}{\bar{\alpha}}$ ,  $\frac{\Delta\beta}{\bar{\beta}}$ ,  $\frac{\Delta\rho}{\bar{\rho}}$ ,  $\Delta\delta^{(v)}$ ,  $\Delta\varepsilon^{(v)}$ , and  $\Delta\gamma$ )

as

$$R_p^{HTI}(i, \phi) = A(i) \times \frac{\Delta\alpha}{\bar{\alpha}} + B(i) \times \frac{\Delta\beta}{\bar{\beta}} + C(i) \times \frac{\Delta\rho}{\bar{\rho}} + D(i, \phi) \times \Delta\delta^{(v)} + E(i, \phi) \times \Delta\varepsilon^{(v)} + F(i, \phi) \times \Delta\gamma, \quad (5.26)$$

where

$$\begin{aligned}
A &= \left( \frac{1}{2 \cos^2 i} \right), \\
B &= - \left( \frac{2\bar{\beta}}{\bar{\alpha}} \right)^2 \sin^2 i, \\
C &= \frac{1}{2} - 2 \left( \frac{\bar{\beta}}{\bar{\alpha}} \right)^2 \sin^2 i, \\
D &= \frac{1}{2} \cos^2 \phi \sin^2 i + \frac{1}{2} \sin^2 \phi \cos^2 \phi \sin^2 i \tan^2 i, \\
E &= \frac{1}{2} \cos^4 \phi \sin^2 i \tan^2 i, \\
F &= \left( \frac{2\bar{\beta}}{\bar{\alpha}} \right)^2 \cos^2 \phi \sin^2 i.
\end{aligned}$$

The method, discussed in Chapter 3, for exact reflection coefficient is used to calculate a numerical model which has 24 azimuthal lines, and the interval of each azimuthal line is 15°. Within each azimuthal line, there are 40 receivers with an incident-angle interval of 1°. Model parameters are the same as those used for inverting for fracture orientation except the rotation angle. In this numerical test, the fracture orientation is set to zero. The main goal of this inversion is to estimate the three anisotropy parameters ( $\delta^{(V)}$ ,  $\varepsilon^{(V)}$  and  $\gamma$ ), the most important of which is  $\gamma$ , because it is directly related to crack density in fracture-induced anisotropic media. The inversion for the three anisotropy parameters is obtained by using all azimuthal and incident angle data. The inversion error, calculated by comparing the inversion results and input model parameters, are shown in Figures 5.16 to 5.18. Favorable results are successfully achieved for the three anisotropy parameters, especially for  $\gamma$ .

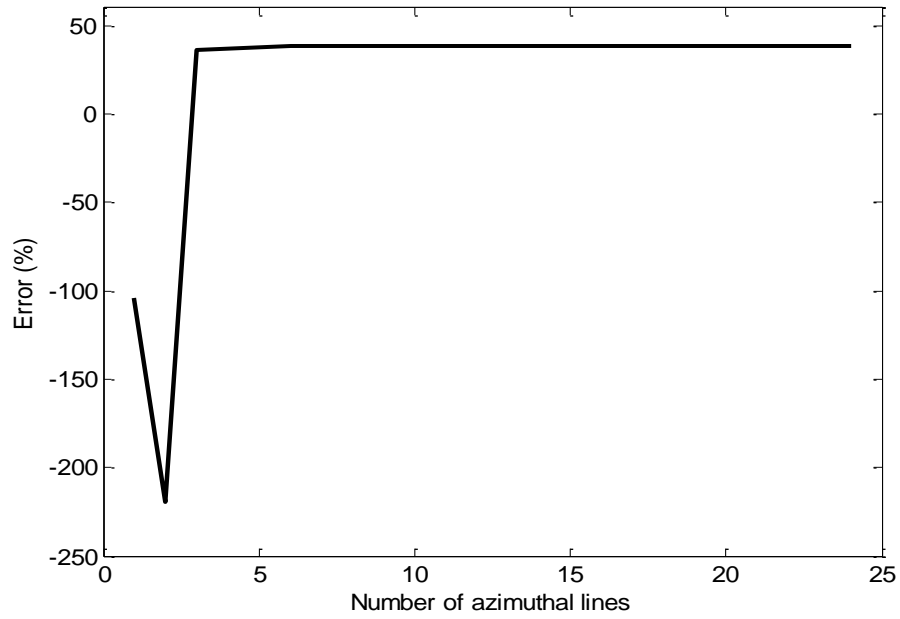


Figure 5.16. Inversion error for  $\delta^{(v)}$ .

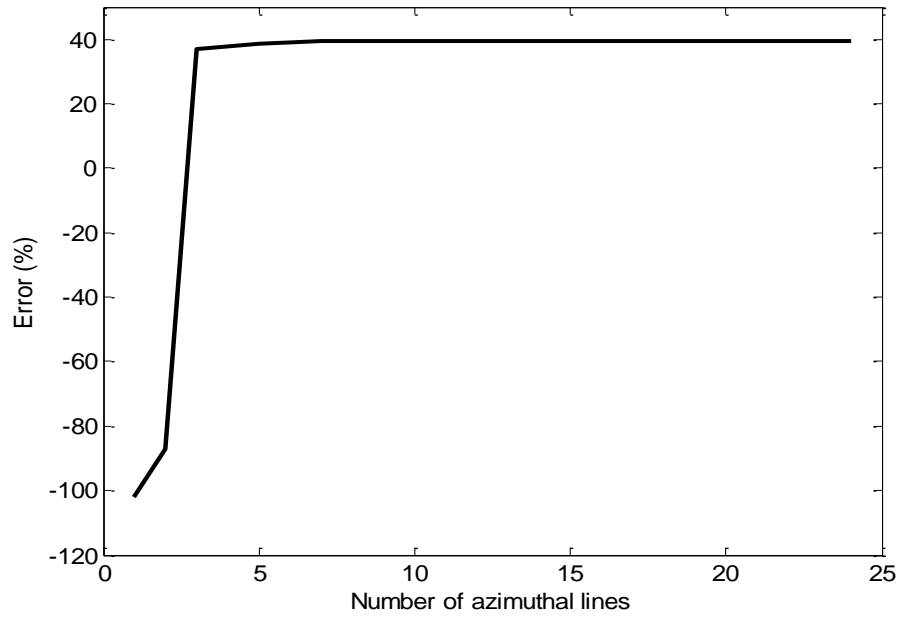


Figure 5.17. Inversion error for  $\epsilon^{(v)}$ .

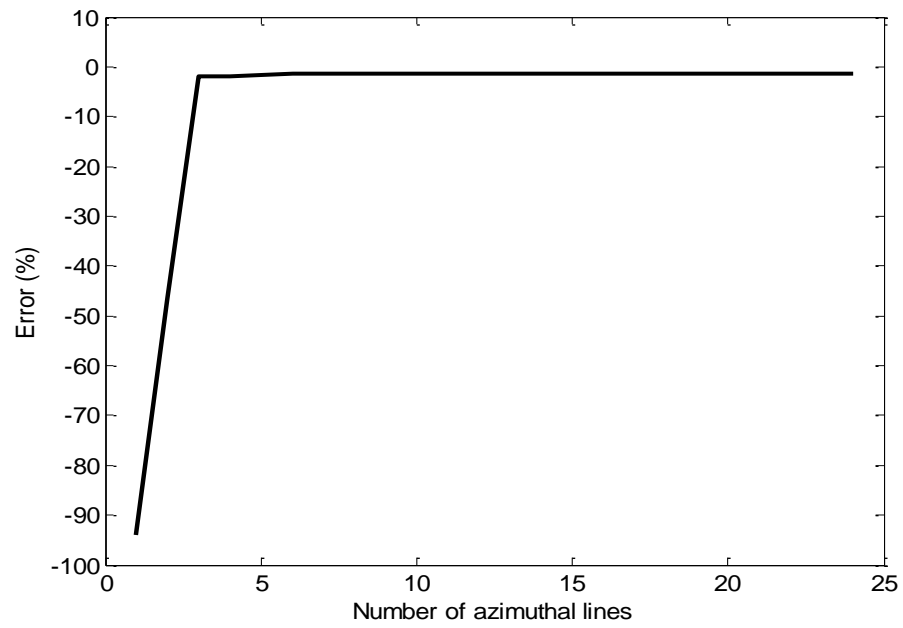


Figure 5.18. Inversion error for  $\gamma$ .

## 5.6 Error analysis

It is observed that the data S/N and some other input factors in the inversion process have noticeable effects on the inversion results for both fracture orientation and anisotropy parameters. How S/N affects the inversion results for fracture orientation are shown Figures 5.2 to 5.13. Now, I am going to discuss the effect of S/N on the inversion results for anisotropy parameters. In Figures 3.6 to 3.9, the reflection coefficients show no azimuthal variation at small incident angles. Only at large incident angles, there are noticeable azimuthal variations in the reflection coefficients. An obvious practical question is how large is the required maximum incident angle for accurate inversion results. Therefore, I am going to analyze how the selection of the maximum incident angle makes a difference in the inverted anisotropy parameters. My entire inversion can be divided into two steps. The first step is to invert for fracture orientation. And then, using the fracture orientation, obtained in first step, to invert for six parameters. I will discuss what the inverted anisotropy parameters will be if there are errors in the inversion for fracture orientation.

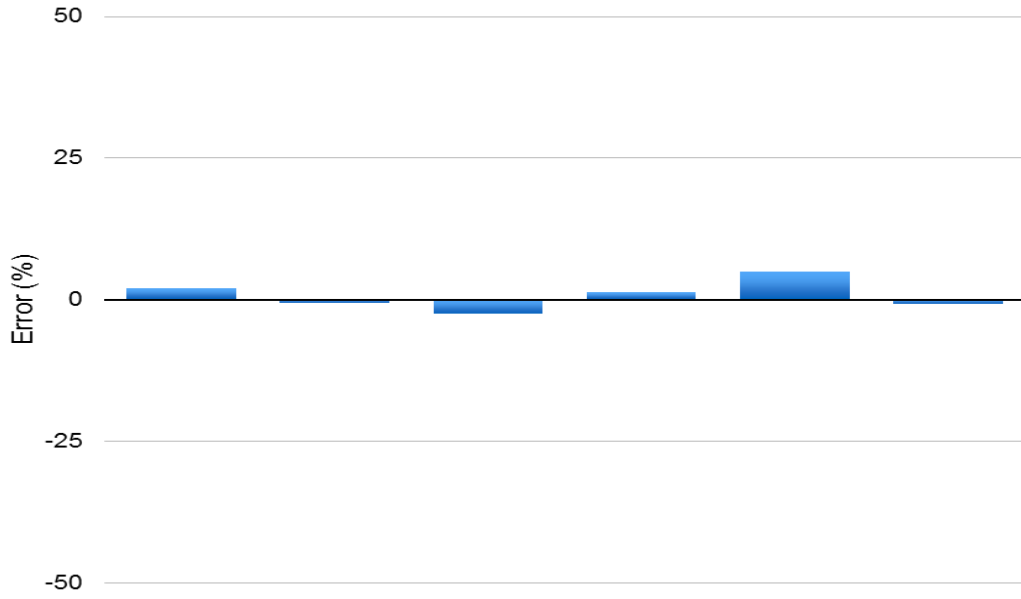


Figure 5.19. Inversion error results with  $S/N = 20$ .  $a, b, c, d, e,$  and  $f$  denote  $\frac{\Delta\alpha}{\bar{\alpha}}, \frac{\Delta\beta}{\bar{\beta}}, \frac{\Delta\rho}{\bar{\rho}}, \delta^{(v)}, \varepsilon^{(v)},$  and  $\gamma$ , respectively.

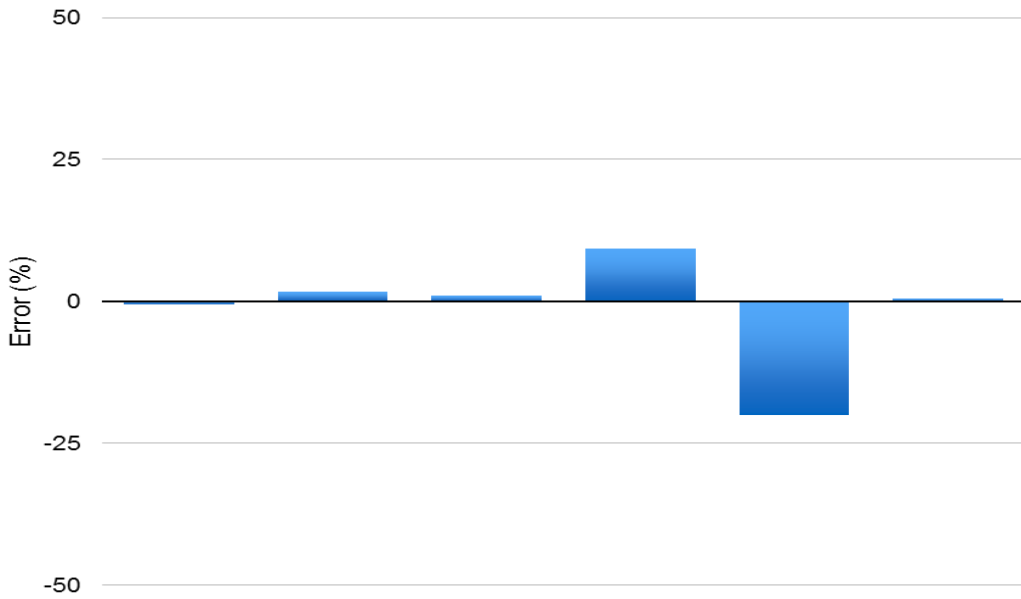


Figure 5.20. Inversion error results with  $S/N = 10$ .  $a, b, c, d, e,$  and  $f$  denote  $\frac{\Delta\alpha}{\bar{\alpha}}, \frac{\Delta\beta}{\bar{\beta}}, \frac{\Delta\rho}{\bar{\rho}}, \delta^{(v)}, \varepsilon^{(v)},$  and  $\gamma$ , respectively.

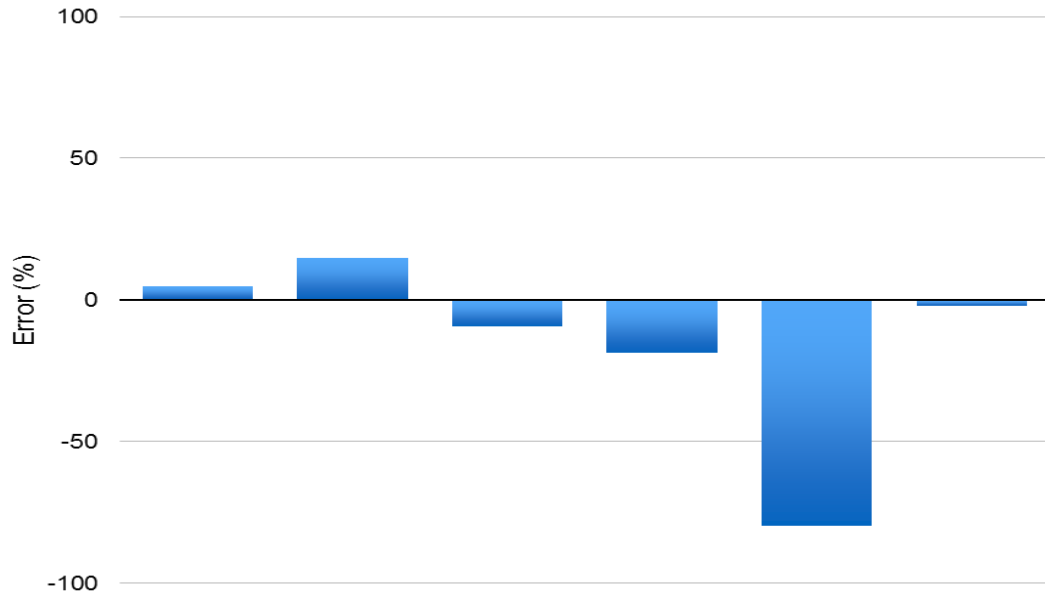


Figure 5.21. Inversion error results with  $S/N = 5$ .  $a, b, c, d, e$ , and  $f$  denote  $\frac{\Delta\alpha}{\bar{\alpha}}, \frac{\Delta\beta}{\bar{\beta}}, \frac{\Delta\rho}{\bar{\rho}}, \delta^{(v)}, \varepsilon^{(v)}$ , and  $\gamma$ , respectively.

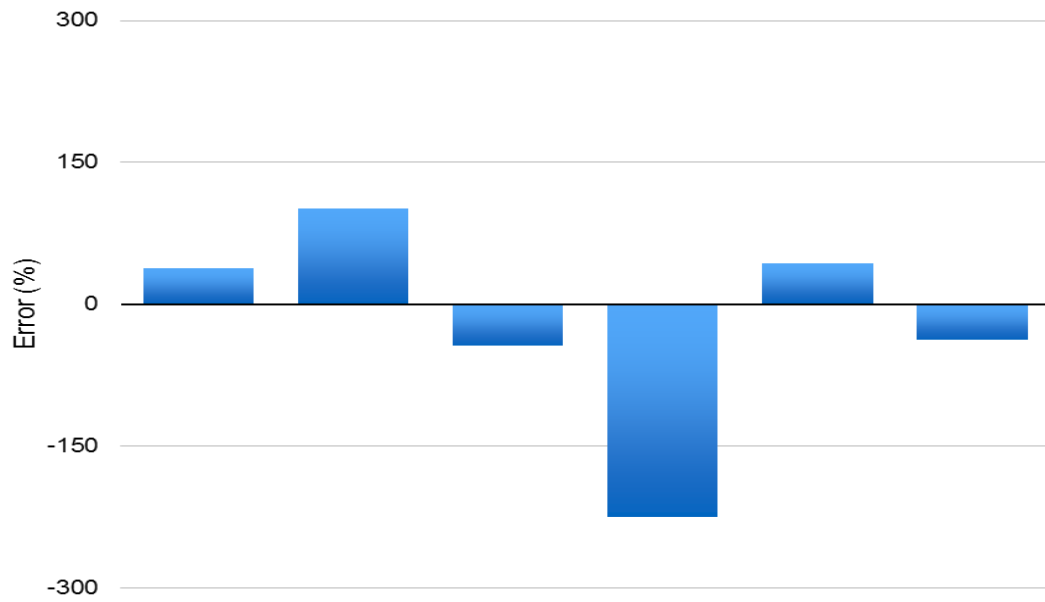


Figure 5.22. Inversion error results with  $S/N = 2$ .  $a, b, c, d, e$ , and  $f$  denote  $\frac{\Delta\alpha}{\bar{\alpha}}, \frac{\Delta\beta}{\bar{\beta}}, \frac{\Delta\rho}{\bar{\rho}}, \delta^{(v)}, \varepsilon^{(v)}$ , and  $\gamma$ , respectively.

Noise is always a problem for seismic inversion. It will affect the stability and the accuracy of the inversion results. The choice between stability and accuracy depends on the experience of the interpreter, as I will discuss how noise affects the accuracy of inversion. Figures 5.19 to 5.22 show four inversion results for the six parameters from six different models. These six models have the same model parameters:  $\frac{\Delta\alpha}{\bar{\alpha}} = 0.1$ ,  $\frac{\Delta Z}{\bar{Z}} = 0.2$ ,  $\frac{\Delta G}{\bar{G}} = 0.2$ ,  $\delta^{(V)} = -0.05$ ,  $\varepsilon^{(V)} = -0.05$ , and  $\gamma = 0.15$  but with different S/N. The reflection coefficients are obtained by Rüger's linear approximation for PP reflection coefficients using 18 azimuthal lines with  $10^\circ$  intervals and 40 receivers with  $1^\circ$  incident-angle interval in each azimuthal line. The S/N in Figures 4.19 to 4.22 are 20, 10, 5, and 2. The inversion is applied based on SVD and Rüger's approximation for PP reflection coefficients. It makes sense that the inversion errors increase when S/N decrease. In these figures, *a*, *b*, *c*, *d*, *e*, and *f* denote  $\frac{\Delta\alpha}{\bar{\alpha}}$ ,  $\frac{\Delta\beta}{\bar{\beta}}$ ,  $\frac{\Delta\rho}{\bar{\rho}}$ ,  $\delta^{(V)}$ ,  $\varepsilon^{(V)}$ , and  $\gamma$ , respectively. The maximum error in Figure 5.22, which has signal noise ratio of 2, is -225% for  $\varepsilon^{(V)}$ . However, the parameter  $\gamma$ , which directly relates to crack density, is of most interest. Fortunately, the  $\gamma$  error is tolerable even in the model with S/N = 2 in Figure 5.22. Thus, when  $\gamma$  is the only parameter that we want to recover from seismic data, the SVD method using Rüger's linear approximation for PP reflection coefficients is reliable. Even in Figure 5.22,  $\gamma$  has an acceptable error of -38% which is acceptable. The inversion errors for variations in P-wave velocity, S-wave velocity, and density, appear to be less than the inversion errors for the three anisotropy parameters. When S/N is larger than 10,

which are shown in Figures 5.19 and 5.20, the inversion errors are acceptable for most interpretations.

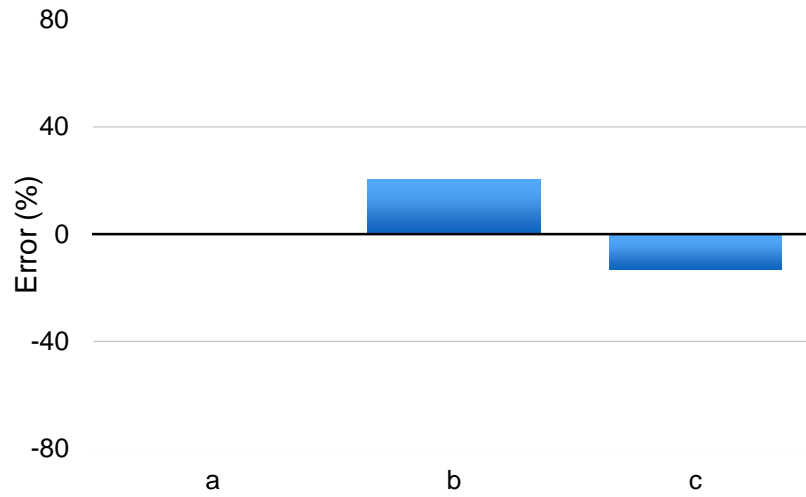


Figure 5.23. Inversion errors from data with incident angles from  $0^\circ$  to  $10^\circ$ .  $a = \delta^{(V)}$ ,  $b = \varepsilon^{(V)}$ , and  $c = \gamma$ .

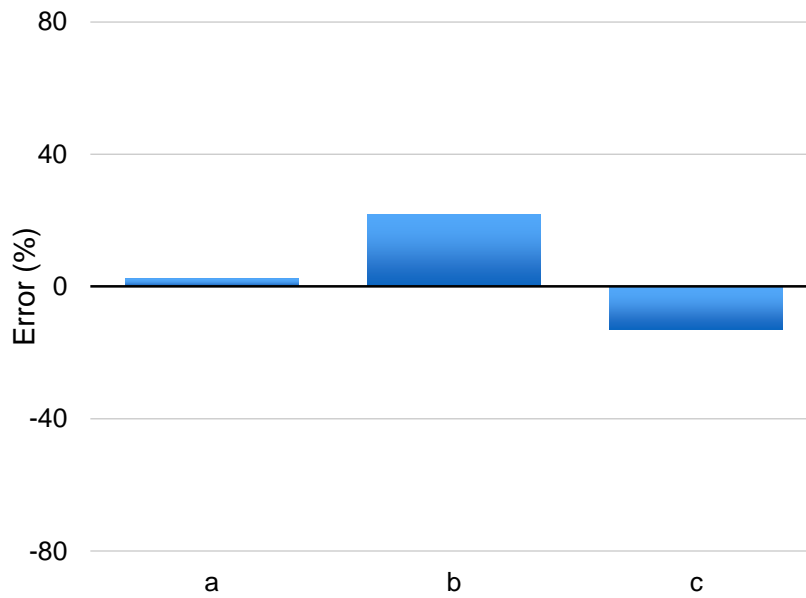


Figure 5.24. Inversion errors from data with incident angles from  $0^\circ$  to  $15^\circ$ .  $a = \delta^{(V)}$ ,  $b = \varepsilon^{(V)}$ , and  $c = \gamma$ .

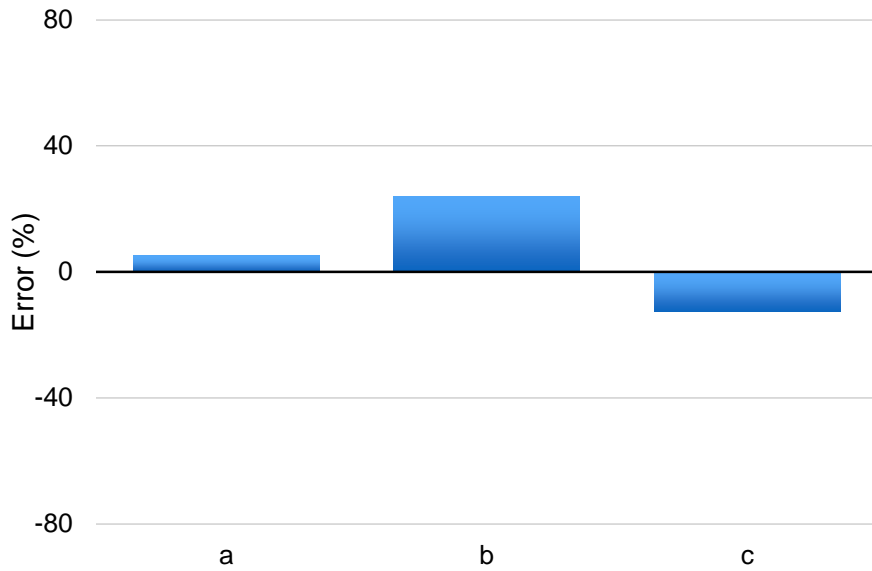


Figure 5.25. Inversion errors from data with incident angles from  $0^\circ$  to  $20^\circ$ .  $a = \delta^{(V)}$ ,  $b = \varepsilon^{(V)}$ , and  $c = \gamma$ .

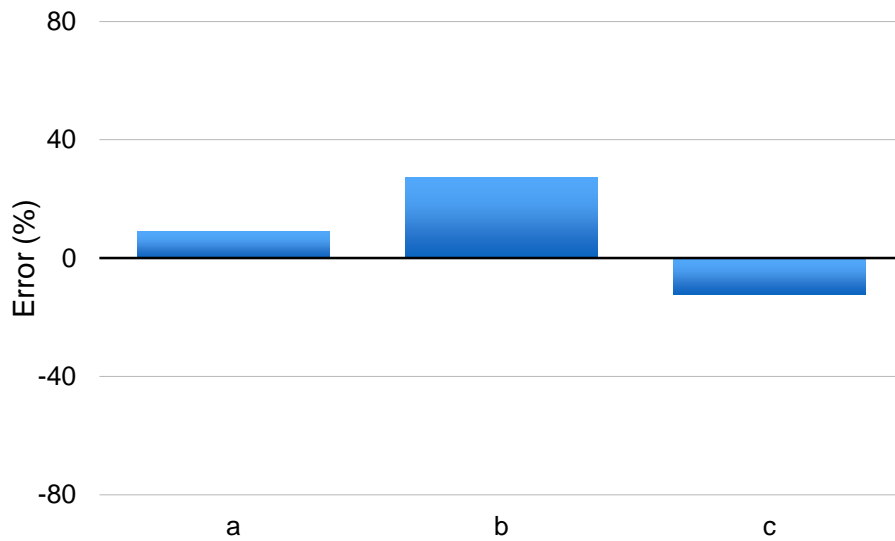


Figure 5.26. Inversion errors from data with incident angles from  $0^\circ$  to  $25^\circ$ .  $a = \delta^{(V)}$ ,  $b = \varepsilon^{(V)}$ , and  $c = \gamma$ .

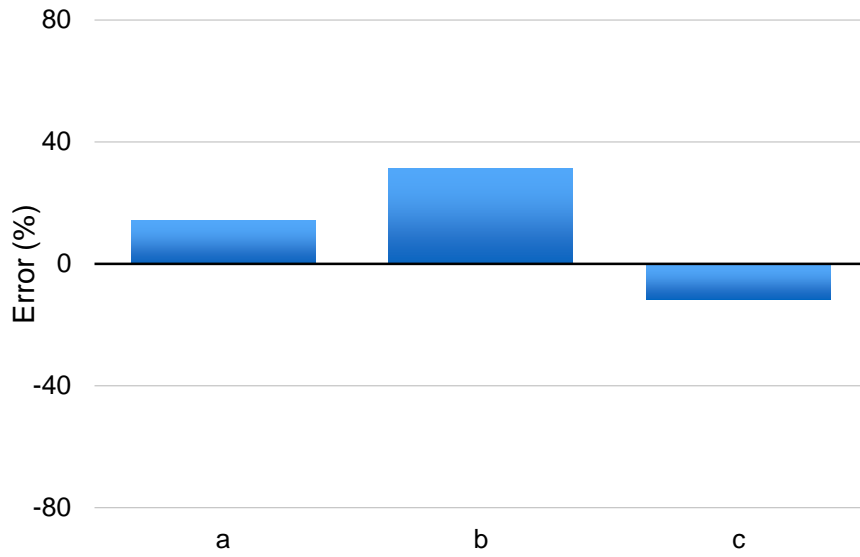


Figure 5.27. Inversion errors from data with incident angles from  $0^\circ$  to  $30^\circ$ .  $a = \delta^{(V)}$ ,  $b = \varepsilon^{(V)}$ , and  $c = \gamma$ .

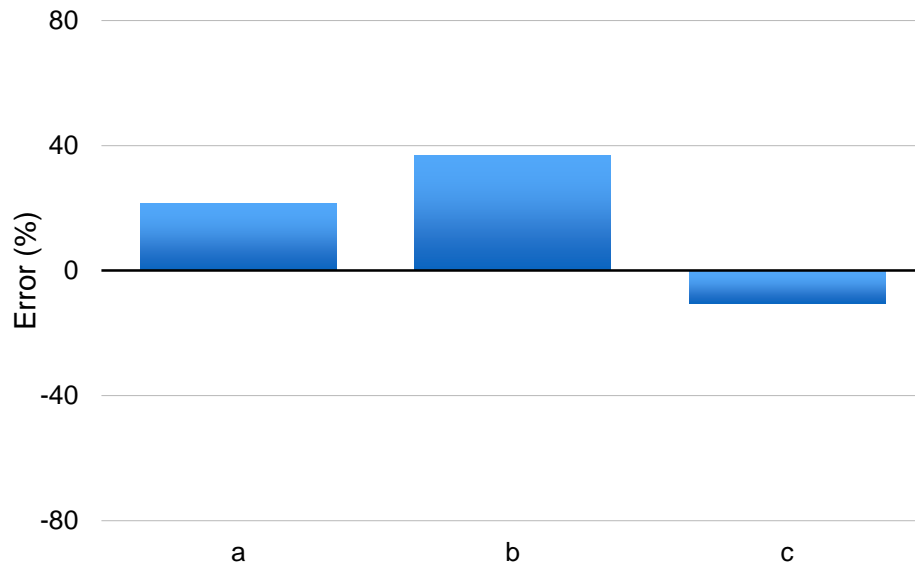


Figure 5.28. Inversion errors from data with incident angles from  $0^\circ$  to  $35^\circ$ .  $a = \delta^{(V)}$ ,  $b = \varepsilon^{(V)}$ , and  $c = \gamma$ .

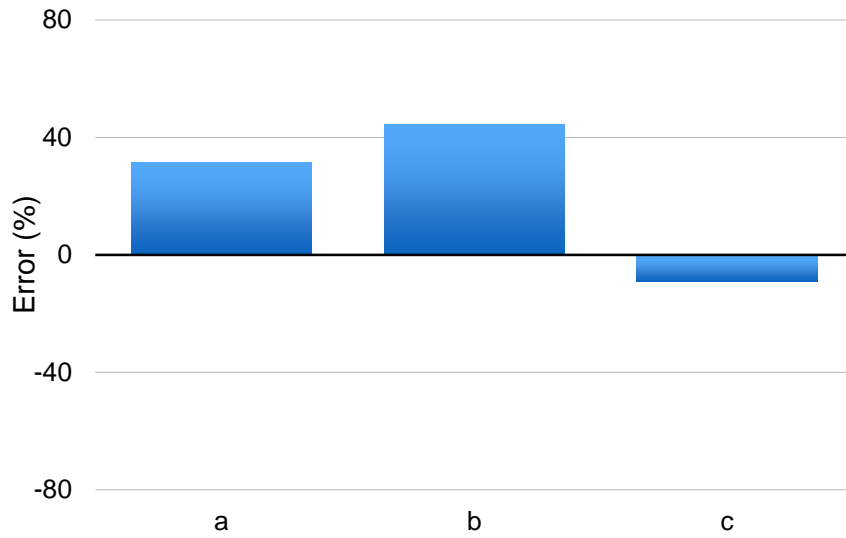


Figure 5.29. Inversion errors from data with incident angles from  $0^\circ$  to  $40^\circ$ .  $a = \delta^{(V)}$ ,  $b = \varepsilon^{(V)}$ , and  $c = \gamma$ .

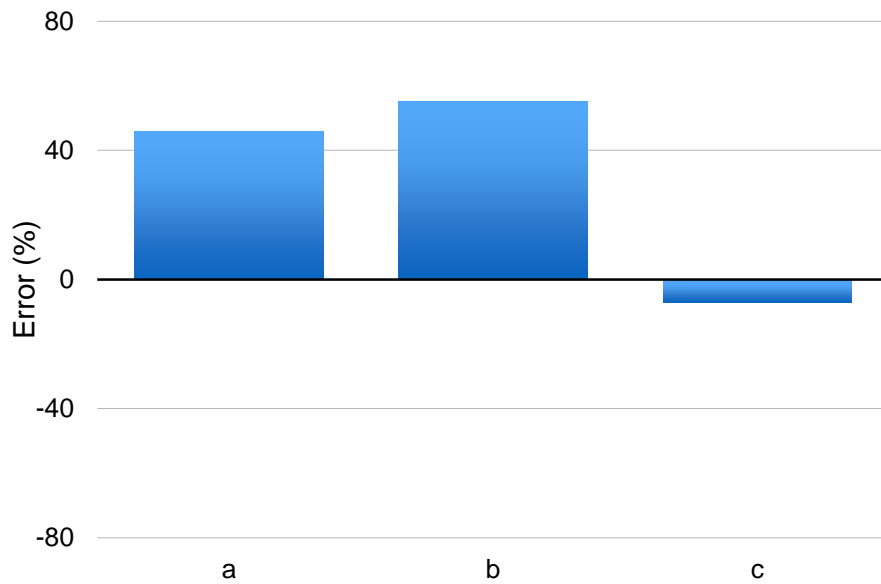


Figure 5.30. Inversion errors from data with incident angles from  $0^\circ$  to  $45^\circ$ .  $a = \delta^{(V)}$ ,  $b = \varepsilon^{(V)}$ , and  $c = \gamma$ .

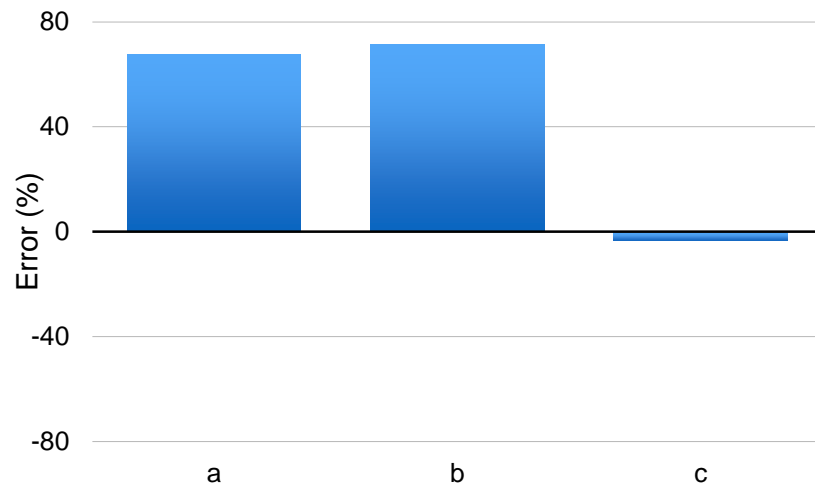


Figure 5.31. Inversion errors from data with incident angles from  $0^\circ$  to  $50^\circ$ .  $a = \delta^{(v)}$ ,  $b = \varepsilon^{(v)}$ , and  $c = \gamma$ .

Figures 5.23 to 5.31 show the inversion errors for three parameters ( $\delta^{(v)}$ ,  $\varepsilon^{(v)}$ , and  $\gamma$ ), which are denoted by  $a$ ,  $b$ , and  $c$ , with different maximum incident angles. And the model parameters are the same as those for Figures 5.19 to 5.22. The input exact reflection coefficients are obtained by the method introduced by Chattopadhyay (2004). Different maximum incident angles will provide different errors for the anisotropy parameters. From the small maximum incident angle to large maximum incident angle, the inversion errors for  $\delta^{(v)}$  and  $\varepsilon^{(v)}$  are increasing. The reason for this phenomenon can be found in Chapter 3. In Chapter 3, I compared the exact reflection coefficients and its approximations, calculated by R uger's method, for different models (See Table 3.1). The difference between the exact and approximated reflection coefficients as a function of incident angle are shown in Figures 3.7 and 3.8, where only the anisotropic parameters  $\delta^{(v)}$  and  $\varepsilon^{(v)}$  are non-zero. R uger's linear approximation deviates from the exact reflection coefficients as the incident angle increases. Unfortunately, R uger's linear approximation cannot estimate the exact reflection coefficient accurately at large incident angles. Consequently, inversion errors for  $\delta^{(v)}$  and  $\varepsilon^{(v)}$ , shown in Figures 5.23 to 5.31, increase when the maximum incident angle increases. But  $\gamma$  is better estimated at large incident angles than  $\delta^{(v)}$  and  $\varepsilon^{(v)}$ . In Figure 3.6, the approximation is very close to the exact reflection coefficients, when only  $\gamma$  is non-zero and other two anisotropy parameters are zero, which means R uger's approximation is less sensitive to the maximum incident angles in this case. The inversion errors for  $\gamma$  in Figures 5.23 to 5.31 are very small and they are decreasing while the maximum incident is increasing. Thus, we can make a conclusion that the choice of the maximum incident angle will definitely

affect the inversion result. However, the value of the inverted  $\gamma$ , which is of most interest, will not change significantly with maximum incident angles.

In this chapter, we first inverted the fracture orientation and then the fracture orientation was used as an input to invert for the other six parameters ( $\frac{\Delta\alpha}{\bar{\alpha}}, \frac{\Delta\beta}{\bar{\beta}}, \frac{\Delta\rho}{\bar{\rho}}, \delta^{(v)}, \varepsilon^{(v)}$ , and  $\gamma$ ). And the error in first step will propagate to the second step, so that the estimations of six parameters are less accurate. Rüger's linear approximation is used for both forward modeling and inversion. In the next modeling examples, the model parameters and geometry are the same as those used in Figures 5.23 to 5.31. And  $a$ ,  $b$ , and  $c$ , in Figures 5.33 to 5.35, denote  $\delta^{(v)}, \varepsilon^{(v)}$ , and  $\gamma$ . Figure 5.32 shows that the difference between the reflection coefficients with a rotation angle of  $0^\circ$  and  $5^\circ$ . The difference is less than 5%. The difference is small but it increases with increasing incident angle. As inferred earlier, this difference is periodic with azimuth. Figure 5.33 shows the inversion error for the three anisotropy parameters, if there is a  $5^\circ$  error in the first step. The inversion results are very good and the errors are small, less than 2%. When the error in the first step becomes  $10^\circ$ , the reflection coefficient difference, shown in Figure 5.34, is less than 10%. Figure 5.35 shows the anisotropy parameter inversion is very encouraging, as even if there is  $10^\circ$  error in estimating the fracture orientation, the inversion results for the three anisotropy parameters have a small error. This phenomenon allows for some errors in the inversion of the fracture orientation.

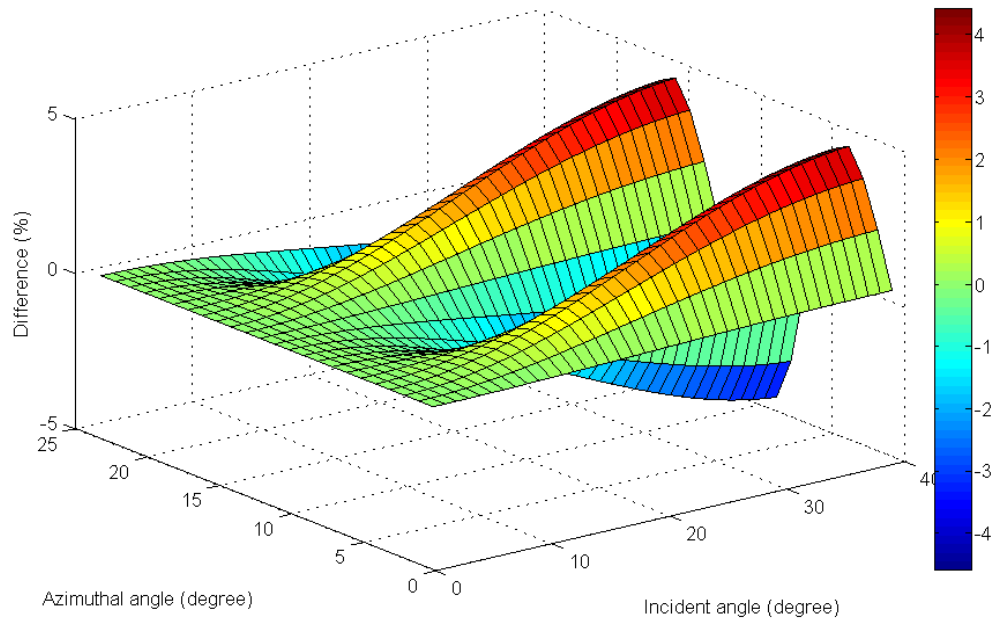


Figure 5.32. Difference between the reflection coefficient for rotation angles of 0° and 5°.

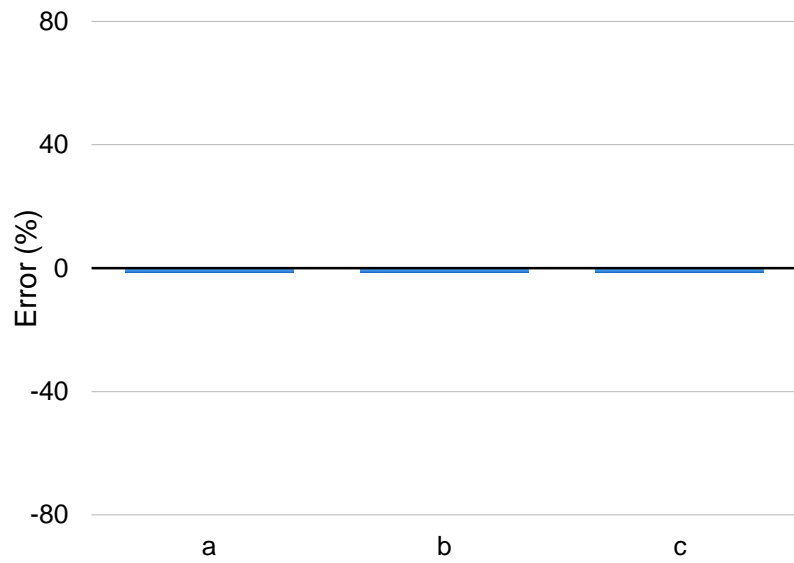


Figure 5.33. Inversion errors for anisotropic parameters for an error of  $5^\circ$  in the estimated fracture orientation.  $a = \delta^{(v)}$ ,  $b = \varepsilon^{(v)}$ , and  $c = \gamma$ .

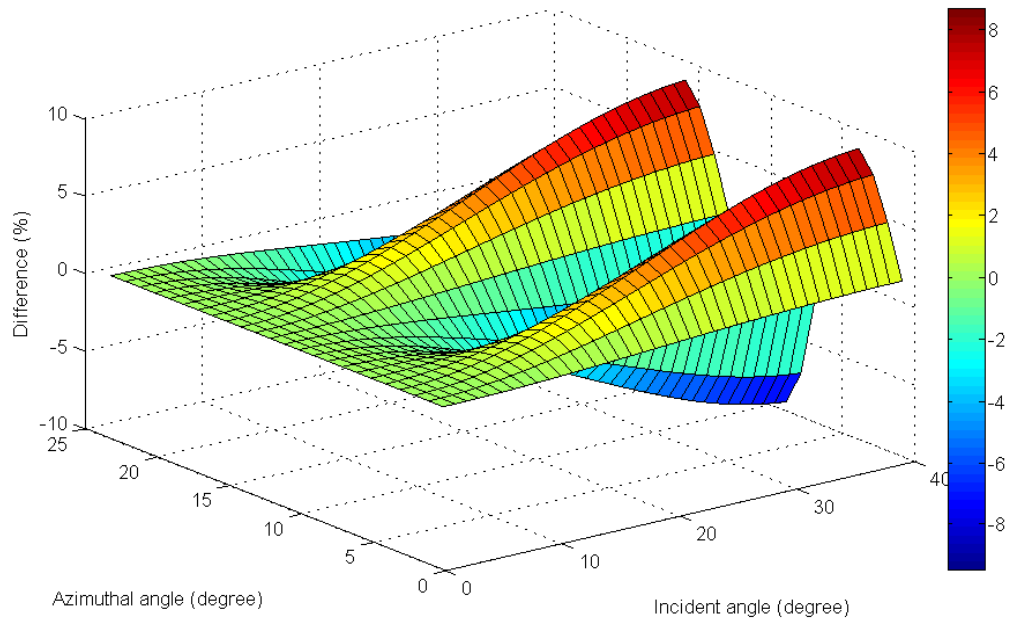


Figure 5.34. Difference between the reflection coefficient for rotation angles of  $0^\circ$  and  $10^\circ$ .

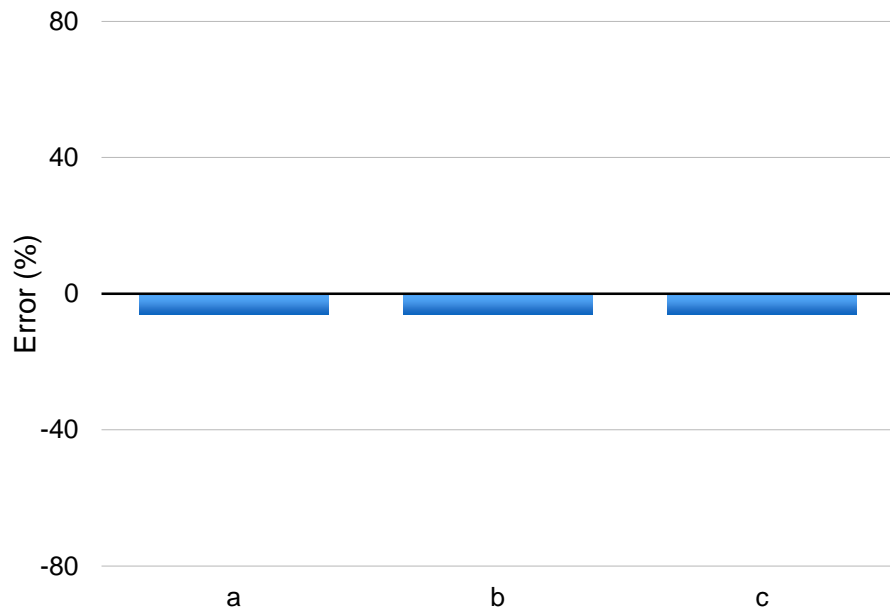


Figure 5.35. Inversion errors for anisotropic parameters for an error of  $10^\circ$  in the estimated fracture orientation.  $a = \delta^{(V)}$ ,  $b = \varepsilon^{(V)}$ , and  $c = \gamma$ .

## 5.7 Conclusion

In this chapter, the inversion for fracture orientation and the six parameters ( $\frac{\Delta\alpha}{\bar{\alpha}}, \frac{\Delta\beta}{\bar{\beta}}, \frac{\Delta\rho}{\bar{\rho}}, \delta^{(v)}, \varepsilon^{(v)}$ , and  $\gamma$ ) in the anisotropic reflection coefficient equation are applied by two different methods. In the first method, SVD and Ruger's linear approximation for P-wave reflection coefficients are used. In the second method, inversions using GLI and exact reflection coefficients are compared to the first method. The fracture orientation estimated by the first method may have a 90° ambiguity. With an appropriate initial guess, the second method can overcome the ambiguity problem. But the first method is fast and the calculations are efficient. The second method requires more calculations and it is very sensitive to noise. When the first method inverts for anisotropy parameters from the exact reflection coefficients, the error for  $\gamma$  results is acceptable. This is directly related to crack density. Different S/N values are used to test the reliability of the first method. The inversion for the six parameters is more sensitive than the inversion for fracture orientation. But the results can still provide useful information about the value of  $\gamma$  even with low S/N.

The three anisotropy parameters ( $\delta^{(v)}, \varepsilon^{(v)}$ , and  $\gamma$ ) have different sensitivities to the maximum incident angle according to Figure 3.6 to 3.8 in Chapter 3. When the maximum incident angle increases, the inversion errors for  $\delta^{(v)}$  and  $\varepsilon^{(v)}$  increase concurrently. However, the inversion result for  $\gamma$  is more accurate at large incident angles. Thus, the choice of the maximum incident angle needs to be carefully considered before inversion. And the error propagation happens, because there are two steps in the

inversion. The fracture orientation is estimated before inverting for the three anisotropy parameters. But it is encouraging that the error in the estimation of the fracture orientation will not problematize the results of three anisotropy parameters, even if the error increases to  $10^\circ$ .

## CHAPTER 6

### CONCLUSION

The main goal of this thesis is to determine whether information, including the anisotropy and direction of the symmetry plane of a fractured medium, can be extracted from an amplitude analysis. Numerical seismic modeling is used in this study. The first and second Green-Christoffel equations provide a solution to obtain phase and group velocities in arbitrary anisotropic media. Two approaches (Chattopadhyay, 2004; Schoenberg and Protazio, 1992) are introduced to calculate the exact reflection coefficients in arbitrary anisotropic media. However, both of these two approaches are complicated and time-consuming. In order to simplify the process, Rüger (1997) introduces a linear equation for reflection coefficients approximation for HTI media. The linear approximation can accurately estimate the exact reflection coefficients at small incident angles. When the azimuth observation lines are closer to the isotropic plane, the estimation is more accurate. Shuey (1985) suggests using the average angle instead of incident angle in the linear equation for the reflection coefficients approximation in isotropic media. The test shows that the choice of average angle and incident angle does not make an obvious difference in the reflection coefficients approximation in HTI media. In other words, the choice of average angle and incident angle will not significantly affect the result in HTI media.

It is convenient to use elastic compliance to formulate the equivalent anisotropic medium problem for seismic modeling of sets of aligned fractures embedded in host

medium, when the seismic wavelengths are much larger than the fracture size and spacing. The linear slip theory, introduced by Schoenberg (1980, 1983), can be used to relate the stress and strain by fracture compliance. For rotationally invariant fractures, two weaknesses, normal ( $\Delta N$ ) and tangential ( $\Delta T$ ) weaknesses, are required to form the compliance matrix. By comparing the linear slip theory and Hudson's method (1980, 1981), the normal and tangential weaknesses can be expressed in terms of the crack density and the ratio of P-wave and S-wave velocities. TI (LSD), which is only required four independent parameters, is used to specify a set of vertical, aligned, rotationally invariant fractures. Even though some assumptions of the effective medium theory are violated, this effective medium theory remains accurate. The information that can be obtained from seismic data is only the fracture orientation and a rough estimate of crack density. The estimation of shape, size, and distribution of the fracture is beyond the capability of long wavelength seismic data.

Linear (SVD) and non-linear (GLI) inversions are used to invert for fracture orientation. However, the  $90^\circ$  ambiguity, which is an intrinsic mathematic problem, always exists in the inversion result. By appropriately choosing the initial guess for the non-linear inversion, this ambiguity may be solved. And three anisotropy parameters ( $\delta^{(v)}$ ,  $\varepsilon^{(v)}$ , and  $\gamma$ ) are inverted by linear inversion. The inversion error for  $\gamma$ , which is directly related to crack density, is acceptable. Factors, which are S/N ratio, maximum incident angle, and error propagation, are analyzed for the inversion results. The inversion error increases when S/N ratio decreases. By comparing the inversion errors for  $\delta^{(v)}$  and  $\varepsilon^{(v)}$  with the inversion error for  $\gamma$ , which is of most interest,  $\gamma$  is less sensitive

to S/N ratio. The choice of maximum incident angle for the inversion will affect the accuracy of inversion results for different anisotropy parameters. Using large maximum incident angle for the inversion may be better for  $\gamma$ , but worse for  $\delta^{(v)}$  and  $\varepsilon^{(v)}$ . Error propagation from inverted fracture orientation to the inverted anisotropy parameters is non-significant. Even though the inverted fracture orientation has a  $10^\circ$  error, the inversion errors for three anisotropy parameters are less than 10%.

## APPENDIX A

Stiffness matrix of illite (Gpa):

179.9	39.9	14.5	0	0	0
39.9	179.9	14.5	0	0	0
14.5	14.5	55	0	0	0
0	0	0	11.7	0	0
0	0	0	0	11.7	0
0	0	0	0	0	70

Density: 2.79 g/cm<sup>3</sup>.

## APPENDIX B

Isotropic medium (Gpa):

13.81378	3.872866	3.872866	0	0	0
3.872866	13.81378	3.872866	0	0	0
3.872866	3.872866	13.81378	0	0	0
0	0	0	4.970455	0	0
0	0	0	0	4.970455	0
0	0	0	0	0	4.970455

Density: 2.7 g/cm<sup>3</sup>.

VTI medium (Gpa):

16.875	4.725	3.632606	0	0	0
4.725	16.875	3.632606	0	0	0
3.632606	3.632606	15.1875	0	0	0
0	0	0	4.673077	0	0
0	0	0	0	4.673077	0
0	0	0	0	0	6.075

Density: 2.7 g/cm<sup>3</sup>.

HTI medium (Gpa):

15.1875	6.653714	6.653714	0	0	0
6.653714	16.875	4.725	0	0	0
6.653714	4.725	16.875	0	0	0
0	0	0	6.075	0	0
0	0	0	0	4.673077	0
0	0	0	0	0	4.673077

Density: 2.7 g/cm<sup>3</sup>.

## REFERENCE

- Aguilera, R., 2003, Geologic and engineering aspects of naturally fractured reservoirs: Canadian Society of Exploration Geophysicists Recorder (February), 44-49.
- Aki, K., and Richards, P.G., 1980, Quantitative Seismology. San Francisco: W. H. Freeman and Company.
- Backus, G. E., 1962, Long-wave elastic anisotropy produced by horizontal layering: Journal of Geophysical Research, **67**, 4427-4440.
- Bakulin, A., and Molotkov, L., 1998, Effective Models of Fractured and Porous Media: St. Petersburg Univ. Press (in Russian).
- Bakulin, A., Grechka, V., and Tsvankin, I., 2000, Estimation of fracture parameters from reflection seismic data. Part I: HTI model due to a single fracture set: Geophysics, **65**, 1788-1802.
- Banik, N., 1987, An effective anisotropy parameter in transversely isotropic media: Geophysics, **52**, 1654-1664.
- Barton, N., 2006, Rock Quality, Seismic Velocity, Attenuation and Anisotropy. London: Taylor & Francis Group.
- Berryman, J. G., 2008, Exact seismic velocities for transversely isotropic media and extended Thomsen formulas for stronger anisotropies. Geophysics, **73**, D1-D10.
- Blangy, J. P., 1994, AVO in transversely isotropic media-an overview: Geophysics, **59**, 775-781.
- Bruner, W., 1976, Comment on "Seismic velocities in dry and saturated cracked solids": Journal of Geophysical Research, **81**, 2573-2576.
- Budiansky, B., and O'Connell, R., 1976, Elastic moduli of a cracked solid: International Journal. Solids Struct., **12**, 81-97.
- Chattopadhyay, A., 2004, Wave reflection and refraction in triclinic crystalline media: Archive of Applied Mechanics, **73**, 568-579.
- Chen, H., 2000, Anisotropic Effects Upon Amplitude-vs-Offset Response in Realistic Earth Models: Ph.D dissertation, University of Oklahoma.
- Chen, H., Brown, R. L., and Castagna, J. P., 2005, AVO for one and two fracture set models: Geophysics, **70**, C1-C5.
- Cooke, D. A., and Schneider, W.A., 1983, Generalized linear inversion of reflection seismic data: Geophysics, **48**, 665-676.
- Daley, P. F., and Hron, F., 1977, Reflection and transmission coefficients for transversely isotropic media: Bulletin of the Seismological Society of America, **67**, No. 3, 661-675.
- Daley, P. F., and Hron, F., 1979, Reflection and transmission coefficients for seismic waves in ellipsoidally anisotropic media: Geophysics, **44**, 27-38.
- Far, M. E., 2011, Seismic Characterization of Naturally Fractured Reservoirs: Ph.D dissertation, University of Houston.
- Fedorov, F. I., 1968, Theory of Elastic Waves in Crystals. New York: Plenum Press.
- Graebner, M., 1992, Plane-wave reflection and transmission coefficients for a transversely isotropic solid: Geophysics, **57**, 1512-1519.
- Grechka, V., and Kachanov, M., 2006, Effective elasticity of fractured rocks: A snapshot of the work in progress: Geophysics, **71**, W45-W58.
- Helbig, K., 1994, Foundations of anisotropy for exploration seismics: Handbook of geophysical exploration, I: Seismic exploration. Oxford: Pergamon Press.
- Henye, F., and Pomphrey, N., 1982, Self-consistent elastic moduli of a cracked solid: Geophys. Res. Lett., **9**, 903-906.

- Hoening, A., 1979, Elastic moduli of a non-randomly cracked body: *International Journal. Solids Struct.*, **15**, 137-154.
- Hsu, C.-J., and M. Schoenberg, 1993, Elastic waves through a simulated fractured medium: *Geophysics*, **58**, 964-977.
- Hudson, J. A., 1980, Overall properties of a cracked solid: *Math. Proc. Camb. Phil. Soc.*, **88**, 371-384.
- Hudson, J. A., 1981, Wave speeds and attenuation of elastic waves in material containing cracks: *Geophys. J. Roy. Astr. Soc.*, **64**, 133-150.
- Hudson, J. A., 1986, A higher order approximation to the wave propagation constants for a cracked solid: *Geophys. J. Roy. Astr. Soc.*, **87**, 265-274.
- Jin, S., Beydoun, W., and Madariaga, R., 1993, A stable elastic inversion for marine data: 63<sup>rd</sup> Ann. Internat. Mtg., Soc. Expl. Geophys., Expanded Abstracts, 665-668.
- Jin, S., Cambois, G., and Vuillermoz, C., 2002, Shear-wave velocity and density estimation from PS-wave AVO analysis: Application to an OBS database from the North Sea: *Geophysics*, **65**, 1446-1454.
- Kachanov, M., 1992, Effective elastic properties of cracked solids: critical review of some basic concepts: *Appl. Mech. Rev.*, **45**, 304-335.
- Lay, D. C., 1997, *Linear Algebra and its Applications*. Boston: Addison-Wesley.
- Leary, P. C., Crampin, S., and McEvelly, T. V., 1990, Seismic fracture anisotropy in the Earth's crust: An overview: *Journal of Geophysical Research*, **95**, 11,105-11,114.
- Liu, E., Hudson, J. A., and Pointer, T., 2000, Equivalent medium representation of fractured rock: *Journal of Geophysical Research: Solid Earth* , **105**, 2981-3000.
- Mahmoudian, F., 2013, *Physical Modeling and Analysis of Seismic Data from a Simulated Fractured Medium*: Ph.D dissertation, University of Calgary (Canada).
- Marrett, R., Laubach, S., and Olson, J., 2007, Anisotropy and beyond: Geologic perspectives on geophysical prospecting for natural fractures: *The Leading Edge*, **26**, no.9, 1106-1111.
- Mavko, G., Mukerji, T., and Dvorkin, J., 2009, *The Rock Physics Handbook: Tools for seismic analysis of porous media*. New York: Cambridge University Press.
- Menke, W., 1989, *Geophysical Data Analysis: Discrete Inverse Theory: International Geophysical Series*, **45**. San Diego: Academic Press.
- Minsley, B. J., Burns, D. R., and Willis, M. E., 2003, *Fractured Reservoir Characterization using Azimuthal AVO*: Massachusetts Institute of Technology. Earth Resources Laboratory.
- Molotkov, L. A., and Bakulin, A. V., 1997, An effective model of a fractured medium with fractures modeled by the surfaces of discontinuity of displacements: *Journal of Mathematical Sciences*, **86**, 2735-2746.
- Nelson, R. A., 1985, *Geologic Analysis of Naturally Fractured Reservoirs*. Houston, TX: Gulf Professional Publishing Company, Book Division.
- Nichols, D., Muir, F., and Schoenberg, M., 1989, Elastic properties of rocks with multiple sets of fractures: 59<sup>th</sup> Ann. Internat. Mtg., Soc. Expl. Geophys., Extended Abstracts, 471-474.
- Nishizawa, O., 1982, Seismic velocity anisotropy in a medium containing oriented cracks-transversely isotropic case: *Journal of Physics of the Earth*, **30**, 331-347.
- Nye, I. F., 1957, *Physical Properties of Crystals*. Oxford: Clarendon Press.
- O'Connell, R. J., and Budiansky, B., 1974, Seismic velocities in dry and saturated cracked solids: *Journal of Geophysical Research*, **79**, 5412-5426.
- Olson, J., and Pollard, D. D., 1989, Inferring paleostresses from natural fracture patterns: A new method: *Geology*, **17**, 345-348.
- Press, W. H., 2007, *Numerical Recipes: The Art of Scientific Computing*, 3<sup>rd</sup> edition. New York: Cambridge University Press.

- Pšenčík, I., and Martins, J. L., 2001, Properties of weak contrast PP reflection/transmission coefficients for weakly anisotropic elastic media: *Studia Geophysica et Geodaetica*, **45**, 176-199.
- Rüger, A., and Tsvankin, I., 1997, Using AVO for fracture detection: Analytic basis and practical solutions: *The Leading Edge*, **16**, 1429-1434.
- Rüger, A., 1997, P-wave reflection coefficients for transversely isotropic models with vertical and horizontal axis of symmetry: *Geophysics*, **62**, 713-722.
- Rüger, A., 2002, Reflection Coefficients and Azimuthal AVO Analysis in Anisotropic Media: *Geophysical Monograph Series*; No. 10.
- Schoenberg, M., 1980, Elastic wave behavior across linear slip interfaces: *The Journal of the Acoustical Society of America*, **68**, 1516-1521.
- Schoenberg, M., 1983, Reflection of elastic waves from periodically stratified media with interfacial slip: *Geophysical Prospecting*, **31**, 265-292.
- Schoenberg, M., and Douma, J., 1988, Elastic wave propagation in media with parallel fractures and aligned cracks: *Geophysical Prospecting*, **36**, 571-590.
- Schoenberg, M., and Protazio, J., 1992, Zoeppritz rationalized and generalized to anisotropy: *Journal of Seismic Exploration*, **1**, 125-144.
- Schoenberg, M., and Sayers, C. M., 1995, Seismic anisotropy of fractured rock: *Geophysics*, **60**, 204-211.
- Sherriff, R. E., 1991, *Encyclopaedic Dictionary of Exploration Geophysics*: Society of Exploration Geophysicists, Tulsa, Oklahoma.
- Shuey, R., 1985, A simplification of the Zoeppritz equations: *Geophysics*, **50**, 609-614.
- Thomsen, L., 1986, Weak elastic anisotropy: *Geophysics*, **51**, 1954-1966.
- Thomsen, L., 1988, Reflection seismology over azimuthally anisotropic media: *Geophysics*, **53**, 304-313.
- Thomsen, L., 1993, Weak anisotropic reflections: Offset-dependent reflectivity—Theory and practice of AVO analysis: *Soc. Expl. Geophys*, 103-111.
- Thomsen, L., 1995, Elastic anisotropy due to aligned cracks in porous rock: *Geophysical Prospecting*, **43**, 805-829.
- Thomsen, L., 2002, *Understanding Seismic Anisotropy in Exploration and Exploitation: SEG 2010 Distinguished Instructor Short Course*.
- Tsvankin, I., and Lynn, H. B., 1999, Special section on azimuthal dependence of P-wave seismic signatures-Introduction: *Geophysics*, **64**, 1139-1142.
- Tsvankin, I., 2001, *Seismic Signatures and Analysis of Reflection Data in Anisotropic Media*. Amsterdam: Pergamon Press.
- Varela Gutierrez, I., 2009, *Fracture Studies From Amplitude versus Offset and Azimuth and Vertical Seismic Profile Data*: Ph.D dissertation, The University of Edinburgh (United Kingdom).
- Vernik, L., and Kachanov, M., 2012, On some controversial issues in rock physics: *The Leading Edge*, **31**, 636-642.
- Winterstein, D., 1990, Velocity anisotropy terminology for geophysicists: *Geophysics*, **55**, 1070-1088.
- Worthington, M., 2008, Interpreting seismic anisotropy in fractured reservoirs: *First Break*, **26**, 57-63.
- Xiao, C., 2006, *A Comparison of Different Methods for Estimating Thomsen Anisotropy Parameters*: M.Sc thesis, University of Calgary (Canada).
- Zheng, Y., 2006, *Seismic Azimuthal Anisotropy and Fracture Analysis from PP Reflection Data*: Ph.D dissertation, University of Calgary (Canada).